Time-resolved aberrometry of the eye with a Shack-Hartmann wavefront sensor

by Charles-Edouard Leroux

Supervisor: Prof. Chris Dainty

OÉ Gaillimh
NUI Galway

A thesis submitted in partial fulfilment of the requirements for the degree of Doctor of Philosophy,

School of Physics, College of Science,
National University of Ireland, Galway

March 2010

Abstract

Measurements of the monochromatic aberrations of the human eye have recently found many exciting applications in vision science. Nowadays, the most popular technique is the Shack-Hartmann wavefront sensor. The recent development of imaging detectors, and in particular the ones based on CMOS technology, have allowed the implementation of Shack-Hartmann wavefront sensors with finer spatio-temporal sampling.

We present a custom-built aberrometer, primarily designed to perform fast measurements of ocular wavefronts. An important part of the work presented in this thesis was to test the aberrometer both statically and dynamically, and we have tried to provide practical solutions to improve aberrometry of the eye.

Time-resolved measurements were performed with this aberrometer, and have been used as input for another PhD project (by Conor Leahy), which aims to model and describe the statistics of the microfluctuations of ocular wavefronts. In particular, we have completed in collaboration with Dr. Luis Diaz Santana (City University, London) an experimental study of the microfluctuations of the accommodative system of the young human eye.

Acknowledgement

Before we start, I want to thank the following people:

Chris Dainty, for sharing his enthusiasm for experimental physics with his students (including myself), and for his invaluable guidance during my PhD project.

Christof Pruss, who helped me a lot when I was an undergraduate student in Stuttgart.

Conor Leahy and Luis Diaz-Santana, for their enthusiasm when we worked together.

My coworkers at the Applied Optics Group, for sharing with me their knowledge in practical optics.

My friends in Galway, who have been so nice during some difficult times of my life.

My friends in Le Havre, who have been so nice and helpful with us.

Dorothée, Antoine, and Olivier. I am proud of the way we stay united.

My dear parents, Florence and Patrick. For the love and the strength they gave me.

My research was funded by Science Foundation Ireland, under Grant No 07/IN.1/I906.

Contents

Abbreviations

SHWFS: Shack-Hartmann wavefront sensor
AO: adaptive optics
CCD: charge coupled device
CMOS: complementary metal oxide semiconductor
FFT: fast Fourier transform
rms: root mean square
D: dioptres
MTF: modulation transfert function
(C)SLO: (confocal) scanning laser ophthalmoscope
OCT: optical coherence tomography
FWHM: full width at half maximum
DU: (10-bit) digital units
FIM: Fisher information matrix
CRB: Cramér-Rao bound
MSE: mean-square error
ML: maximum likelihood
MAP: maximum a-posteriori
PSD: power spectral density
ACF: autocorrelation function

Chapter 1

Introduction

The study of the higher-order monochromatic aberrations of the eye is a topic that has interested many researchers over the centuries, including illustrious scientists like Young and Helmholtz. High order aberrations are the imperfections of the eye that cannot be corrected with classical spectacles. To our knowledge, observations of high order aberrations published before 1961 were done by the subjects themselves, using a mask placed close enough to their pupil so that the pattern they would see was related to their "spot diagram". Thanks to the ophthalmic implementations of the Shack-Hartmann and other wavefront sensors, ocular wavefronts are nowadays instantaneously and objectively measured in the pupil plane. The Shack-Hartmann wavefront sensor (SHWFS) is the main actor of modern aberrometry, even though other techniques might as well be applied in the future for finer research studies on ocular wavefronts.

1.1 The early days of aberrometry

The Hartmann, Tscherning, and Howland tests

The most famous implementation of these so-called "screen tests" is the Hartmann test, which has been primarily invented by Hartmann in 1900 to test the Great Refractor at Postdam, and later to test large primary mirrors [1]. The basic principle of such a test is to observe the distribution of the light in a plane slightly out of the focus of an optical system that is sampled in its entrance/exit pupil by an opaque screen with

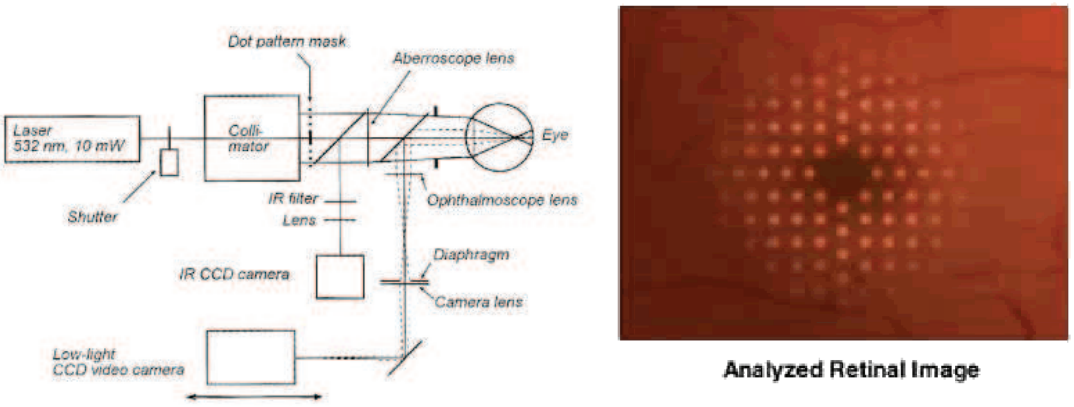

Figure 1.1: The aberroscope: an objective implementation of the Hartmann test [3].

equally spaced holes. The Hartmann screen and the position of the plane of observation have to be carefully designed, to find the optimal tradeoff between the sensitivity of the test, the diffraction-induced blur, and the overlapping of the Hartmann spots [2]. Figure 1.1 shows a commercial device (LASIK EYE CENTERS, Vancouver) which allows an objective recording of the Hartmann mask projected on the retina using a CCD camera. The adjustable "aberroscope lenses" allow conjugation of the mask with the pupil and to defocus the spot pattern so that it covers approximatively a 5 degree field in the retina.

A similar screen test had been previously proposed and implemented by Tscherning in 1894 ("Tscherning aberroscope"). Using a star as distant source, he asked his subjects to draw the shadow of a rectangular grid projected on their retina [4]. Intuitively, the accuracy and the precision of a screen test is closely related to the shape and the signal to noise ration of the recorded spot. A first optimisation of the original Tscherning test was suggested by Howland et al. in 1968 [5], who suggested the use of two cylindrical lenses to project the Tscherning rectangular grid, so that the diffraction effect would occur along the direction of the shadowed lines of the grid when the measured aberrations are small. Howland et al. measured 50 subjects in 1977 using a subjective implementation of this test [6], now referred as the "Howland aberroscope". Later, Walsh et al. took benefit of the development of the CCD camera to build the first objective Howland aberroscope [7–9]. Figure 1.2 shows an example of a raw frame, and the estimated distorted grid. The intersections of the grid represent the (defocused) spot diagram of the eye. Clearly, these early objective measurements could only indicate the major features of the ocular aberrations.

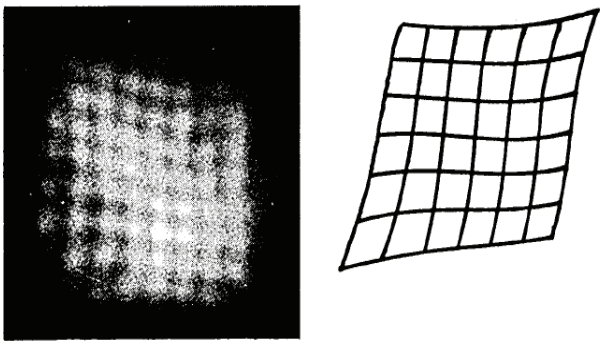

Figure 1.2: Raw CCD frame and estimated grid recorded by Walsh et al. [7], using the first objective Howland aberroscope in 1984.

The Scheiner and Smirnov tests, and the laser-ray tracing sensor

Smirnov in 1961 [10] proposed a very powerful method to measure the transverse aberrations of the human eye, by using a moveable aperture (translated in the pupil plane) to scan the local slopes of the wavefront in the pupil plane. This principle takes advantage of the good capability of the subject to align a vernier image, which was already used by Scheiner to measure the spherical error in 1619, and then by Young to measure the sphero-cylindrical errors and observe clearly the effects of the high order aberrations. Webb et al. later constructed an upgraded version of Smirnov's test ("spatially resolved refractometer") and quantified the wavefront map by integration of the wavefront slopes [11, 12].

The scanning of a narrow laser beam in the pupil plane was later suggested by Navarro et al. [13, 14] ("laser ray-tracing"), and can be seen as an objective implementation of Webb's refractometer. It uses an automated probing of the pupil plane and an objective measurement of the angle of the wavefront slopes with a CCD camera conjugated with the retina. The (repeatable) errors introduced by the control system that scans the probing beam can be calibrated with a reference wavefront. Using a pentaprism for the scanning reduces greatly these errors, as the direction of the probing beam is unchanged if the pentaprism is slightly rotated. The pentaprism test can thus be done without any reference optics, which is a great advantage when testing large optics. The so-called scanning pentaprism test had been successfully used before 1993, for the measurement of the conic constant of the 1.8 m f/1 primary mirror of the Stewart Observatory Mirror Lab [15].

1.2 The Shack-Hartmann wavefront sensor

Physical description of the Shack-Hartmann wavefront sensor

A SHWFS consists of an array of lenslets that sample a wavefront, typically in the exit pupil plane of an optical system, and an imaging CCD or CMOS detector. The deviation of the spot imaged by each lenslet on the detector is proportional to the the locally-averaged gradient of the measured wavefront.

The principle, which can simply be understood with geometrical optics, has been originally proposed by Roland Shack in the late 1960's as an alternative to the loss of energy inherent to the mask originally invented by Hartmann, for the real-time compensation of the effects of atmospheric turbulence on images captured by ground-based telescopes.

A more physical description of the SHWFS can be found in the literature [16]. It assumes that each lenslet of the sensor can be described independently. Writing down the Fresnel approximation of the propagation of the optical field from the pupil plane (z_1) of the lenslet to the detector plane (z_2) yields the equation of propagation of the centroid $\boldsymbol{\rho}(z)$ of the light distribution $I(\mathbf{x},z)$, along the z-axis:

$$\boldsymbol{\rho}(z_2) = \boldsymbol{\rho}(z_1)(1 - \frac{z_2 - z_1}{f}) + \frac{z_2 - z_1}{Es} \int_{\mathbf{x}_1 \in L} I(\mathbf{x}_1, z_1) \boldsymbol{\nabla} W(\mathbf{x}_1, z_1) d^2\mathbf{x}_1 \tag{1.1}$$

The centroid position $\boldsymbol{\rho}(z_2)$ of the irradiance distribution $I(\mathbf{x}_2, z_2)$ in the infinite detector plane is proportional to the spatial integration of the gradient of the wavefront $W(\mathbf{x}_1, z_1)$ over the lenslet L, as long as the irradiance $I(\mathbf{x}_1, z_1)$ in the pupil plane is homogeneous over L. The estimated gradient of the wavefront is scaled by the distance $z_2 - z_1$ that needs to be calibrated, as we describe in Chapter 2. When the detector plane is not in the effective focal plane of the lenslet ($z_2 \neq z_1 + f$) and when $\boldsymbol{\rho}(z_1) \neq 0$, the term $\boldsymbol{\rho}(z_1)(1 - (z_1 - z_2)/f)$ is also a source of bias in the wavefront estimation.

In principle, the domain of linearity of the SHWFS is very large. The parabolic approximation of the Huygens-Fresnel principle involved to obtain Equation 1.1 is valid if the distance $d(\mathbf{x}_1, \mathbf{x}_2)$ between any point $\mathbf{x}_1$ of the support of the lenslet L and any point $\mathbf{x}_2$ of the detector plane that significantly contributes to the total centroid position $\boldsymbol{\rho}(z_2)$ can be approximated by its first order Taylor expansion:

$$d(\mathbf{x}_1, \mathbf{x}_2) \simeq |z_1 - z_2| \times \left(1 + 1/2 \times \left[\frac{\|\mathbf{x}_1 - \mathbf{x}_2\|}{z_1 - z_2}\right]^2\right) \tag{1.2}$$

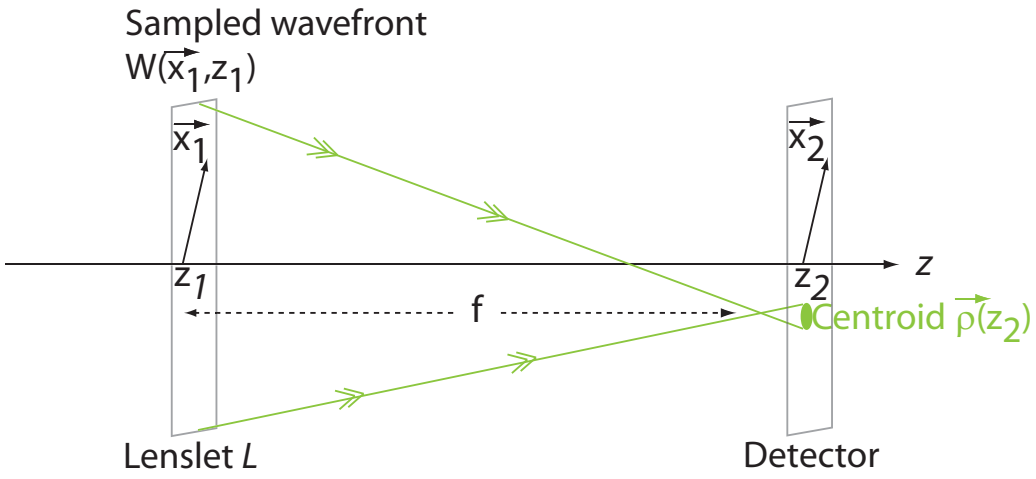

Figure 1.3: Geometry of the detection of a Shack-Hartman spot, as described by Equation 1.1. The detector is in a plane $(\mathbf{x}_2, z_2)$, at a distance $(z_2 - z_1)$ from the lenslet L. f is the effective focal length of the lenslet.

This approximation is valid assuming that the second order term is much smaller than the first order term:

$$1/8 \times \left[\frac{\|\mathbf{x}_1 - \mathbf{x}_2\|}{z_1 - z_2}\right]^4 \ll 1/2 \times \left[\frac{\|\mathbf{x}_1 - \mathbf{x}_2\|}{z_1 - z_2}\right]^2$$

$$\text{or equivalently: } \frac{\|\mathbf{x}_1 - \mathbf{x}_2\|}{|z_1 - z_2|} \ll 2 \tag{1.3}$$

The SHWFS that we present in Chapter 2 has a 7.5 mm focal length and a 0.2 mm pitch, which is typical for aberrometry of the eye. With our system, the left-hand side of Equation 1.3 is therefore in the order of 7×10^{-4}, and the parabolic approximation required to obtain Equation 1.1 is valid.

A major problem is that the spatial integration in Equation 1.1 should be done over an infinite plane, which is in practice impossible. The processing of the raw data recorded by a SHWFS is carried out independently for each spot over a small portion of the frame ("local window"), which is numerically defined and centered as much as possible on the corresponding spot. The truncation of the Shack-Hartmann spot and the crosstalk of two neighboring spots are two common sources of (signal-dependant) bias in the estimation of the position of the Shack-Hartmann spot.

Depending on the application of the SHWFS, further processing is carried out on

the estimated slopes of the wavefront. In an open-loop application, the wavefront can be numerically computed using either a modal or a zonal reconstructor. This so called wavefront reconstruction can introduce some additional numerical artefacts, as we briefly describe in Chapter 4. For example, the zonal reconstruction of the wavefront assumes that the measured wavefront is "locally plane", which is not necessarly the case in Equation 1.1. For an adaptive optics (AO) system, the wavefront is usually not of direct interest. The estimated slopes are used to compute the required control command of the corrector system, using a calibration (again, modal or zonal) of the system {wavefront sensor+wavefront corrector}.

Two alternatives to this two-step approach have been proposed and numerically tested [17, 18], but yet not experimentally implemented. Their common principle consists in using the raw data from the camera as input to get a direct estimate the wavefront and/ or the control command of an AO system. The maximum likelihood (ML) approach seeks the wavefront that maximises the probability of obtaining the actual recorded data [18], while a maximum a-posteriori (MAP) estimator [17] looks for the most likely wavefront given the recorded data. They would generally be expected to have a better precision and accuracy than the classical two-step approach used in wavefront sensing. Many decisive choices of parameterisation make these approaches very complex in terms of practical implementation, and they are also very expensive in terms of computational time. An even more complex issue remains their robustness towards a lack of statistical and physical knowledge of the measured wavefronts, of the noise on the raw data and of other physical nuisance parameters that significantly influence the data. Typical significant nuisances in wavefront sensing applications include the non-uniformity of the intensity in the pupil plane and undersampled high spatial frequencies of the wavefront.

The fundamental limitation of the Shack-Hartmann wavefront sensor

When a SHWFS is designed with a very fine spatial sampling, the assumption of independence of each lenslet does not always hold. Primot describes the SHWFS as a grating interferometer, and uses Fourier analysis to quantify the effect of adjacent lenslets on the estimation of the wavefront gradient [19]. The compression ratio H (lenslet pitch/size of the diffraction limited spot) parameterizes the importance of the crosstalk effect. For a typical aberrometer ($H = 4$), Primot evaluated that each local window contains significant information about an area of the pupil that is twice the size of the lenslet [19].

The crosstalk has thus an important effect in aberrometry. The size of the laser

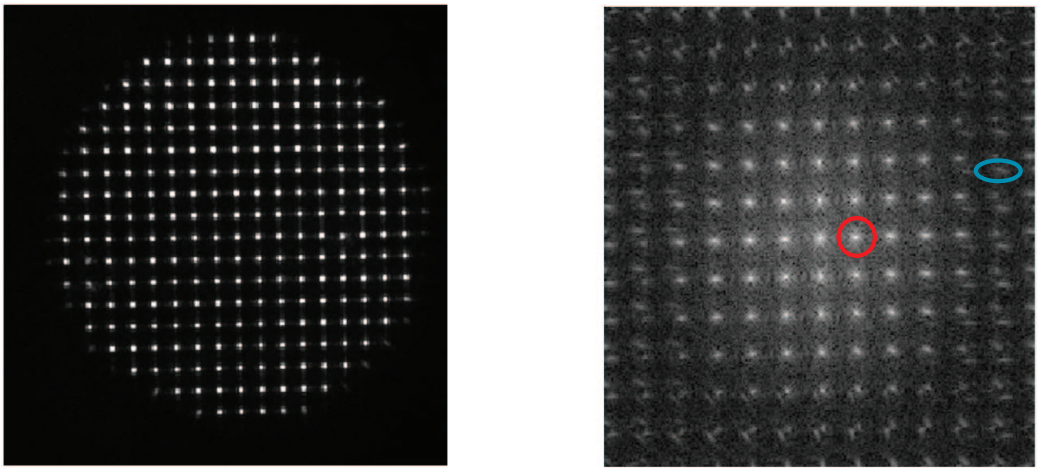

Figure 1.4: The figure shows an example of CCD frame recorded by a SHWFS (left), and its spectrum (right). Courtesy of Primot [19]. The blue ellipse shows an harmonic due to the crosstalk, which is outside the grid of the main harmonics because the CCD camera undersamples this spot pattern. The harmonic circled in red can be used to get an estimate of the horizontal gradient of the wavefront. The SHWFS has a $H = 6$ compression ratio, so that the main harmonics are located on a 13×13 grid.

beacon created on the retina with the probing beam, and the scattering of the light through the biological tissue also increase the crosstalk between lenslets. One way to decrease the crosstalk between lenslet, which has not been mentioned by Primot [19], is to use a local window of size smaller than a lenslet.

The spectrum of the raw data recorded by a SHWFS, which can be computed with a simple fast Fourier transform (FFT) algorithm, gives an approximate estimate of the wavefront gradient [19, 20]. We show in Figure 1.4 an example of raw data recorded by a SHWFS with a $H = 6$ compression ratio (left), and the corresponding spectrum computed using a FFT algorithm (right). In principle, the spectrum of the raw CCD frame recorded by the SHWFS consists of $(2H + 1) \times (2H + 1)$ harmonics centered on a square grid. In Figure 1.4, higher harmonics are located outside of the square grid (see for example blue ellipse), because of some aliasing effects (the CCD camera undersamples the Shack-Hartmann spots).

Dynamic range of a Shack-Hartmann wavefront sensor

Increasing the dynamic range of a SHWFS allows us to measure highly aberrated wavefronts, without compromising its sensitivity. Classically, a tradeoff between the sensitivity and the dynamic range consists of choosing the longest focal length of the

lenslet array that allows each spot of the SHWFS to remain in the field of view of its lenslet (for a given application of the SHWFS).

If one chooses to reduce the focal length to increase the dynamic range of the SHWFS, one can also reduce the size of the aperture of a lenslet (to get a finer spatial sampling of the pupil) and still keep the compression ratio constant. However, the amount of light collected by each lenstet is reduced (and so does the signal to noise ratio of the data), which is not acceptable in some real time application of the SHWFS.

The dynamic range of a SHWFS is limited by the ability of the system to process the recorded data. Two major difficulties occur for the processing of the Shack-Hartmann data.

The first problem occurs when two adjacent spots are so close that they cannot be processed independently. The crosstalk of adjacent spots happens when the curvature of the wavefront is locally too large. The main method to overcome this limitation of the SHWFS is to record the spots sequentially, which is what a laser ray tracing wavefront sensor does [13]. This can be done using a spatial light modulator that switches on and off the lenslets, as it was implemented by Lindlein et al. [21]. Yoon et al. [22] successfully implemented a similar method using a translatable obstruction mask for the measurement of ocular aberrations in a population of keratoconus eyes.

A second difficulty occurs when the Shack-Hartmann spots leave the field of view of their lenslets. This effect is considered to be the first limitation in the operation of a SHWFS, because the crossover of adjacent spots usually happens for a higher amount of aberration. This limitation of the SHWFS can be overcome with methods that are robust to large displacements of the spots. A simple hardware solution is to measure the centroid positions for different longitudinal positions of the detector [23]. Some algorithmic solutions have also been suggested in the literature. Extending the range of a SHWFS with an algorithmic solution permits the measurement of highly aberrated wavefronts instantaneously, which is one of the key features of a SHWFS. For most algorithmic approaches, the problem consists in finding the lenslet that corresponds to each measured centroid position.

Various methods have been suggested in the literature. One approach is to manufacture a lenslet array that has a calibrated periodic change in the structure of the lenslet array (for example the pitch of the lenslet), and to identify this structure in every measured map of centroid positions [24]. A similar method was also introduced by Lindlein et al. [25, 26], who suggested using a lattice of astigmatic lenslets with different (and calibrated) principal axes, and to identify the corresponding direction

in the pattern of each Shack-Hartmann spot. A powerful idea to retrieve the corresponding lenslet of each Shack-Hartmann spot is to apply an iterative extrapolation of the measured centroid positions, using some previously indexed centroid positions. Previously proposed methods to implement this idea rely on the use of adjacent centroid positions, and can thus be considered as local extrapolation [27–29]. One of these methods, which relies on a spline extrapolation [28], has been successfully implemented for the measurement of ocular aberrations at large field angles [30]. An interesting alternative to measure a highly aberrated wavefront is to directly extract the gradient of the wavefront from the raw CCD frame, using a Fourier demodulation technique [19, 20]. This approach is simple and has a low computation time. Roggemann et al. [31] also introduced a method to extend the dynamic range of a SHWFS using the raw CCD frame and an additional image of the point spread function.

We have proposed a method based on the iterative extrapolation of the measured centroid positions [32], and used this method for the measurement of the microfluctuations of accommodation over a wide range of accommodative state (see Chapter 5). The main difference with the above methods [27–30] is that the extrapolation required to gradually analyze the whole pupil is performed on the wavefront itself, using Zernike polynomials. This method is presented in Chapter 4.

The principle of aberrometry

The basic principle of aberrometry is to measure the wavefront of the light backscattered by the retina. The first pass through the optics of the eye leaves a signature on the measured wavefront if the probing beam that enters the eye has a large diameter, and if no speckle-removal technique is used [33, 34]. To average the speckle effect over a short time (< 5 ms) one can either use a scanning mirror, or a source with a large bandwidth [35]. The first method is efficient for surface scattering: one needs to scan the probing beam across the retina with an amplitude much larger than the size of the laser beacon [36]. The second method is more effective if the scattering happens in a three dimensional volume. In this case, the bandwidth of the source must be sufficiently large to average the wavelength-dependant propagation of the optical field through the retinal layers. Another method to create an incoherent beacon in the fundus of the eye is to use the fluorescent properties of the retinal layers [37].

Alternative to the Shack-Hartmann wavefront sensor

The SHWFS does not give a very fine sampling of the wavefront, but has the potential to have a great dynamic range. An alternative to the SHWFS in an ophthalmic

application is the pyramid wavefront sensor [38,39]. The pyramid wavefront sensor is a powerful implementation of Foucault's knife-edge test, and allows for a quantitative measurement of the local slopes of the wavefront thanks to the rotation in a retinal plane of the measured beam around the top of the pyramid. To our knowledge, the knife test was used for the first observation of ocular aberrations in the pupil plane [40], and is routinely used by optometrists for the prescription of spectacles (using the "retinoscope"). An ophthalmic application of the pyramid wavefront sensor has been successfully demonstrated by Chamot et al. within an AO system [41].

The pyramid wavefront sensor is best suited for closed-loop applications, as its sensitivity and spatial sampling can be tuned for each experiment [42]. The sampling properties of the wavefront sensor are in general better with a pyramid than with a SHWFS, except if the latter works in the "quad-cell mode" (2×2 CCD pixels per lenslet). In this case, the spatio-temporal sampling reached by the two sensors is the same, for a given number of CCD pixels.

The linear range of the pyramid is limited by the fact that the modulation of the beam around the top of the pyramid has to be much larger than the point spread function of the aberrated beam [43]. The linear range of a pyramid wavefront sensor is thus limited by the maximal amplitude of modulation achievable by the steering mirror, which makes the pyramid wavefront sensor not a very good open-loop sensor. The lack of linearity is also a well-known feature of the quad-cell Shack-Hartmann wavefront sensor [44,45].

A curvature sensor records the intensity distribution in two planes that are slightly and symmetrically defocussed from the measurement plane [46]. It is therefore a special case of the phase diversity technique, which can be applied with various combinations of aberrations [47]. The principle of the curvature sensor relies on the intensity transport equation:

$$\frac{\partial I}{\partial z} = -\boldsymbol{\nabla} I \cdot \boldsymbol{\nabla} W + I \nabla^2 W \tag{1.4}$$

Assuming that the intensity is uniform over the pupil, one can obtain the curvature of the wavefront $\nabla^2 W$ from the measured difference in the intensity distribution taken in two planes, $\frac{\partial I}{\partial z}$. A major artefact of the curvature wavefront sensor is that the term $\boldsymbol{\nabla} I \cdot \boldsymbol{\nabla} W$ in Equation 1.4 is non zero at the edge of the pupil, which creates large errors in the measurement of the wavefront. These errors propagate from the edge to the central region of the pupil. This effect cannot be neglected, and the knowledge of the gradient of the wavefront at the edge of the pupil is required to retrieve W. This mathematical problem is referred to the Poisson equation with Neumann

boundary conditions, and is usually time consuming to solve. The curvature sensor is however an efficient solution for many applications of AO, as the curvature of the surface of some deformable mirrors is proportional to the applied commands [48]. This is the key concept of the AO system developed for free-space communication by the company AOPTIX. Like the SHWFS and the pyramid wavefront sensor, the curvature sensor works with incoherent light. It is however very sensitive to the size of the source, which leaves a mark in the defocussed intensity distributions [49].

The curvature sensor is very efficient in terms of spatial sampling, because the wavefront is effectively measured at each pixel of the detector. Curvature sensors have therefore been implemented to measure ocular aberrations [50–52]. In particular, Gruppetta et al. [53] reported a curvature sensor to measure the topography of the cornea, and took advantage of the fine spatial sampling to study the dynamics of the tear film.

1.3 Clinical relevance of modern aberrometry

Many studies involving objective measurements of the monochromatic aberrations of the human eye have been carried out during the last decade. After the early measurements of Liang et al. with a SHWFS [54–56], some studies have been made to model the statistical properties of the human eyes over large populations of young and healthy eyes [57–59]. These studies broadly agreed on the significance of the amount of ocular aberrations of radial order higher than 2: Thibos et al. found a mean root mean square (rms) value of 0.3 μm for a 6 mm pupil [57], while Williams et al. found 0.35 μm for a 5.7 mm pupil [58]. The relevance of aberrometry for the prescription of spectacles is not obvious, because these values only correspond to the rms of a pure sphere of 0.25 dioptres (D), which is the resolution of a standard subjective refraction made by an optometrist.

The direct analysis of the wavefront map and its rms value is however rarely enough to prescribe spectacles or to investigate the visual acuity of a subject. The quality of a retinal image is not linearly related to the rms value of the wavefront. A simple metric of image-quality that illustrates this idea is the so-called "rms spot radius", which can be minimised by a proper combination ("balancing") of Zernike polynomials [60, 61]. As a result, using the defocus term $z_{2,0}$ measured by the aberrometer is in general not a good method to prescribe spectacles [62], even if the achromaticity of the eye can be partially taken into account in the measurement of the

monochromatic aberrations (usually made in the near infrared) [57, 63].

Similarly, McLellean et al. [64] discussed the variability in the modulation transfer function (MTF) that can be obtained from simulated wave aberrations with a fixed rms. Interestingly, they found that the MTF of real eyes is usually higher than the MTF of s simulated eye with the same rms. This result suggests that the optics of the eye are somehow optimised for retinal image quality.

The temporal variations of the ocular aberrations is another reason to analyse the outcome of an aberrometer with care. Many clinical studies have been done on the long term variations of ocular aberrations, as it is a major issue in their possible correction via laser surgery or other methods. This issue depends a lot on the investigator and the equipment used. In particular, the alignment procedure is known to play a major role in aberrometry [65]. Cheng et al. used the COAS aberrometer manufactured by AMO Wavefront Sciences and reported a stable rms value of the high order aberrations of four healthy subjects, with a typical annual variation of 0.03 μm [66]. (This is 10 times smaller than the mean rms measured in the two largest population studies of healthy eyes.) Over a single week, they measured a modest standard deviation of 0.02 μm of the rms, but observed a significant variability in the measurement of individual Zernike modes. More recently, Miranda et al. measured 23 normal subjects with the IRX3 aberrometer manufactured by Imagine Eyes, and found no significant change of the high order aberrations over a week [67]. Ocular aberrations also seem to be stable over a single day, according to the measurements of Srivannaboon et al. on 20 normal eyes [68] and Pierscionek et al. on 17 eyes [69]. The number of subjects of these clinical studies is usually around 20, but we did not find any study with more than three measurements in a single day. Such a reduced number of measurements makes the analysis of these results incomplete, and in particular it is difficult to estimate relevant diurnal variations of ocular wavefronts.

Clinical studies show that the high order aberrations of the human eye tend to increase with age (for a given pupil size), but most probably with a small impact on vision thanks to the associated decrease in pupil size [70, 71]. The change of aberrations over a lifetime is a fundamental issue for the design of customised correction of high order aberrations.

1.4 Aberrometry in vision science

Modeling the optics of the eye

Modeling the human eye as a combination of realistic optical elements is potentially useful for the optimisation of any ophthalmic instrument. A single wavefront map is not enough information to understand the optics of the human eye, but the measurement of the aberrations across the visual field provides valuable information that can be used as inputs to retrieve the parameters of these elements, and thus obtain a "customised eye model" [72–76]. The same operation can in principle be done for the measurements of the accommodated eye, although in this case some of the parameters change with the level of accommodation. Systematic studies of the aberrations of the accommodated eye have already been reported [77,78], yet not directly compared to the prediction of a model, such as the one proposed by Navarro et al. [79] or later by Goncharov et al. [80]. The aberrometer we present in Chapter 2 of this thesis is well suited to the measurements of ocular aberrations as a function of the accommodative state.

The estimation of the parameters of a customised eye model gains in robustness if one can couple the measurements of the aberrometer with other ophthalmic instruments. The measurement of the paraxial curvature of the cornea, the depth of the anterior chamber, and the total axial length of the eye can for example be easily measured with the "IOL Master" manufactured by Zeiss [81]. The measurement of the angles between the main axis of the eye (pupillary axis, line of sight, tilt and decentration of the lens) can also potentially give important information about the origins of ocular aberrations, and can be done by locating the four Purkinje images of a suitable light source [82–85]. The radii of curvature of the lens (anterior and posterior) can also be measured using Purkinje imaging, or more directly using Scheimpflug imaging. An experimental comparison of both techniques was presented by Rosales et al. [86].

The use of a videokeratoscope can quantify the contribution of the cornea to the ocular aberrations, which is also potentially very useful to customise an eye model. Several studies tend to show that the aberrations introduced by the lens partially compensate corneal aberrations [87–90].

This instrument provides an estimate of the topography of the curvature of the cornea. From this topography, the aberrations induced by the cornea alone can be computed using an approximate index of refraction of 1.3375 [91]. To do this, commercial devices (such as the Atlas topographer, manufactured by Zeiss) use a ray-

tracing approach. A major problem, which should be solved in the very near future, is that the videokeratoscope uses the so-called keratometric axis as reference axis (defined by the paraxial centre of curvature of the cornea and the fixation point), whereas an aberrometer is meant to measure the ocular aberrations along the line of sight. The mismatch between the two axes, which can be for some subjects up to 10°, can lead to significant errors in the computation of the corneal aberrations of the human eye [92].

AO system for vision science

AO has first been successfully implemented with a flood illuminated retinal camera [56], in order to improve the resolution of images of the cones (the high resolution, photopic photoreceptors of the retina) [93–95]. It was later adapted to a scanning laser ophthalmoscope (SLO) [96]. With AO, SLOs and flood illuminated retinal cameras lead to similar field of view (typically 1 to 3 degree) and resolution (3 μm, or the typical size of a cone near the fovea). SLOs have however a better photometric efficiency, which permits imaging of the cone mosaic at video rates. SLOs are now stabilized in real time to remove the distortion of the reconstructed retinal images due to the microfluctuations of the fixation of the eye [97, 98]. With some image processing, it is thus possible to reconstruct high resolution, width-field images of the cone mosaic. This point is very relevant for clinical application, and can also be directly obtained with a suitably designed wide field SLO coupled to AO [99].

High resolution retinal cameras with flood illumination and AO correction are soon going to be commercialized. High resolution SLOs remain instruments of research, which need experienced investigators. The use of a confocal pinhole (confocal SLO, CSLO) increases the axial resolution of the instrument, and filters the light scattered by the deeper layers of the retina (or selects it, if the pinhole is replaced by a small blocking mask). Optical coherence tomography (OCT) coupled with AO can also provide an axial sectioning of the retinal layers [100], with an axial resolution of around 1 μm (depending on the bandwidth of the light source) and a transverse resolution around 5 μm. This is potential helpful for the visualization of the evolution of age-related macular pigment degeneration [101], a major source of blindness amongst older people. Figure 1.5 shows some retinal images obtained with a CSLO, coupled with AO (left graphs). Axial and transverse resolutions of three main retinal imaging systems (CSLO, OCT, flood illumination) are summarized by a schematic (right graph).

AO is also a very interesting tool to investigate the process of visual detection, and in particular to measure the visual performance of a subject after correction of

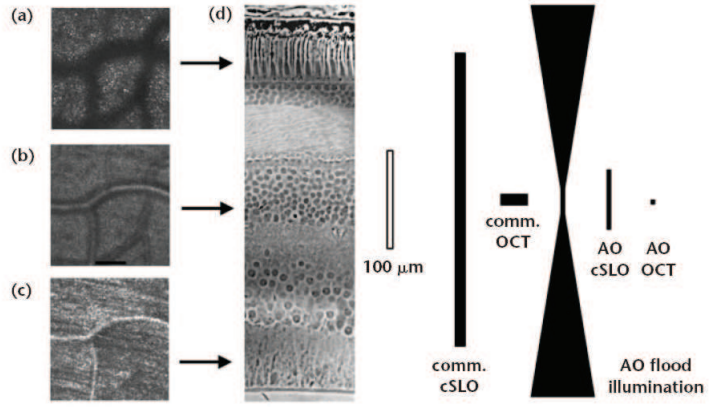

Figure 1.5: Resolution of modern retinal imaging systems. Left: three different layers imaged with a CSLO. Right: Effects of AO on the resolution of three main retinal imagers: CSLO, OCT, and flood illumination. Courtesy of Don Miller (School of optometry, Indiana University).

ocular aberrations [56,102]. If the AO system works well, one can measure the neural contrast sensitivity of the eye, which is the reduction in contrast of a retinal image (at a given spatial frequency) due to the neural processing alone. The neural contrast sensitivity function can also be measured by projecting some interference fringes on the retina using two narrow beams that are insensitive to the optics of the eye [103], as was suggested by Le Grand in 1935. AO is not limited to the measurement of the neural contrast sensitivity function, as it allows to measure the impact of ocular aberrations for a large variety of visual tasks [104].

Study of the microfluctuations of ocular aberrations

Understanding the statistical behavior of the microfluctuations of ocular aberrations has a potential impact on the design of future AO systems. It is also important to understand and to quantify the origins of the dynamical changes of the optics of the eye for the design of customised contact lenses.

A first study published by Hofer et al. concluded that a perfect AO system with a bandwidth of 1-2 Hz would compensate the ocular aberrations up to the diffraction limit for a 5.8 mm pupil [35]. The microfluctuations of ocular aberrations are typically above the $\lambda/14$ diffraction limit defined by the Marechal criterion, but have a low activity above 2 Hz. The benefit of using a static customised phase plate to improve the quality of a retinal imaging system was later demonstrated by Burns et al. with a scanning laser ophthalmoscope [105,106], and discussed using simulated images of

the cone mosaic [107].

Diaz-Santana et al. [108] later noted a significant increase in the measured Strehl-ratio of the double-pass point spread function when they used the maximum bandwidth of their high-speed AO system. (This bandwidth was 25 Hz, so one order of magnitude higher than the bandwidth of a standard AO systems implemented for vision science.) Like Hofer et al. [35], Diaz-Santana et al. [108] reported a decrease in the power spectra with a slope around -4/3 on a log-log scale. The study of Diaz-Santana et al. was carried out with a high-speed SHWFS (with a 240 Hz frame-rate), for which the fluctuations of the ocular wavefronts below 30 Hz were above the noise floor of the system. This limit was later pushed to 70 Hz by Nirmaier et al. [109].

The fluctuations of ocular aberrations are mostly driven by the fluctuations of accommodation [35, 110, 111], and the break up of the tear film [53, 112–115]. After a few seconds of experiment, the drift of the pupil of the subject can also influence the measured ocular aberrations. We present in Chapter 4 a simple algebraic model to understand the influence of the shift of the pupil on the measured Zernike coefficients, and we illustrate this model by some simultaneous measurements of ocular aberrations and drifts of the pupil of the eye.

Microfluctuations of accommodation

It is well known that the power of the lens of the eye changes rapidly and continuously [111, 116, 117]. Variations in the steady-state accommodative response are typically less than 0.25 D in magnitude, and are commonly known as microfluctuations [118]. The microfluctuations of accommodation play an important part in the variability of the optical quality of the eye and have therefore attracted much study.

An area of continued debate is the possible roles that microfluctuations play in the function of accommodation, and the question of whether they are involved in the accommodative control system [111]. The microfluctuations have been shown to be detectable by a normal observer [119], yet their exact role in the accommodative system is not fully understood. Either the microfluctuations are tuned according to the viewing conditions, or they simply represent uncontrolled interference.

Campbell et al. [116] first proposed a description of the main features of the commonly recorded accommodation signal: a low frequency component ($<$0.5 Hz), which corresponds to the drift in the accommodation response of the subjects, and a peak at higher frequency, usually observed in the 1-2 Hz band. This description of the frequency composition was also adopted in later studies [111, 120–124].

The high frequency components exhibit correlation with the cardiopulmonary system [117,125–127]. This observation suggests that the rapid variations of the shape of the crystalline lens are a consequence of its mechanical properties, and are not controlled by a neural process [111]. The relationship of the microfluctuations to the mean response of the accommodative system is of primary interest, because the physical nature of the process changes depending on the level of accommodative effort. Several authors have reported that the amplitude of the high frequency component increases with the target vergence [35,110,121,128].

The low frequency components of the accommodative response are very likely to be related to the ability of a subject to main a stable focus, and can therefore be used to quantify the influence of parameters in the visual process [129], such as the luminance of the target [124,130], pupil size [120], astigmatism [131] and high order aberrations [132]. When the subject does not have any target to fixate ("empty visual field"), the measured drifts of the accommodative response are described as the open-loop response of the accommodative system [133]. Alternatively, studies have reported the effects of high order aberrations [134–138] and longitudinal chromatic aberration [139–141] on the accommodative response using moving targets (step response or single frequency).

Variability of the location of peaks in the power spectral density across subjects had been noted by previous authors [111]. The temporal dynamics of the eye's focusing power have been characterised as non-stationary [35, 142]. Therefore, periodogram analysis is limited in what it can tell us, because the spectral power of the signal varies over time. Iskander et al. [142] identified low-frequency ($<$2 Hz) components in Zernike defocus that varied in both magnitude and frequency throughout measurements. Though they are incapable of resolving the time-varying frequency characteristics of signals, periodograms can still be of practical use in interpreting the major characteristics of the accommodative system, by giving an indication of the average spectral power.

We present in Chapter 5 our study of the dynamics of accommodation. In particular, we present a simple spectral analysis of the accommodative signal, and a study of its increments. These two mathematical tools show without ambiguity that a young and healthy eye has an accommodative signal with different statistics at around 4 D of "accommodative effort".

1.5 Thesis synopsis

We present in Chapter 2 the tests that we performed on our custom-built aberrometer: accuracy in the measurement of calibrated phase plates, suppression of the jitter of the system, and quantification of the speckle removal.

Chapter 3 describes the main issues for the design of an algorithm that estimates the positions of the Shack-Hartmann spots in an ophthalmic application. In particular, we stress the importance of the background on the raw frames recorded by the sensor (due to retinal scattering). The work described in this chapter has been published in Optics Express [143].

Chapter 4 describes simple computational issues inherent to the reconstruction of a wavefront map from a set of estimated centroid positions. We present the modal and the zonal approaches, their implicit assumptions and the corresponding bias. We also briefly present some measurements and simple modeling of the impact of the eye's decentration on the measured Zernike coefficients. In particular, we show the effects of the drift of the pupil on the measured wavefront for an unexperienced subject, during a 40 second trial using a synchronised tracking of the pupil. I was assisted in this part by Antoine Leroux, a summer student. Chapter 4 also presents a software-based method to extend the dynamic range of an aberrometer, which we published in Optics Express [32].

Chapter 5 describes our study of the microfluctuations of the accommodative system of a young human eye. We show how the "accommodative effort" influences the statistics of the measured accommodative signal, independently of the refractive errors of the subject. We recently published this work [144]. This work was collaborative with Conor Leahy and Dr. Luis Diaz-Santana.

Chapter 2

Design and tests of a versatile aberrometer

The aberrometer we present in this chapter is an efficient tool for the study of the aberrations of the accommodated eye, and for any open-loop ophthalmic application of the SHWFS. The basic idea was to design a system that has a great sensitivity, that can be adapted to a large number of experiments, and that does not require any optical adjustments when measuring highly aberrated ocular wavefronts. The design of the different fixation arms that we used during the project is not discussed in this chapter: using a beamsplitter just in front of the aberrometer allowed us to design various experimental studies of the dynamics of accommodation, as described in Chapter 5. We present in this chapter the main properties of our aberrometer, in terms of spatial and temporal sampling. We describe the calibration and the static tests of the system, and then present the tests we did to investigate experimentally the jitter of the system using an artificial eye. Some experimental data obtained on a real eye conclude this chapter, and illustrate the importance of reducing the speckled aspect of the recorded Shack-Hartmann spots using a scanning mirror.

2.1 Design of the aberrometer

2.1.1 Presentation of the system

Sampling properties

The design of a SHWFS is quite a complex issue, which requires a good knowledge of the targeted application. For the design of astronomical AO systems, end to end simulations are usually performed to find the optimal tradeoff between spatial sampling of the pupil and signal to noise ratio of the data (number of lenslets), sensitivity and dynamic range (focal length), accuracy and processing time (choice of algorithms).

End to end simulations are not reliable for opthalmic applications of the SHWFS, because there is little statistical knowledge about the temporal and spatial statistics of ocular aberrations. From our experience, the number of photons per lenslet is not a limiting factor in the design of an aberrometer (unless a lot of light coming out of the eye is lost). Also, we relied on an algorithmic method to extend the dynamic range of the SHWFS, which we present in Chapter 4. The starting point in the design of our system was the targeted frame rate, which we wanted one order of magnitude higher than a standard SHWFS for the eye (around 20 Hz [145]).

The first step in the design of the aberrometer was the choice of the detector. We decided to try a state of the art CMOS detector, the NIR Microvista manufactured by Intevac for near infrared applications. The quantum efficiency of this detector is 75% for our 0.78 μm operating wavelength, and the readout noise is 40 electrons/pixel rms. For a given pixel size, this CMOS detector achieves frame rates that are typically four times higher than a typical CCD camera. The number of pixels of the detector used to map the measured pupil fixes the frame rate of acquisition. We have used two configurations of the detector: 396×396 and 286×286 pixels for frame rates of 100 Hz and 173 Hz. Note that the manufacturer specifies a 100% fill factor, which is a major improvement of the CMOS technology. We have experimentally checked that the light-insensitive areas of the CMOS detector have a negligible effect on the measurement of ocular wavefronts. (See Section 2.2.)

From our experience in the processing of the SHWFS data (see Chapter 3), we know that we can estimate the centroid position of a Gaussian spot that has a 3.5 pixels FWHM, processed over a a 15×15 pixels local window. Shifts up to 3 pixels (from the centre of the local window) can be estimated without bias, even with the high amount of scattered light (see Figure 3.3). We therefore choose a square lenslet

array that has a 200 μm pitch, so that each lenslet corresponds to 18.5 $\times$ 18.5 pixels of the detector. The 7.5 mm effective focal length gives a Gaussian spots of FWHM 3.5 pixels, even for large aberrations (see Figure 5.2, obtained with an uncorrected ocular wavefront with a 5 D convergence).

The pupil of the eye is imaged onto the Shack-Hartmann lenslets with a 0.8 magnification to obtain the sampling properties summarized in Table 2.1. The measurement of a 3.9 mm pupil is suitable for the study of the accommodated eye, which is presented in Chapter 5. The pupil of the eye is sampled with a spatial resolution of 250 μm, which is standard for current opthalmic SHWFS. The system that relays the pupil of the eye to the SHWFS should not introduce significant aberrations, even if the incoming wavefront is largely aberrated. For example, we show in Figure 5.3 the measurement of Zernike aberrations for convergent incoming wavefront (0 to 7 D). Using an artificial eye, we were able to measure the same combination of tip/tilt/defocus with an artificial eye and an uncorrected accommodating eye. Over the 0 to 7 D range, we estimated the system aberrations as smaller than 40 nm rms (using 62 Zernike polynomials, astigmatisms included). These aberrations can also be easily removed by the use of a lookup table. It is also of primary importance to evaluate the distortion introduced by the system. Distortion cannot be simply compensated by a reference wavefront. The measured wavefront should be stretched according to the distortion figure.

Table 2.2 describes the geometrical parameters of the SHWFS. Through numerical simulations, it is possible to evaluate the benefit of a finer spatial sampling and a higher sensitivity [146, 147]. We present in Chapter 4 some results of similar calculations that do not take into account the "detectability" of the Shack-Hartmann spots. For example, Table 4.2 shows that for the estimation of 65 Zernike coefficients, increasing the sampling from 21 $\times$ 21 to 31 $\times$ 31 lenslets do not decrease significantly the noise on the estimated coefficients. An alternative to this purely numerical considerations was proposed by Llorente et al. [148], who used a laser ray tracing system to measure ocular aberrations with a variable spatial sampling. The pyramid wavefront sensor allows to have similar freedom, with the advantage that the wavefront is measured simultaneously over the pupil as with a SHWFS.

The optical layout of the system is shown in Figure 2.1. We use a scanning mirror (conjugated to the pupil plane) to reduce the speckle effect linked to the scattering properties of the retinal layers and to obtain time-resolved and low noise measurements. A first $4f$ system ($L1 - L2$) relays the exit pupil of the eye to the scanning mirror. We choose the smallest scanning mirror possible, in order to maximise the

Diameter of the measured pupil (mm)	Number of lenslets across the diameter	Frame rate (Hz)
3.9	15	173
5.4	21	100

Table 2.1: Sampling properties of the aberrometer.

Magnification of the pupil to the SHWFS	0.8
Size of a lenslet	$p = 0.2$ mm
Calibrated sensitivity of each lenslet	$f_l = 7.15$ mm
Size of a pixel of the CMOS detector	$\Delta = 10.8$ μm

Table 2.2: Geometry of the aberrometer.

scanning frequency allowed by the galvanometer on which it is mounted. The reduction of the beam coming out of the eye is thus naturally performed by the system ($L1 - L2$). The second $4f$ system ($L3 - L4$) conjugates the scanning mirror with the SHWFS. All the lenses used in the system are achromatic doublets, optimised for near infrared applications.

A field stop $F1$ is placed in a plane conjugated with the retina. $F1$ limits the field of the aberrometer to $\pm 2^\circ$, which corresponds to shifts of the Shack-Hartmann spots of $\pm 1.5 \times p$ (the pitch a lenslet). $F1$ allows to cut the small portion of the probing beam that is directly reflected by the lenses $L1$ and $L2$. These reflections, and the reflection from the cornea, are also controlled by translation of the probing beam parallel to the optical axis of the instrument. This is done by tilting the mirror $M1$, which is placed in a plane conjugated with the retina. When adjusting the position of the probing beam, it is important to make sure that it is far away from the position that maximises the Stiles-Crawford effect, which is typically less than 2 mm away from the center of the pupil [149, 150]. Doing so reduces the amount of light scattered from the fundus of the eye, but allows to collect data that has a uniform signal to noise ratio over the whole pupil.

A major feature of our aberrometer is its software-based extended dynamic range, which we describe in Chapter 4. Using our algorithm, each Shack-Hartman spot is not bound to remain in the area of the detector that corresponds to the "shadow" of its lenslet. We designed our aberrometer so that the quality of the recorded data is robust to large ocular aberrations. This specification is achieved by using a very narrow probing beam, of FWHM 0.5 mm in the entrance pupil of the eye. As a result, we measure Shack-Hartmann spots that are larger than the diffraction limit of a single lenslet: 3.5 pixels FWHM (instead of 2.4 pixels for the diffraction limit). This

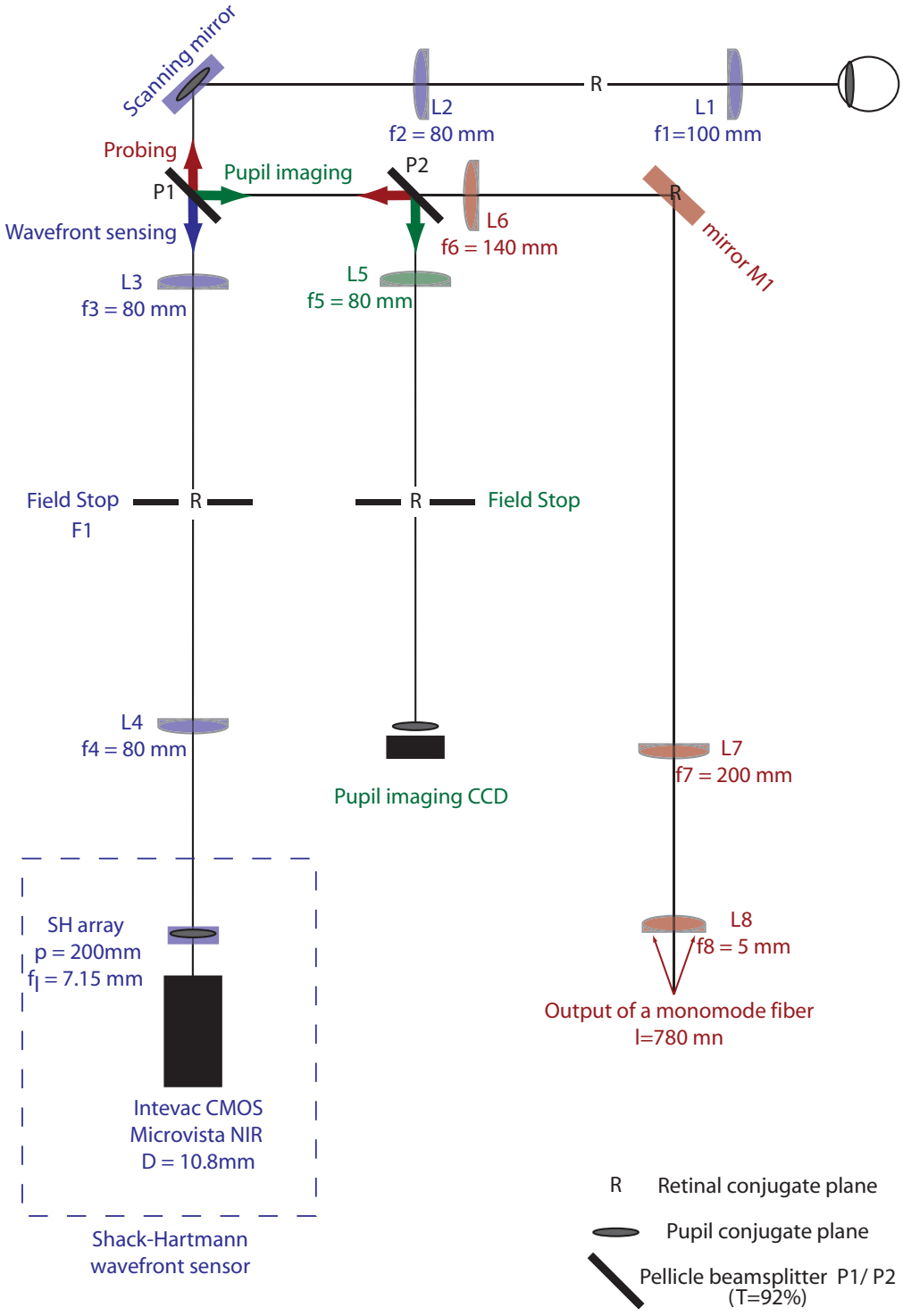

Figure 2.1: Optical layout of the aberrometer.

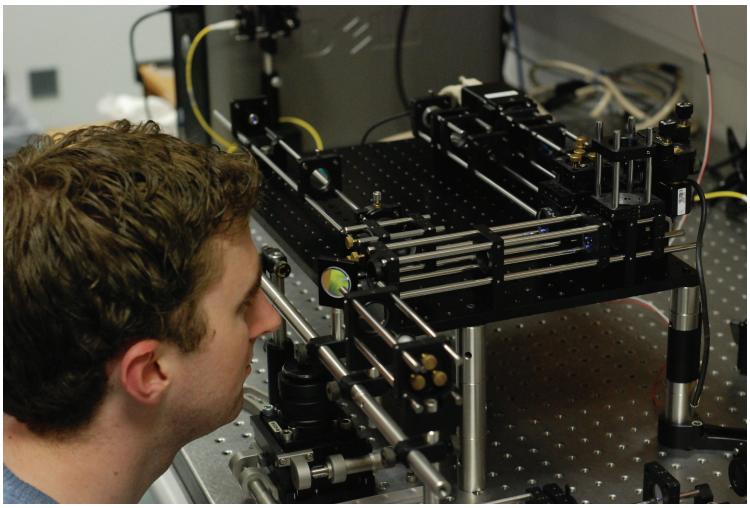

Figure 2.2: Picture of the aberrometer, which stands on a 30×45 cm breadboard. Outside the breadboard lay the bite-bar and the fixation arm, which was used for the study presented in Chapter 5.

reduces the compression ratio down to 2.6, but the geometry of the detection remains the same for most eyes. For example, we did not measure any significant spread of the Shack-Hartmann spots when measuring young subjects at different level of accommodation. (See Chapter 5.) In most aberrometers, the defocus term of an ocular wavefront, which is due to a combination of the refractive error and the accommodative state of the subject, is easily corrected with additional optics (a "Badal" system). This is less true for astigmatism, which requires cylindrical lenses (and the associated back-reflections). We consider the use of the extended range of our aberrometer for the measurement of accommodating eyes as a proof of principle of both our algorithm and optical design, which will hopefully be helpful to other research groups.

For the design of an aberrometer with the same sensitivity and a larger dynamic range than our aberrometer, we would recommend to avoid the use of any relay lenses that are common to the wavefront-sensing and the probing arms ($L1$ and $L2$ in Figure 2.1). Doing this eliminates the back reflections from these lenses, and makes the field stop $F1$ unnecessary. The remaining back reflections from the cornea are easily suppressed by a small translation of the probing beam away from the centre of the pupil of the eye. On the other hand, the use of a scanning mirror is no longer possible, and the reduction of speckle would be done using a low-coherence light source (typically a superluminescent diode). A simple design is given in Figure 2.3. This design seems suitable for a clinical implementation of a simple aberrometer with

a large dynamic range. A major application for such an instrument is the measurement of ocular aberrations of patients with keratoconus, who have an abnormally thin and conical-shaped cornea. This condition is quite rare (0.05 %) in a healthy population [151], but is common (15 %) among people with Down's syndrome [152]. The shape of the cornea of a keratoconus patient changes significantly until she/he becomes 30 years old, and is characterised by high amounts of coma, astigmatism and spherical aberration. An early population study was reported by Maeda et al. [153], who measured with a SHWFS a mean rms of 2.03 μm over a young population of 35 mild keratoconus eyes and a mean rms of 0.34 μm for 38 healthy eyes. Barbero et al. [154] adopted the laser ray-tracing approach, which does not have the limitation of the SHWFS in terms of dynamic range. Pantanelli et al. later measured a mean rms value of 2.24 μm for 35 abnormal eyes [22, 155]: 19 patients with keratoconus, and 14 patients with penetrating keratoplasty. A typical young and healthy eye does not have a large amount of high order aberrations (for a 6 mm pupil, around 0.3 μm of rms on average [57, 58]), and can easily be measured by a standard aberrometer after correction of the refractive errors.

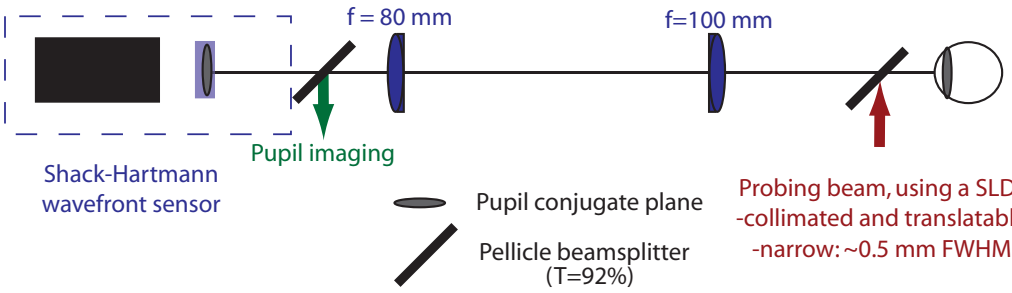

Figure 2.3: Alternative design for the aberrometer, without the scanner. This design is likely to be less efficient than our aberrometer for noise reduction, but does not need any field stop to block the reflections of the probing beam from the lenses $L1$ and $L2$ (See Figure 2.1). In practice, the dynamic range is therefore larger with this system than with our aberrometer.

The main advantage of our design (Figure 2.1), compared to the design of Figure 2.3, is the use of the scanner to reduce speckle. In theory, scanning the probing beam across the retina is more efficient for speckle reduction than using a low-coherence light source [36]. This issue should be addressed experimentally in a future study. Speckle was found in Section 2.3 to be a major source of noise. We quantified the speckle-reduction of our aberrometer, for the time-resolved measurements of ocular aberrations.

2.1.2 Alignment of the aberrometer

This section briefly describes the alignment of the aberrometer.

Adjustment of the longitudinal positions

An important feature of the aberrometer is to implement the principle of conjugation between the planes of the scanner, the lenslet array, and the camera that monitors the pupil of the eye. We have set the longitudinal position of these components by using a point source, located in a plane situated 100 mm in front of the lens $L1$. A sharp image of this point source was first imaged onto the camera that monitors the pupil, without any wander (although the scanning mirror was switched on). The longitudinal position of the SHWFS was then adjusted so that it would image the point source with no visible effect of the lenslet, as shown in Figure 2.4. The accuracy of these settings has been evaluated at around 1 mm for each element.

Alignment of the system

All lenses, especially the ones in the wavefront sensing part, are as much as possible used on their mechanical axis and over their central clear aperture. The wavefront sensing arm and the pupil alignment arm have to be mutually aligned with an accuracy much smaller than the spatial sampling. This was achieved by monitoring the data recorded by the two channels, using a collimated beam. The saturated patterns obtained on the SHWFS allowed us to reach an accuracy that was evaluated around 50 μm in the pupil plane of the eye. (See Figure 2.5.)

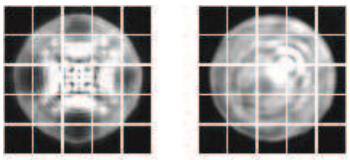

Figure 2.4: Patterns obtained on the SHWFS, when adjusting its longitudinal position. Left: The SHWFS is 1 mm out focus. Right: Correct longitudinal position of the SHWFS. The lenslet is conjugated to the point source, so does not leave a mark on the recorded pattern.

Reference with a point source

A point source is set at a distance 938 mm ($\pm$ 1 mm) in front of the plane of the exit pupil of the eye. The positions of the spots are stored and used as a reference.

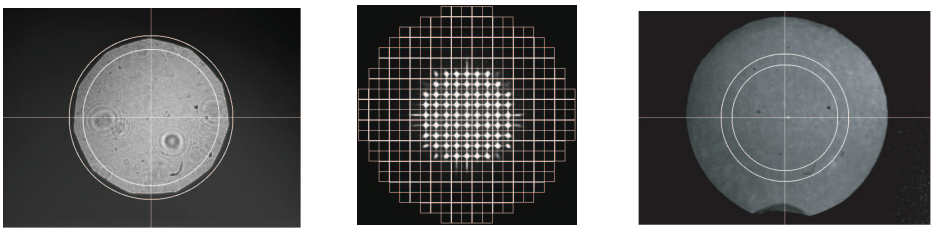

Figure 2.5: Data recorded on the pupil imaging CCD (left) and the SHWFS (middle), when aligning the aberrometer. Right: The pupil of a human eye (7 mm diameter).

Any measured wavefront can be converted into an absolute measurement by taking into account the divergence of the reference wavefront. For a measurement over a 5.4 mm pupil, we subtract the quantity $5.4^2/(16\sqrt{3}\times 0.938)$ to the Zernike coefficient $z_{2,0}$ measured in microns.

2.1.3 Tests using calibrated phase plates

Four phase plates (kindly supplied by Prof. S. Bará) have been used to test the aberrometer. These plates were supposed to simulate a typical ocular wavefront, with corrected sphero-cylindrical errors. Technical details about how these plates have been manufactured and other technical specifications can be found in the literature [105]. We first measured them over a 5.4 mm pupil with a high-resolution commercial Twyman-Green interferometer (Fisba Optik), using a collimated beam of diameter 10 mm in a double pass configuration (the measured wavefront is thus divided by two). The wavelength of this interferometer is 632.8 nm. A physical stop, slightly larger than the size of the measured pupil, was mechanically attached to the plate to make sure that the same region of the plate is afterwards measured by the aberrometer. An example of interferogram is shown in Figure 2.6.

The software of the interferometer was setup so that the measured wavefronts were oriented according to the standard for reporting ocular aberrations [156] (as an observer facing the eye of the subject would see the wavefront, and the sign of the wavefront is negative if it is delayed with respect to a perfect arbitrary wavefront coming out of the eye). The measured wavefront maps were imported into Matlab (here again it is important to check some scaling and orientation issues when importing the data), and a least-square estimation of 65 Zernike polynomials was performed (up to the tenth radial order). The definition of the Zernike polynomials that we use in this thesis also follows the standards proposed for aberrometry. These standards

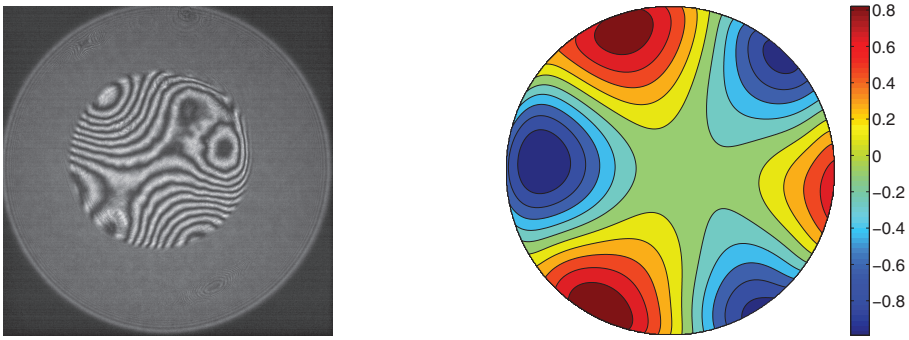

Figure 2.6: Left: Double-pass interferogram obtained for the plate 4 with the commercial interferometer. The physical aperture of the interferogram is 6 mm, and the measurement made over a 5.4 mm diameter. Right: Tip/tilt-removed wavefront in microns, as measured by our aberrometer, over a 5.4 mm pupil centred on the same physical stop.

define the ordering, the normalisation, and the positive orientation of the cartesian coordinate system (with the z axis oriented along the line of sight of the eye, and oriented as the beam coming out of the eye) [156]. The plate and the physical stop were then placed in the measurement plane of the aberrometer, and were back illuminated with a collimated beam that had been taken as reference for the aberrometer. The beam was obtained with a 635 nm monomode fiber and a 40 mm doublet. We measured a set of 65 Zernike coefficients (up to the tenth radial order). Figure 2.7 compares for each plate the Zernike coefficients (up to the fourth radial order) measured with the interferometer (solid lines) and the aberrometer ($*$). The rms residual error was computed for each of the four plates, using 63 Zernike coefficients. (Piston, tip and tilt are not included because they have no physical meaning in these comparative measurements). We found values of 0.047, 0.040, 0.032, and 0.060 μm for the plates 1 to 4. The values correspond on average to a rms error of $\lambda/10$ at a wavelength of 0.5 μm, which is a typical error budget for an aberrometer. The corresponding residual wavefronts do not have any significant impact on vision, even for an experienced subject. These errors might be due to the misalignment of the plate relative to each sensor. It is also possible that the two sensors have measured the plates with some small rotational misalignment (on the order of a degree), and the translational misalignments could be in the order of 100 μm (smaller than half the pitch of a lenslet of the aberrometer, or 10 pixels of the interferometer).

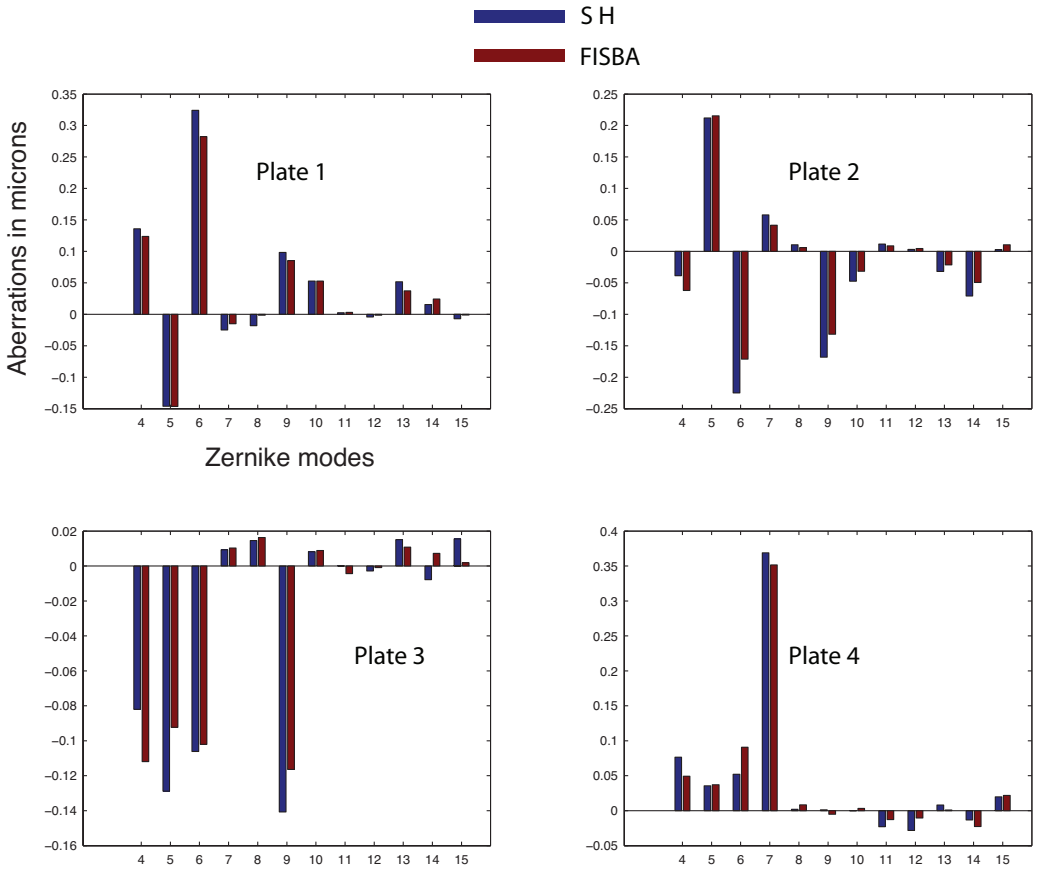

Figure 2.7: Zernike coefficients (up to the fourth radial order), as measured by the interferometer (red) and the aberrometer (blue).

2.2 Tests on the Shack-Hartmann wavefront sensor

Calibrating a SHWFS for open loop applications consists in knowing by how much one should scale an estimated shift of the Shack-Hartmann spot (pixel unit), in terms of local gradient of the wavefront (angle in radians). One can view the problem as taking the size of the pixel of the detector as granted, and trying to estimate the distance between the exit pupil of each lenslet and the detector plane. This distance is the one effectively used for scaling the estimated wavefront [16]. In a closed-loop AO system, this distance may be estimated with a large relative error, as the scaling of the reconstructed wavefront is only used for assessing the efficiency of the coupling between the wavefront sensor and the deformable mirror, and is not directly used in the closed-loop process. For an open-loop aberrometer, one has to define an error budget for the scaling the reconstructed wavefront. We aimed to calibrate the sensitivity of

our SHWFS with a relative accuracy better than 1%. For a typical eye as measured by Thibos et al. [57] (with a 0.3 μm rms of high order aberrations), such an uncertainty corresponds to a 30 nm error, which is acceptable. If the whole lenslet array is significantly tilted compared to the detector plane, one should calibrate this distance for each lenslet [157]. Using a proper mechanical mount, one can couple a lenslet array to a detector with such a good parallelism that the difference in the sensitivity from one lenslet to the other is not measurable.

When a SHWFS is designed with few pixels per lenslet, it is also important to adjust the translation of the SHWFS with respect to the detector. Doing so allows to define accurately the geometry matrix (see Chapter 4, Section 4.1). Given the large number of pixels used to sample each lenslet, we think that there is no need to have a sub-pixel accuracy in this setting. The XY positions of the lenslets are defined using the centroid positions of a collimated beam. The direction of this beam has to be carefully aligned with the mechanical axis of the Shack-Hartmann.

Another result discussed below is the investigation of the effect of the fill factor of the Microvista CMOS detector on the measurements of the centroid positions.

2.2.1 Calibration of the Shack-Hartmann wavefront sensor

For an open loop application of the SHWFS, it is important to calibrate the distance between the lenslet array and the detector plane (typically with a relative error of 1%). This distance defines the sensitivity of the SHWFS according to Equation 1.1. The lenslets of our SHWFS have a high F-Number (F = 37.5), and it is therefore practically impossible to adjust the position of the detector plane at the geometrical focus with an adequate accuracy. It is important to mention that, for such a high F-Number, the intensity of the Shack-Hartmann spot is relatively insensitive to the detector position and is maximal in a plane situated between the geometrical focus and the lenslet [158, 159].

To calibrate the sensitivity of the SHWFS, we have used an horizontal motorized translation stage that has a resolution of 10 nm. The output of a 780 nm monomode fiber was placed on this stage. The distance between the output of the fiber and the lenslet array of the SHWFS was measured with a relative accuracy of $\pm 0.1\%$ (1093 $\pm$ 1 mm). Each Shack-Hartmann spot was tracked over the whole field of view of its corresponding lenslet (18 pixels of the detector, corresponding to $\pm 0.7^{\circ}$). The increment of the displacement of the stage was 40 μm, which corresponds to 0.028 pixel at the de-

tector plane. We computed, for each lenslet, an averaged position of the detected spot from 20 single measurements, for each of the 600 positions of the translation stage. From the effective positions of the stage (in radians) and the corresponding measured row and column positions of the Shack-Hartmann spot i, we have computed the row and column sensitivities of each lenslet (r_i and c_i respectively) by a simple linear fit. The effective focal length f_i of the lenslet i was thus obtained using these measured sensitivities, and the known size Δ of a single pixel: $f_i = \sqrt{r_i^2 + c_i^2} \times \Delta$. The result for each lenslet is shown in Figure 2.8. The largest relative variation over pupil is 0.5% ($\pm$0.25%). Currently, these variations have been interpreted as artefacts and only the mean value of $f_l = 7.15$ ($\pm$0.02) mm is used for the wavefront reconstruction.

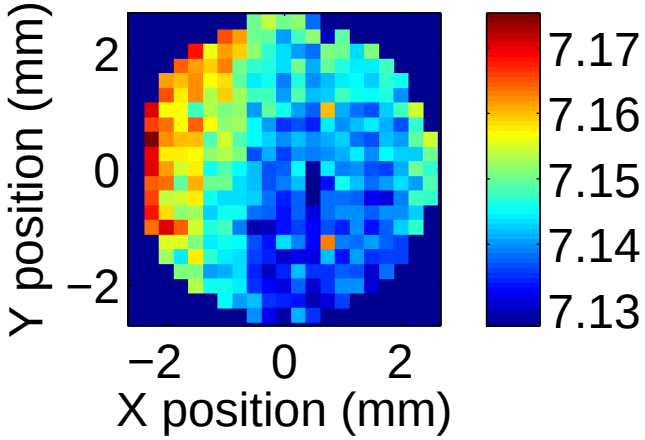

Figure 2.8: Effective focal length (in mm) for each of the lenslet of the Shack-Hartmann array, over a 5.4 mm pupil diameter.

2.2.2 Fill factor of the CMOS detector

The calibration of the SHWFS has been carried out twice, with the translation stage following the same path, but with the SHWFS flipped by 90°. The measured displacements were mainly along the columns of the CMOS detector for the first trial, and along the rows for the second trial. In terms of sensitivity of the lenslets, the two trials gave very similar results, but a difference was however observed for the residuals of the fits. Figure 2.9 displays the residuals of the tilts, as a function of the measured positions of the Shack-Hartmann spots. (top: residuals of the horizontal tilts as a function of the column positions; bottom: residuals of the vertical tilts as a function of the row positions). The horizontal non-linearities have an amplitude

of ± 40 μrad (± 0.03 pixels), and a pseudo-periodicity of 2 pixels. The vertical non-linearities are smaller, and vary more slowly (8 pixels of periodicity). These results suggest the surface that is dedicated to the reading of the electronic signal has light-insensitive vertical gaps. The influence of this light-insensitive surface is usually seen as a fundamental limitation of CMOS detectors, especially for a SHWFS.

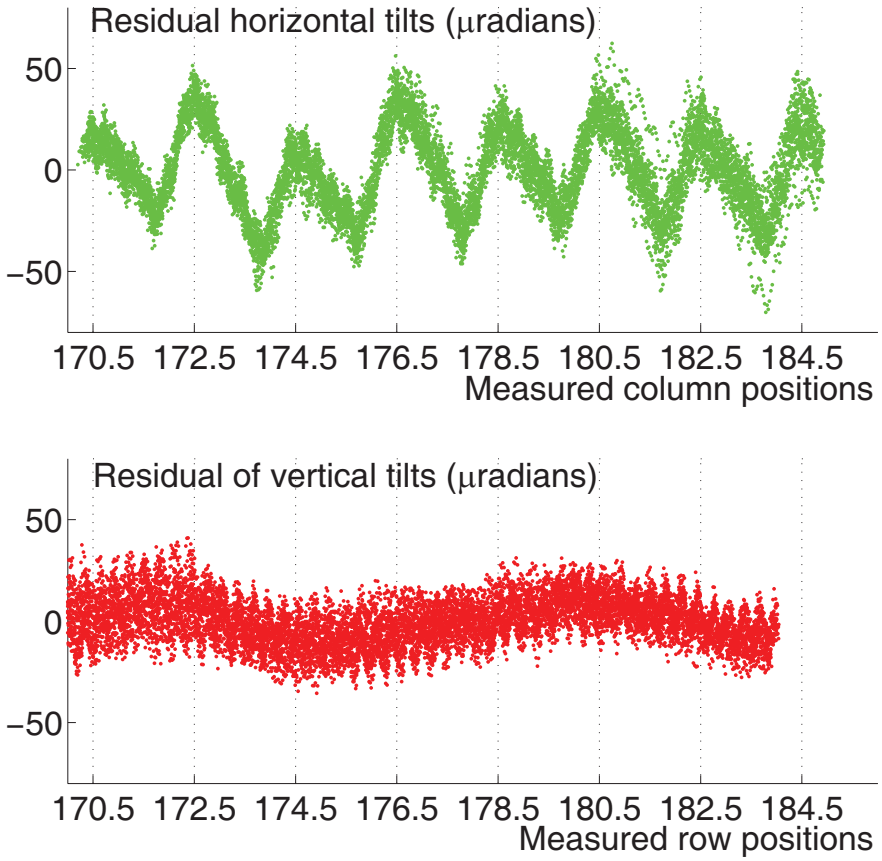

Figure 2.9: Non linearities observed when measuring pure horizontal and vertical tilted wavefronts, for 21 different lenslets. Top: horizontal tilts; Bottom: vertical tilts.

A (noise-free) numerical simulation has allowed us to estimate the fill factor of this detector. The Shack-Hartmann spots were modeled as Gaussian-shaped, with a FWHM $w = 2.4$ pixels (black and green) and $w = 3.5$ pixels (blue and red). The local window used for the detection algorithm has a size 15×15 pixels, and the true position of the Shack-Hartmann spots varies from 0 to 2 pixels in the horizontal direction, with an increment of 0.01 pixel. A FWHM $w = 2.4$ pixels corresponds to the FWHM of a diffraction-limited spot, like the one we measured during the calibration of the SHWFS. The data are first numerically modeled over a 750×750 pixel grid. The

sampling effect of the pixel of the CMOS detector is taken into account, by summation of grids of size 50×50 to create the signal of a single pixel of the detector. Only vertical light-insensitive gaps have been simulated, to illustrate the major trend of the data shown in Figure 2.9. An example of data simulated on the 750×750 grid is shown in Figure 2.10, for a vertical gap of width $0.2 \times \Delta$ (Δ being the size of a pixel of the CMOS camera: 10.8 μm), and a Shack-Hartmann spot of FWHM $w = 2.4$ pixels. Figure 2.11 shows the non-linearity introduced by gaps of widths $0.2 \times \Delta$ (black and red) and $0.12 \times \Delta$ (green and blue), in terms of estimated centroid position. The 0.03 pixel peak to valley non-linearity obtained for $w = 2.4$ pixels and $0.2 \times \Delta$ vertical gaps (black) corresponds to the experimentally measured value. The fill factor of the detector, which we define as the fraction of the light-sensitive surface of the detector, should thus be approximatively equal to $1 - 0.2/2 = 0.9$. The manufacturer of the camera specifies a 100% fill factor, thanks to the use of microlenses that focus the light on the light-sensitive area of the detector. For a SHWFS, it is likely that the use of microlenses do not completely cancel the effect of the light-insensitive areas of the detector. A detailed modeling of the CMOS structure would be required to investigate this point any further. Obviously, this requires a collaborative work with the manufacturer. Such a work was considered out of the scope of our project.

For $w = 3.5$ pixels (red and blue), the non-linearity becomes very small, on the order of 0.001 pixels peak to valley. Our aberrometer usually records Shack-Hartmann spots that have consistently a FWHM $w \simeq 3.5$ pixels. According to our simulations, the fill factor of our CMOS detector is thus high enough and does not introduce any significant error in the measurement of the centroid positions of Shack-Hartmann data obtained from real eyes.

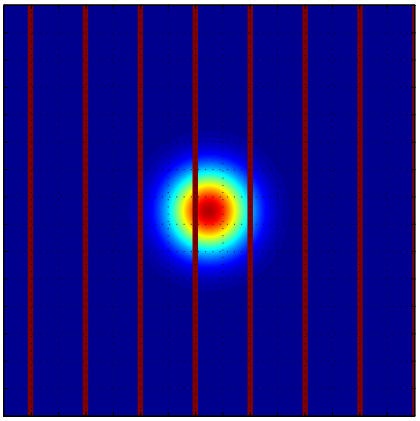

Figure 2.10: Simulation of a noise-free Shack-Hartmann data, for a CMOS detector with a 0.9 fill factor. The width of each insensitive vertical line is $0.2 \times \Delta$ the width of a pixel (red lines). The Shack-Hartmann spots have a FWHM $w = 2.4$ pixels. The size of the displayed data corresponds to the size of the local window defined for the calculation of the centroid positions: 15×15 pixels.

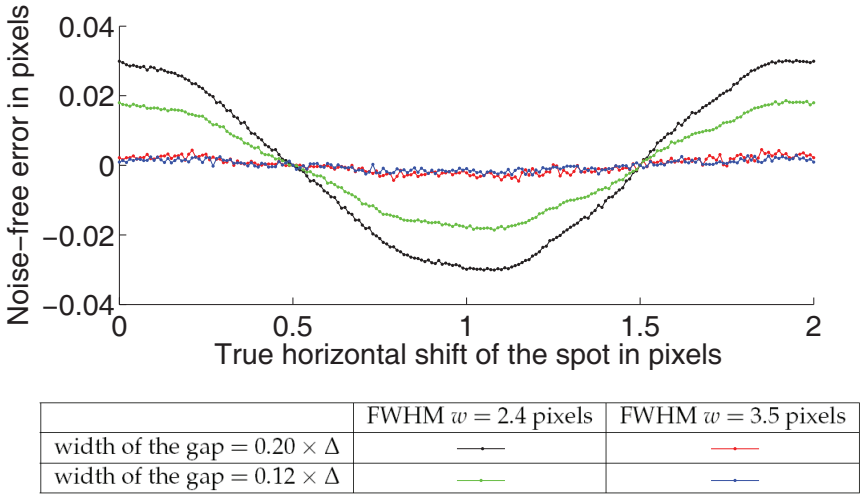

Figure 2.11: Simulation of the effect of light-insensitive vertical gaps in the CMOS structure, on the estimation of the Shack-Hartmann spot position obtained for the Gaussian-shaped Shack-Hartmann spots, with a FWHM equal to one (black and green) and one-and-a-half times (blue and red) the FWHM of the diffraction-limited spot ($w = 2.4$ pixels). The black and red curves correspond to a detector with vertical gaps of widths $0.2 \times \Delta$, the green and blue curves vertical gaps of widths $0.12 \times \Delta$.

2.2.3 Effects of reimaging the Shack-Hartmann spots

In this section we present briefly some results we obtained on a SHWFS that uses a $4f$ relay system to image the Shack-Hartmann spots onto the CCD. The main result is that such a relay introduces differences in the sensitivity of the lenslets, or non-linearities in terms of the measured wavefronts. The use of a relay system is therefore *not recommended* for any open loop application of the SHWFS. For the test system, the SHWFS consisted of a lenslet array of focal length 7.5 mm and pitch 200 μm. The lenses of the relay were two achromatic doublets of focal length 80 mm, as shown in Figure 2.12. The lenses had their concave surfaces facing each other, in order to optimise the imaging of each Shack-Hartmann spot. The Pixelfly qe CCD (manufactured by PCO) was the imaging detector of this SHWFS, which was working over a 5 mm pupil diameter.

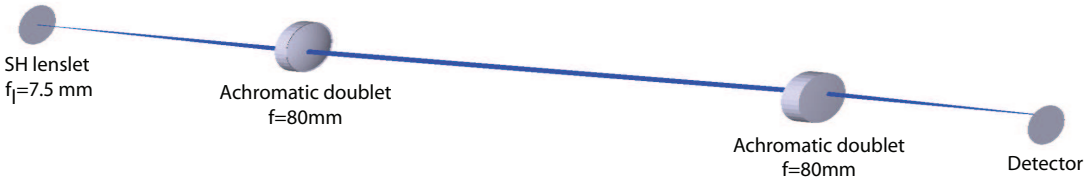

Figure 2.12: Relay system used to image the Shack-Hartmann spots on the detector.

A collimated beam of high optical quality was measured with the SHWFS, with various amounts of horizontal and vertical tilts. The measured high-order aberrations, computed as Zernike coefficients in microns, are plotted as a function of the corresponding measured tip/tilts in Figure 2.13 (green: horizontal tilt; red: vertical tilt). The x-axis corresponds to the Zernike tilts, as measured by the SHWFS. The main result is that an increasing amount of coma is measured when the incoming wavefront gets more tilted. The direction of the measured coma follows simply the direction of the introduced tilt. The amount of coma measured varies from -0.060 μm to +0.060 μm (as normalised Zernike coefficient, so $2\sqrt{8} \times 0.060 = 0.340$ μm peak to valley), for incoming tilts in the range of ± 10 μm, which corresponds to $\pm 0.45^\circ$ for

a 5 mm diameter pupil. The remaining aberrations (rms value that includes Zernike coefficients up to the tenth radial order) were quite modest and constant across the field, and are also shown in Figure 2.13. It represents a relatively modest error, but we decided that it could be easily avoided by not using any relay system. Stronger non-linearities can be measured, if for example the diameter of the measured pupil increases and the focal of the relay system decreases. The difference of sensitivity between lenslets can be calibrated, when a relay system is required to adapt the dimensions of the imaging detector to the lenslet array.

Simulations, also shown in Figure 2.13, were made using the ray-tracing software Zemax. Each lenslet of the Shack-Hartmann array was modeled sequentially, by modifying its centering with respect to the remaining of the relay system. Practically, the lenslet and the detector remained fixed, while the two lenses of the relay system were translated across the pupil. Each lenslet was used as the physical stop of the optical system, and the incoming tilt of the wavefront was introduced by modifying the field of the system. The Zemax-provided function for centroiding the energy of the different rays, in the fixed detector plane, allowed the simulation of the same operation usually carried out in the detector plane of the SHWFS. For each lenslet, the difference between the centroid obtained with an incoming wavefront on axis and the one obtained for a given field was computed. The reconstruction of the wavefronts, from these displacements of the spots, used the same functions as the ones that we use for the aberrometer. The results of the simulation appear in Figure 2.13, as the black line. They match the experimental results quite well in both directions. Coma was the only aberration predicted by the simulation when tilted wavefronts were used as input for the sensor.

The Zemax operands called the field curvature generalised sagittal (FCGS) and the field curvature generalised tangential (FCGT) are the longitudinal positions of the paraxial focus of the projection of the rays, in the sagittal plane (by convention the XZ plane), and in the tangential (YZ) plane. The two operands are defined for a given field angle (tilt of the incoming wavefront), and reflect the sensitivity of each lenslet after propagation through the relay system. The sensitivity of each lenslet along the X and Y direction is proportional to the FCGS and the FCGT respectively. Figure 2.14 illustrates the results provided by Zemax in terms of longitudinal position of the sagittal focus of each lenslet, across the 5 mm diameter pupil. The largest difference across the 5 mm pupil, in terms of sagittal focus, is 0.5 mm. This corresponds to a relative variation of the sensitivity of 7%, the nominal focal length of the Shack-Hartmann lenslets being 7.5 mm. If not taken into account, this non-linearity introduces large

errors in the reconstructed wavefronts.

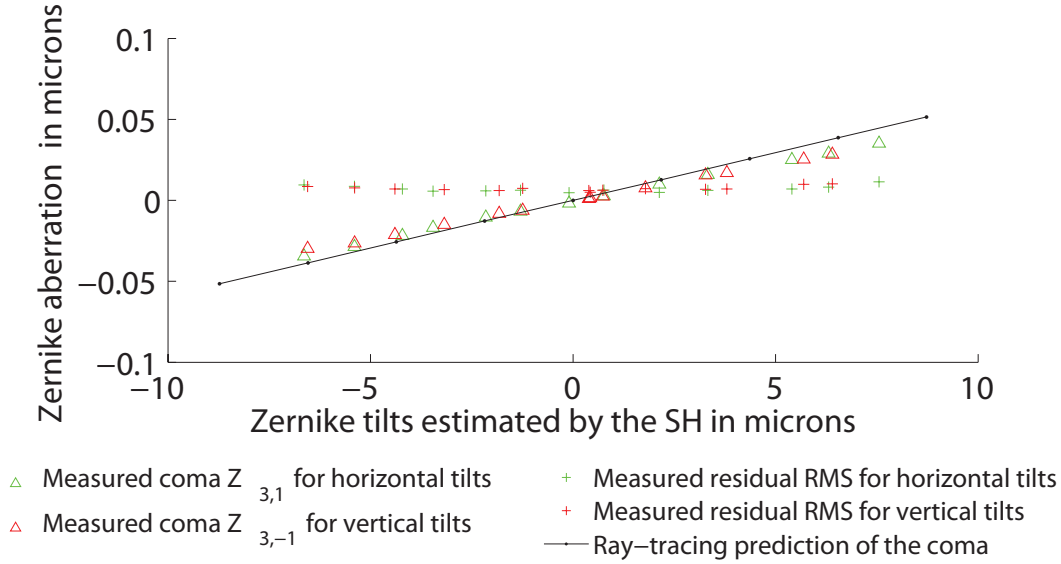

Figure 2.13: Non-linearity introduced by the relay system that images the Shack-Hartmann spots, as a function of the tilt of the incoming wavefront.

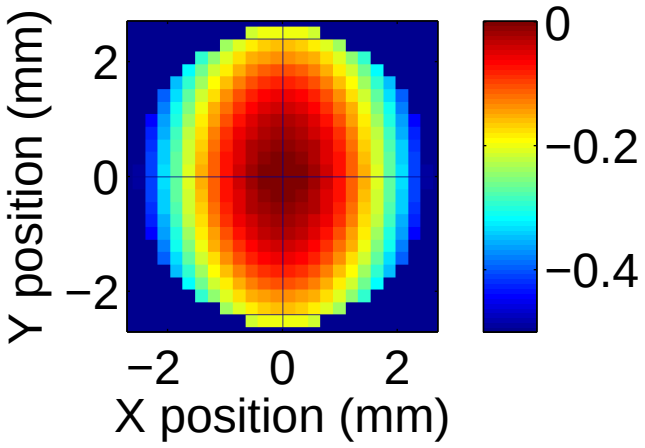

Figure 2.14: Longitudinal positions of the sagittal focus across the 5 mm pupil of the SHWFS simulated using a ray-tracing software, for a $[0°, 0°]$ field angle.

2.3 Efficient reduction of the effects of speckle

Scattering of the laser light is a significant nuisance in aberrometry. It originates from the deeper layers of the retina, and propagates up to the analysed pupil plane

of the eye. Two effects on the recorded Shack-Hartmann data can be distinguished. A first effect is the background light, the amount of which is very subject-dependant. This background cannot be easily disregarded, and creates some difficulties in the computation of the centroid positions. This issue is discussed in Chapter 3. A second effect is the speckled aspect of the recorded spots, and can be efficiently reduced using a scanning mirror in the pupil plane. We present in this section some of the tests we did with the scanning mirror. The results obtained for fully developed speckle tell us that the probing beam has to be as compact as possible on the retina, if one wants to minimise the effect of speckle in the pupil plane [36]. The probing beam of our aberrometer creates a laser beacon of diameter larger than the 30 μm diffraction limit, which is larger than the size and the spacing of the photoreceptors at the fovea (both are approximatively equal to approximatively 2 μm). As a result, the probing beam needs to be scanned across the retina so that a sufficient number of retinal structures are seen by the laser beacon. An example of data recorded without speckle reduction by our aberrometer on an uncorrected -2 D myopic subject is shown in Figure 2.15. The effect of speckle on the Shack-Hartmann spots is already apparent on the raw frames, although the spots are relatively homogeneous. With no scanner, the overall brightness of each spot is time-varying, with a characteristic time in the order of a second. The random variation of the phase might also be important, and a wavefront sensor with a fine spatial sampling might resolve these variations of the phase.

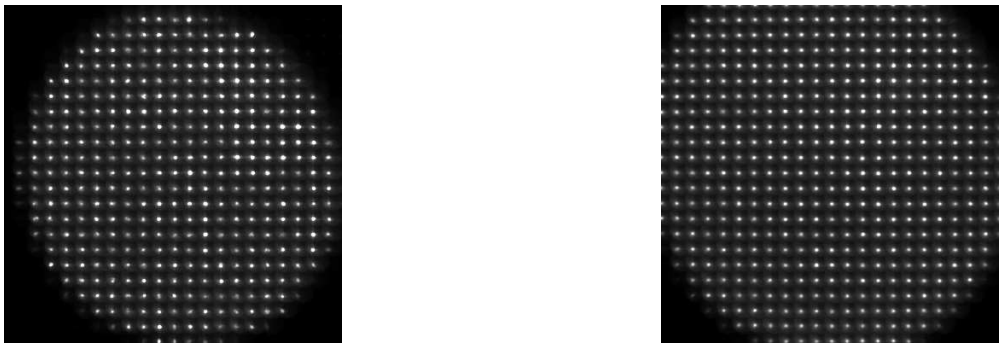

Figure 2.15: Typical Shack-Hartmann data collected at 100 Hz over a 5.4 mm pupil, without and with a scanner (left and right respectively). Scanning the probing beam reduces pupil constriction: the natural pupil is typically smaller without the scanner, even though the light level is the same (24 μW).

2.3.1 Frequency of the scanner

It is important that a single exposure of the CMOS detector corresponds to a multiple number of half-periods of the scanning mirror. Doing so ensures averaging the random variations of the optical field in the same way for each acquired data, assuming that there is no significant change in the scanned structures of the retina during the timescale of an exposure of the SHWFS. This setting has been tuned with an artificial eye that consisted of a 18 mm singlet coupled with an opaque screen in the focal plane. We summarise Table 2.3 the sampling parameters of our aberrometer, and the corresponding frequency of the scanning mirror.

Pupil diameter	Frame rate	Exposure time	Frequency of the scanner	Periods of scan per exposure
3.9 mm	173 Hz	2.89 ms	864.125 Hz	2.5 $\times$
5.4 mm	100 Hz	4.99 ms	800.825 Hz	4 $\times$

Table 2.3: Settings of the SHWFS and the scanner.

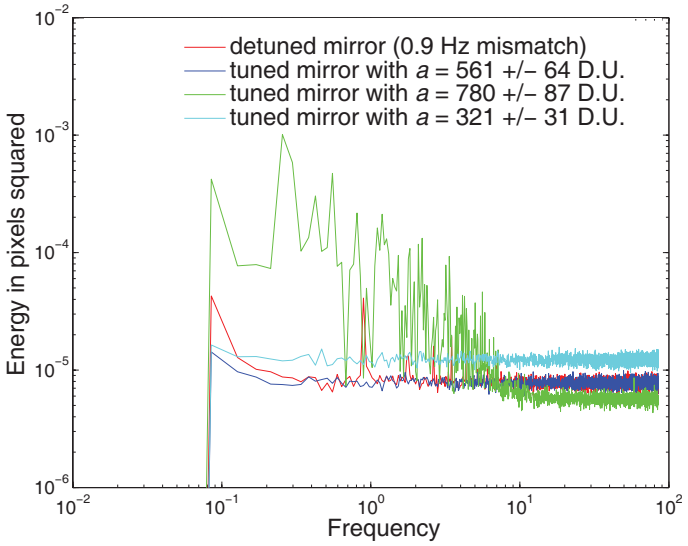

Figure 2.16: Energy spectra of the centroid position of the spot, computed with a 5×5 centroiding algorithm from data obtained on an artificial eye. Two important sources of jitter are pointed out in this graph: the mismatch between the frequencies of the scanner/exposure time of the CMOS (red), and the increase of the readout noise for bright spots (green, obtained for approximatively $a \simeq 800$ digital units).

Figure 2.16 displays the energy spectra of the centroid positions, computed from trials of 4000 frames obtained with the artificial eye at 173 Hz, and averaged across the different lenslets. In particular, the sensitivity of the aberrometer to a slightly

detuned frequency of the scanner (0.9 Hz) is illustrated by the red curve: peaks at different harmonics multiple of 0.9 Hz are one order of magnitude above the noise floor, for both the horizontal and the vertical components of the centroid position. At a frame rate of 173 Hz, the full 10 bit range of the detector should not be used, because an increase of the readout noise is apparent for bright Shack-Hartmann spots (see the green curve, for which the mean peak of the spot is $a = 780 \pm 87$ digital units). Note that with the 100 Hz configuration of our aberrometer, the full 10 bit range of the CMOS detector can be used without any noticeable amplification of the readout noise.

2.3.2 Amplitude of the scanner

To quantify the effects of speckle on the measurements of ocular wavefronts, we performed four 40 second-trials (100 Hz, 5.4 mm pupil) on a subject, for different peak to peak amplitudes of oscillation α of the scanning mirror: 2°, 1°, 0.5°, and 0°. We computed the energy spectra of the centroid positions, and averaged across the different lenslets. The results are displayed in Figure 2.17, and show that scanning the probing beam is very important. The spectrum obtained without scanning is approximatively reduced by a factor 65 when the maximal amplitude of scanning (2°) is used (see the blue curve: 2° scan, and the red curve: no scan). This is approximatively true for all the sampled frequencies, as the two spectra are shifted by an offset on a log-log scale. This implies that 65 independent areas are covered by the scanned spot.

For comparison we also display the spectrum of the noise of the system, obtained with an artificial eye and approximatively half the dynamic range of the camera (black curve: the mean peak of the spot is $a = 400$ digital units). For the highest sampled frequency (50 Hz), the noise of the system is still 75 times smaller than the measured signal on the human eye. This specification is "better" than the one reported by Diaz-Santana [108], who reported measurable (below the noise floor) dynamics of the aberrations up to 30 Hz. To beat the specification of Nirmaier [109] (measurable dynamics up to 70 Hz), our aberrometer has to work over the reduced 3.9 mm pupil. In this case, the measure dynamics of the ocular aberrations is still approximatively 50 times smaller than the noise level, at the highest sampled frequency (86 Hz).

The sampling, accuracy, and sensitivity are major properties of any wavefront sensor, and were described for our custom built aberrometer in this chapter. We also briefly discussed an issue specific to aberrometry: the reduction of the speckled aspect of the Shack-Hartmann data due to the retinal scattering. The scattering of the

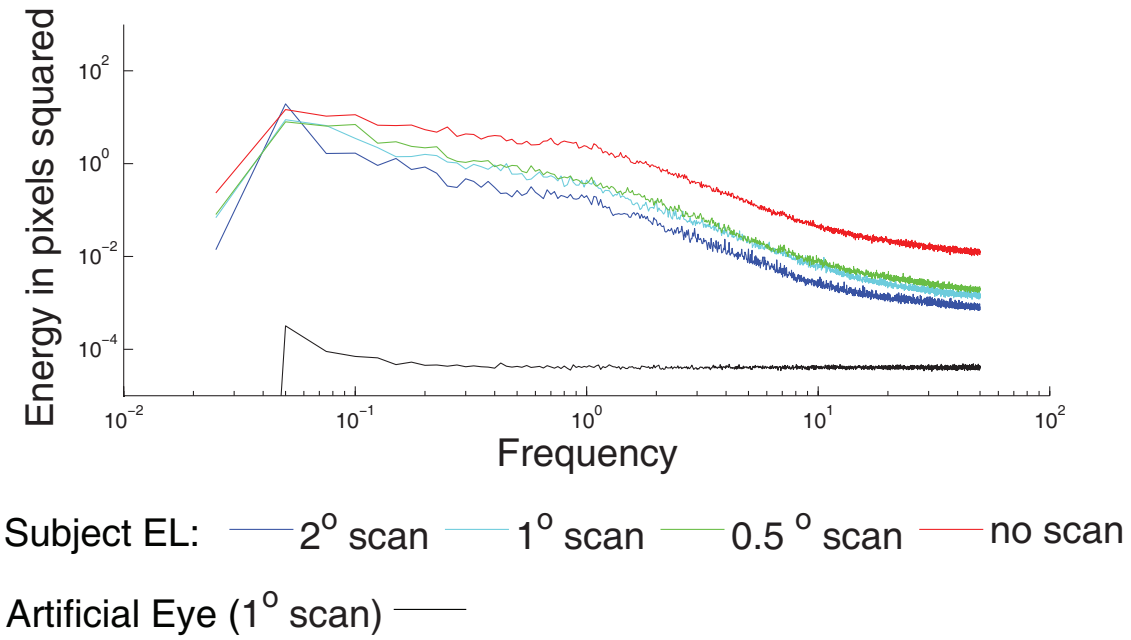

Figure 2.17: Energy spectra of the measured centroid positions for different amplitudes of the scanning mirror

measurement light also leads to some background on the raw data, which is not easily separated from the chore of the Shack-Hartmann spot. Chapter 3 aims to describe in a simple manner some key-issues in the process of estimating the centroid positions of the Shack-Hartmann spots from the raw data. We present a very classic modeling of the noise of the raw data, and stress the importance of having a linear (non-biased) algorithm. In particular, we discuss the influence of the background light on the linearity of a centroiding algorithm.

Chapter 3

Wavefront slope estimation for aberrometry of the eye

The SHWFS has a large number of ophthalmic applications, some of which have a great impact on the future life of the patients. Naturally, its performance has been questioned by many authors, usually for the problem of reconstructing the wavefront map from the measured centroid positions [16, 146–148, 160]. However, the measurement of the centroid positions is the core of the SHWFS, and corresponds to the largest reduction of data in the measurement process [17, 18].

This chapter briefly describes the CMOS data that have been recorded by our aberrometer during the study of the microfluctuations of accommodation, which is presented in Chapter 5. We present a simple modeling of the data, which we use to show that the matched filter is an estimator of the centroid positions that is well suited to aberrometry.

3.1 Modeling the Shack-Hartmann spot

3.1.1 Typical data

The signal to noise ratio of the aberrometer described in Chapter 2 is fairly insensitive to the measured ocular aberrations. This remark is illustrated by Figure 3.1, which shows the profile of a typical spot for an emmetropic subject in both the relaxed and accommodating states (subject CEL: left and right respectively), and for an artificial eye (18 mm singlet, with an opaque screen translated behind the back focal plane). The spread of the spot due to defocus is in both cases barely observable, although no optical correction of the defocus of the beam is applied within the aberrometer. With human eyes, the Shack-Hartmann spots have a depth of focus larger than with the artificial eye of similar effective focal length. The near-infrared laser beacon ($\lambda = 780$ nm) created in the fundus of the eye is probably spread among the different layers of the retina.

The background light in the data obtained with a SHWFS corresponds to the diffused component of the light scattered by the deeper layer of the retina (mainly some specular reflection by the sclera, and volumetric scattering in the 400 μm thick choroid [161]). It can be drastically reduced by introducing polarisers [162], or using a light source at shorter wavelength [163].

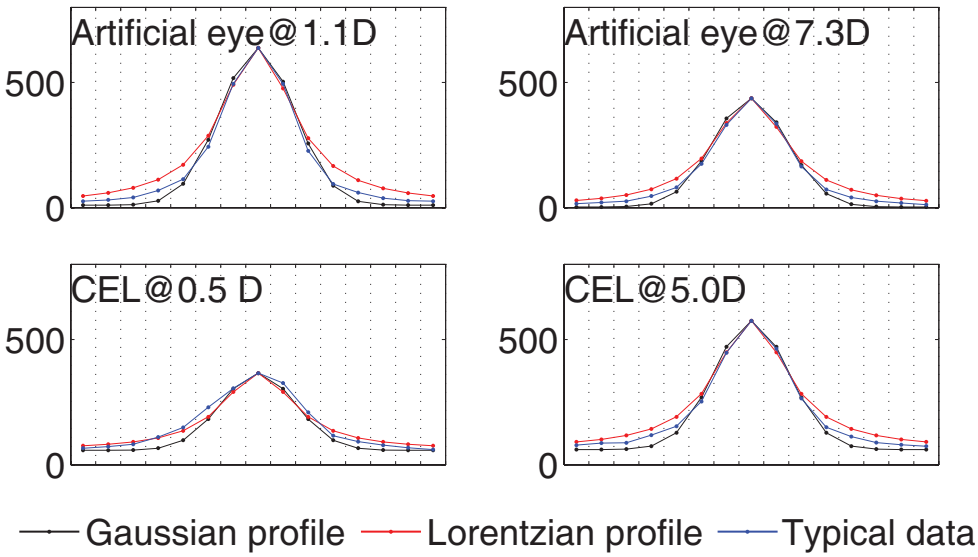

Figure 3.1: Typical Shack-Hartmann spot in a relaxed (left) and accommodative (right) states, with Lorentzian and Gaussian profiles surimposed (both of FWHM $w = 3.5$ pixels) .

3.1.2 Modeling

With our custom built aberrometer, the 0.2 mm pitch of a lenslet corresponds to 18.5 pixels of the CMOS detector, and the data are processed using 15×15 software windows. We model the 15×15 noise-free CMOS image typically recorded as a Gaussian profile with an additional homogeneous background. The FWHM of the simulated Shack-Hartmann spot is $w = 3.5$ pixels, the peak signal $a = 400$ (10 bit) digital units (DU), and the background $b = 50$ DU. These values are typical for our aberrometer, operating at 780 nm. The centroid position of the spot is parameterized by the 2-dimensional vector $\boldsymbol{\rho}$ (in pixels, with the center of the software window taken as origin). Only shifts smaller than 0.5 pixels are considered, which corresponds to accurately positioned software windows. We therefore assume that a preliminary measurement of the centroid position of the spot is made. This two step approach is very common for AO systems. The final estimation of the centroid position is obtained via the "second pass centroiding" [164] that we study in this chapter.

The noise that corrupts the CMOS data recorded by a SHWFS is described with combined Poisson and Gaussian statistics, in order to model the fundamental randomness of the detection and the processing of photoelectrons [165]. We write the mean data $\langle g_m \rangle$ recorded by the pixel m of the CMOS detector (in DU), at the position $[x_m, y_m]$ (in pixels):

$$\langle g_m \rangle = (a - b) \times \exp\left[-\frac{4\ln 2}{w^2}\left[(x_m - \rho_x)^2 + (y_m - \rho_y)^2\right]\right] + b \tag{3.1}$$

The main parameters of the detection of a single Shack-Hartmann spot are summarised on Table 3.1. Numerically, the mean number of photoelectrons k_m is used to generate a random number that follows a Poisson probability law, independent from one pixel to the other. A zero-mean Gaussian random number of standard deviation σ_{e^-} is added, to simulate the readout noise. The obtained number k_m corresponds to the number of electrons delivered by each pixel m, and can be converted into a digital unit to get a simulated data g_m by dividing by the gain G of the detector:

$$\begin{aligned} k_m &= \text{Poisson}\{\langle k_m \rangle\} + \text{Gauss}\{0, \sigma_{e^-}\} \\ g_m &= \text{Round}\left\{\frac{k_m}{G}\right\} \end{aligned} \tag{3.2}$$

Without refering to any estimator, this modeling can be used to investigate the best precision of the estimated centroid position $\widehat{\rho_x}$ one can obtain from a set of data,

Size of the processed images	15×15 pixels
FWHM of a typical spot	$w = 3.5$ pixels
Centroid of the spot	$\boldsymbol{\rho}$ pixels
Peak of a typical spot	$a = 400$ DU
Background light	$b = 50$ DU
Gain of the detector	$G = 30\ e^-/\text{DU}$
Readout noise of the detector	$\sigma_{e^-} = 40\ e^-$

Table 3.1: Numerical parameters that simulate the detection of a typical Shack-Hartmann spot, as recorded by our custom-built aberrometer.

using an unbiased estimator. The Cramér-Rao bound (CRB) defines this precision, and is a valuable tool that can be used as reference to test algorithms. The CRB is defined using the Fisher information matrix (FIM) $\mathbf{F}$ [165], which characterizes the statistical behavior of the data $\mathbf{g}$ for a given "true Shack-Hartmann spot" as modeled using Equation 3.1:

$$\mathbf{F} = \begin{pmatrix} \left\langle \left[\frac{\partial}{\partial \rho_x} \ln \Pr(\mathbf{g})\right] \left[\frac{\partial}{\partial \rho_x} \ln \Pr(\mathbf{g})\right] \right\rangle & \left\langle \left[\frac{\partial}{\partial \rho_x} \ln \Pr(\mathbf{g})\right] \left[\frac{\partial}{\partial \rho_y} \ln \Pr(\mathbf{g})\right] \right\rangle \\ \left\langle \left[\frac{\partial}{\partial \rho_x} \ln \Pr(\mathbf{g})\right] \left[\frac{\partial}{\partial \rho_y} \ln \Pr(\mathbf{g})\right] \right\rangle & \left\langle \left[\frac{\partial}{\partial \rho_y} \ln \Pr(\mathbf{g})\right] \left[\frac{\partial}{\partial \rho_y} \ln \Pr(\mathbf{g})\right] \right\rangle \end{pmatrix}$$

$\Pr(\mathbf{g})$ stands for the probability of obtaining the data $\mathbf{g}$, for fixed parameters a, b, w, and $\boldsymbol{\rho}$. The FIM has been analytically derived for the estimation of any parameter from data corrupted by combined Poisson and Gaussian noise [18]. We apply this result to the estimation of the centroid position of a Gaussian spot (described by Equations 3.1 and 3.2), and find in the zero-shift case:

$$\mathbf{F} = \frac{64}{(\ln 2)^2 w^4} \sum_{m=1}^{m=15^2} \frac{{x_m}^2 \times \langle g_m - b \rangle^2}{\sigma_{e^-}^2 / G^2 + \langle g_m \rangle} \times \begin{pmatrix} 1 & 0 \\ 0 & 1 \end{pmatrix} \tag{3.3}$$

The CRB is defined as a single diagonal element of the inverse of the matrix $\mathbf{F}$. In this case, we found the following expression for the CRB, in pixels squared:

$$CRB = \left(\frac{64}{(\ln 2)^2 w^4} \sum_{m=1}^{m=15^2} \frac{{x_m}^2 \times \langle g_m - b \rangle^2}{\sigma_{e^-}^2 / G^2 + \langle g_m \rangle} \right)^{-1} \tag{3.4}$$

To our knowledge, the CRB has been derived and used in several published papers related to the SHWFS [166–168]. This metric presents a valuable tool in any discussion on the fundamental nature of the data provided by of an instrument, as it does not

limit the analysis to a specific algorithm.

3.2 Estimators of the centroid position of the spot

3.2.1 Centroiding algorithms

Centroiding the data recorded by the Shack-Hartmann sensor is the most common method to estimate the wavefront slopes. We recall that this method is "physically justified", according to Equation 1.1, which we write here in a form simplified by the assumption of uniform intensity in the pupil plane:

$$\boldsymbol{\rho} = \frac{\int_{\mathbf{x}_2 \in \infty} \mathbf{x}_2 I(\mathbf{x}_2) d^2\mathbf{x}_2}{\Delta \times \int_{\mathbf{x}_2 \in \infty} I(\mathbf{x}_2) d^2\mathbf{x}_2} = \frac{f_l}{\Delta \times p^2} \int_{\mathbf{x}_1 \in L} \boldsymbol{\nabla} W(\mathbf{x}_1) d^2\mathbf{x}_1 + \boldsymbol{\rho}_{\mathbf{ref}} \tag{3.5}$$

p is the pitch of a lenslet, f_l the calibrated sensitivity of a lenslet, and Δ the size of a CMOS pixels (all in metres, see Table 2.2). $\mathbf{x}_1/\mathbf{x}_2$ are the coordinates in the pupil/detector plane (in metres), and $\boldsymbol{\rho}$ is the centroid position in pixel units (as in Table 3.1). The wavefront W is also in metres. Respecting these units is essential for the reconstruction of the wavefront map from the measured centroid displacements (see Chapter 4, for which we keep the same notations).

In principle, centroiding the point spread function of one lenslet over an infinite plane provides an unbiased estimation of the locally averaged wavefront slope. Practically, reduction of the recorded data is done by thresholding/windowing, and is unavoidable, because of the nuisance linked to the adjacent Shack-Hartmann spots. Aberrometers are designed with a large number of pixels per single lenslet (10×10 to 20×20), in order to cope with the extended nature of the Shack-Hartmann spots. As a result, a large number of noisy pixels do not carry any significant information about the measured wavefront, and can be responsible for a lack of precision in the estimation of the centroid positions. Methods to suppress irrelevant pixels mainly consist in applying rectangular/Gaussian weighting function [169–173] or thresholding the data [174–176]. These methods are susceptible to bias the estimated centroid positions if significant information is thrown away [168, 177–179]. The variance of a centroiding algorithm can be simply computed using the classical formula [180]:

$$\mathrm{Var}\{\widehat{\rho_x}\} = \left(1/\sum_{m=1}^{m=15^2} \langle \widetilde{g}_m \rangle\right)^2 \times \sum_{m=1}^{m=15^2} \mathrm{Var}\{\widetilde{g}_m\} \times [x_m]^2 \tag{3.6}$$

Equation 3.6 is derived under the assumption that the data g_m are statistically identical and independent from one pixel to the other. $\widetilde{\mathbf{g}}$ are the reduced data, obtained after thresholding/windowing the raw data $\mathbf{g}$. The variance $\mathrm{Var}\{\widetilde{g}_m\}$ can be computed under the assumption of combined Poisson and Gaussian noise: $\mathrm{Var}\{\widetilde{g}_m\} = \sigma_{e^-}^2 + \langle \widetilde{g}_m \rangle$. Like the CRB, the variance of a centroiding algorithm is computed for fixed parameters a, b, w, and $\boldsymbol{\rho}$.

We present in this chapter some results obtained with a simple centroiding algorithm that uses a rectangular window, of width R (in pixels), and a normalised threshold $0 \leq t \leq 1$. The threshold level is computed adaptively, from the minimum b and the maximum a of the 15×15 local data. The algorithm is illustrated in Figure 3.2. For $t = 0$, there is no effective thresholding of the data. For $t = 1$, the threshold level is $2a/3$. This algorithm has the advantage of being fast and easy to implement for real time application of the Shack-Hartmann with fine spatio-temporal samplings. We show in Section 3.3 that, for an ophthalmic application of the Shack-Hartmann, this algorithm should be carefully parameterised.

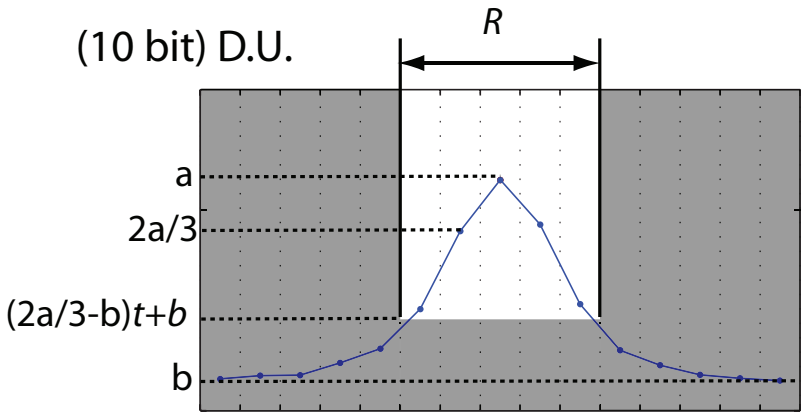

Figure 3.2: Parameterisation of a centroiding algorithm, with a normalised threshold t and a rectangular window of size R. The gray area corresponds to the data set to 0 before centroiding.

3.2.2 The matched filter algorithm

The matched filter algorithm estimates the shift that maximizes the scalar product of a reference image (typically a Gaussian mask) with the actual data [165, 181, 182]. The scalar product of the two images can be seen as a cross correlation and thus be computed using the Fourier transform, according to the correlation theorem.

The linearity of the algorithm can be understood with the Shannon sampling theorem and the concept of space-bandwidth product [183]. Both the data and its cross spectrum with the reference image should not be truncated. For Gaussian spots, this statement defines an interval of acceptable FWHM. For data of size 15×15 pixels, we find that $2 < w < 5$ pixels is an acceptable design. Figure 3.4 shows that the cross spectrum is significantly truncated for $w = 1.5$ pixels, which leads to the periodic error observed in Figure 3.3 (black curves).

Without a proper interpolation of the cross correlation function, this signal-dependant bias is also observed for correctly sampled Gaussian data ($2 \leq w \leq 5$ pixels). We do this interpolation by padding with zeroes the cross spectrum, so that the estimated cross correlation has 3 times the size of the original images. Figure 3.3 shows the effect of the interpolation of the cross correlation in terms of linearity, in the absence of noise. The interpolation reduces the noise-free error down to approximatively 0.001 pixels, for $w = 2.4$ and $w = 3.5$ pixels (green and red curves). For $w = 3.5$ pixels, the matched filter algorithm remains essentially linear for spots shifted up to $\rho_x = 4$ pixels. The sub-pixel accuracy of the estimated shift is obtained by a simple parabolic interpolation of the cross correlation function [181].

These simulations are very simple, as they do not take into account the possible mismatch between the reference image and the data. In practice, we found results that are very similar to Figure 3.3 when Lorentzian or diffraction limited spots are correlated with a Gaussian reference image. For a given FWHM, the linear range of the matched filter algorithm is slightly smaller for Lorentzian spots ($\rho_x < 3.5$ pixels) than for Gaussian spots ($\rho_x < 4$ pixels). Further investigations would be required to study the robustness of the matched filter algorithm to the asymmetry of the recorded spots. If it is found to improve significantly the estimation of the centroid positions, the spread and the asymmetry of the measured spots might be compensated by an adaptive matched filter algorithm. Such an algorithm is based on the modification of the reference image, in order to match the data with a lower residual error. This improvement might be relevant for the measurement of highly aberrated eyes.

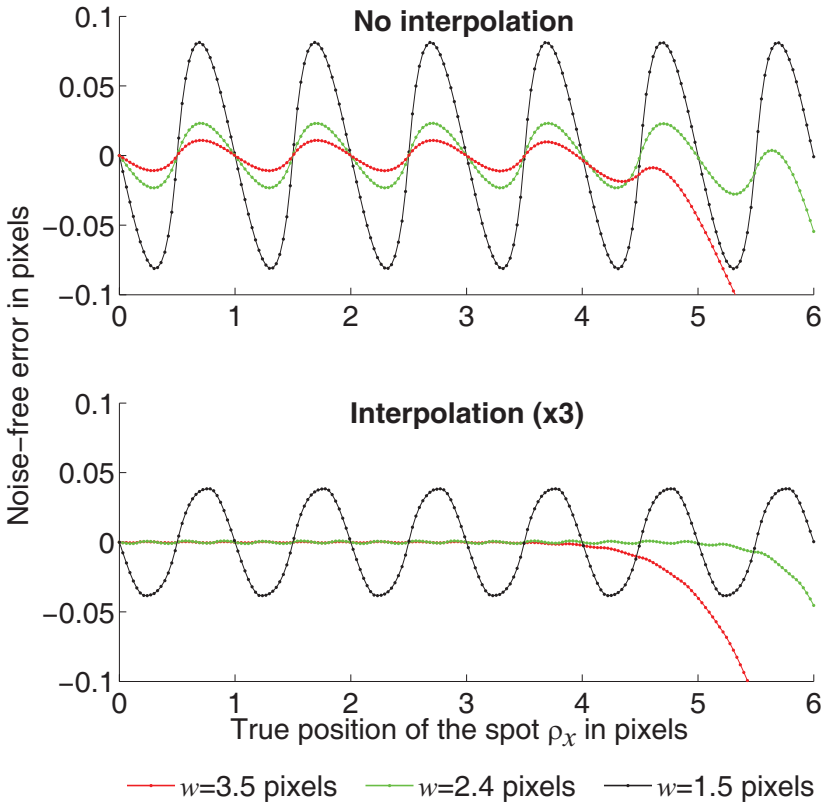

Figure 3.3: Noise-free error on the estimated spot position as a function of the true centroid position ρ_x of the Shack-Hartmann spot, for a Gaussian matched filter that has the same FWHM w as the Shack-Hartmann spot. $\rho_x = 0$ corresponds to the center of the software window.

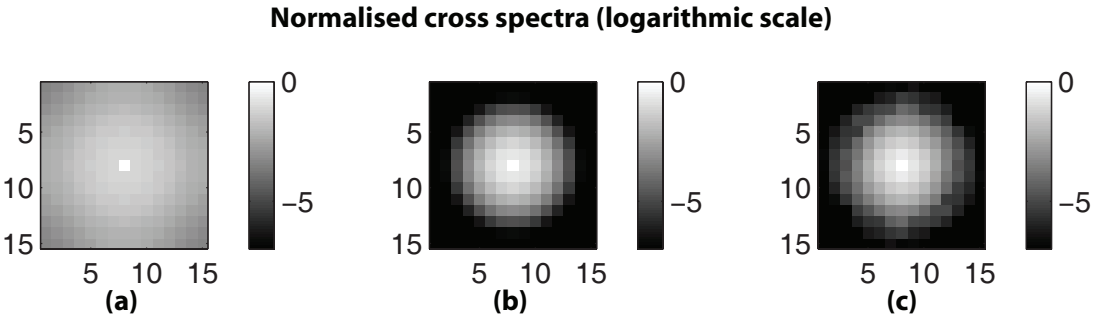

Figure 3.4: Illustration of the truncation of the cross spectrum, for $w = 1.5$ pixels (a). For $w = 3.5$ pixels, the cross spectrum is not truncated (b). Nor is the cross spectrum between typical data (obtained in a human eye) and a Gaussian reference mask of FWHM $w = 3.5$ pixels (c).

3.2.3 Precision of the centroid estimates

We compare in Figure 3.5 the variance of different centroid estimates to the CRB, with and without Gaussian noise (solid and dotted curves respectively). These simulations are relevant for the design of our aberrometer, because the readout noise of our CMOS detector is quite high ($\sigma_{e^-} = 40\ e^-$ rms: see Table 3.1).

The influence of the Gaussian noise is quite important for the $R = 15$ unthresholded centroiding algorithm (left graph), because many pixels with low signal to noise ratio are directly taken into account in the centroiding process. A common practice to partially suppress this white noise is to threshold the recorded data [174, 175]. In Section 3.3.3, we discuss how this thresholding should be done, using data recorded from human eyes. The main issue is to threshold correctly the background light, because of its local inhomogeneity.

One alternative to thresholding is to reduce the size of the window used for centroiding. Comparison of the variance of the $R = 15$ and the $R = 5$ centroiding algorithms shows that reducing the size of the rectangular window considerably reduces the effect of the readout noise. (See the red solid curves of the left and right graphs respectively.) The $R = 5$ centroiding algorithm has a variance lower than the CRB (both with and without readout noise). This is a clue that the $R = 5$ centroiding algorithm is significantly biased when the spot is not centred at $\boldsymbol{\rho} = \mathbf{0}$.

The matched filter algorithm performs very well in the presence of readout noise. The matched filter is an implementation of the ML estimator for data corrupted by Gaussian noise only [165], and its variance approaches the CRB in this case. The variance of the matched filter is very close to the CRB in the "Gaussian noise" regime (readout noise + low light level). (See the red and blue solid graphs, which are similar for $a < 300$ DU approximatively.)

For $a \simeq 400$ DU, we experimentally evaluate the precision of the matched filter estimates as a standard deviation of 0.006 pixels, using an artificial eye (a 18 mm lens, with an opaque screen in the back focal plane). This value is in agreement with the middle graph of Figure 3.5 (variance $\simeq 3 \times 10^{-5}$ pixels squared), and corresponds to a 2.5 nanometers rms error on the estimated wavefronts (with a modal reconstruction of 65 Zernike polynomials, up to the tenth radial order).

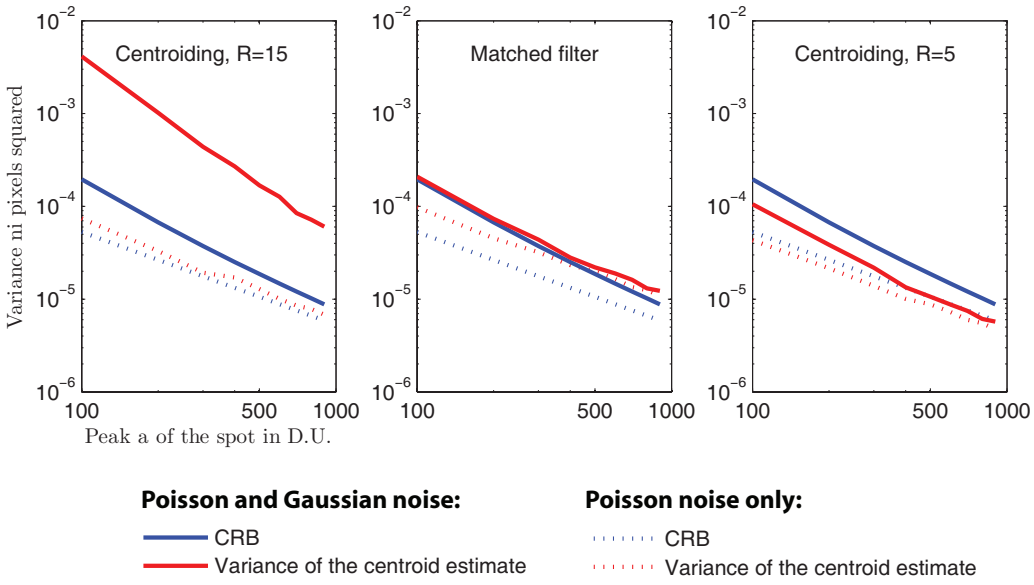

Figure 3.5: Variance of the centroid estimates, with and without the Gaussian noise of our CMOS detector. Each estimator (red curves) is compared to the CRB (blue curves).

3.2.4 Effect of background light on the centroid estimates

Because of the high signal-to-noise ratio of the data typically obtained with an aberrometer, the implementation of a linear algorithm is a fundamental issue in the design of our open-loop system. Near infrared light is commonly used for aberrometry [163], at the cost of an increased amount of scattered background in the recorded data. We show that a centroiding algorithm can be greatly affected by this background light. As an alternative, we propose to estimate centroid positions with the matched filter algorithm.

Figure 3.6 shows the Mean Square Error [165] (MSE, in pixels squared) in the estimated x-position of the centroid as a function of the shift of the spot ρ_x, using two unthresholded ($t = 0$) centroiding algorithms ($R = 5$ and $R = 15$) and the matched filter algorithm. For a peak signal $a = 400$ DU and a background $b = 50$ DU, the nonlinearity of the unthresholded centroiding algorithm is important, for both the $R = 5$ (red dots) and the $R = 15$ (blue dots) algorithms. The MSE increases with the amount of shift of the true spot. For $\rho_x = 0.5$, the error is around 0.33 pixels for $R = 15$, and 0.26 pixels for $R = 5$. For the $R = 15$ algorithm, this effect is due to the contribution

of the uniform background light, the centroid of which is in the middle of the processed window. As a result, the estimated position of the centroid is biased towards zero. Without background light, the $R = 15$ centroiding algorithm remains linear (blue solid graph), because there is no significant truncation of the Gaussian spot over the full $[0 - 0.5]$ pixels range of shifts. The $R = 5$ centroiding algorithm is not linear both with and without background light (red dotted and solid graphs respectively), because there is a significant truncation of the Shack-Hartmann spot by the 5×5 rectangular window. For $\rho_x = 0.5$, the error is 0.17 pixels without background, and 0.27 pixels with background. With background light, the error arises from a combined effect of the truncation of the Shack-Hartmann spot and the background.

The matched filter remains linear over the whole [0-0.5] pixels range of shifts, even with the background light. The MSE of the matched filter is higher with the background light, because it is subject to the combined Poisson and Gaussian noise. For a non-biased estimator, having a larger error (variance) when the contrast of the image decreases is "natural", and can be quantified using the CRB. Figure 3.6 demonstrates that great caution is required in using a centroiding algorithm in practice, even when "smart" centroiding (recursive variable threshold, variable width centroiding) is used. We illustrate this issue in the next section, using data obtained in human eyes.

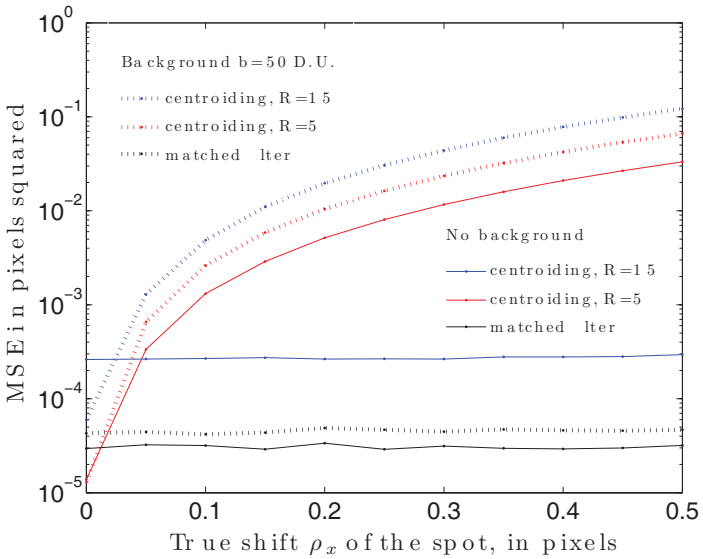

Figure 3.6: Simulation of the effect of an uniform background added to the mean data for two centroiding algorithms ($R = 5$ and $R = 15$, both with $t = 0$) and a matched filter.

3.3 Comparative study on human eyes

Taking the matched filter as a reference, we discuss in this section the performance of the centroiding algorithm, for data recorded on 5 human eyes. In particular, we confirm the large non-linearity of the unthresholded centroiding algorithm in the presence of background light. We also quantify the effect of the normalised threshold t on the centroid positions estimated by the centroiding algorithm.

3.3.1 Methodology

We measure 5 young subjects during a 1 second trial that has no occurrence of blinks, and we compute the difference $\boldsymbol{\Delta\rho} = \widehat{\boldsymbol{\rho}}_{cent} - \widehat{\boldsymbol{\rho}}_{mf}$ between the centroid positions estimated by the matched filter $\widehat{\boldsymbol{\rho}}_{mf}$ and the centroiding algorithm $\widehat{\boldsymbol{\rho}}_{cent}$. The centroiding algorithm uses a threshold t and a rectangular window of size R, which is positioned on the integer value of the centroid position $\widehat{\boldsymbol{\rho}}_{mf}$. We present in Table 3.2 the mean values of the peak a and the background b of the data, which are estimated for each subject by spatio-temporal averaging of the minimum and maximum values of the processed local data. The values presented in Table 3.2 are close to the values we used in the simulations of Section 3.2.4 ($a = 400$ DU and $b = 50$ DU).

Subject	a	b
1	466 ± 69	141 ± 7
2	419 ± 75	77 ± 4
3	375 ± 104	57 ± 5
4	399 ± 69	55 ± 5
5	458 ± 112	49 ± 7

Table 3.2: Estimated peak a and background b of the mean spot (in DU).

3.3.2 Non-linearity of the unthresholded centroiding algorithm

Figure 3.7 shows that the centroid positions $\widehat{\boldsymbol{\rho}}_{cent}$ ("$\cdot$") are systematically biased towards the centre of the software window, for $R = 9$ and no thresholding ($t = 0$). This effect is also apparent in Figure 3.8, which shows that the norm of $\boldsymbol{\Delta\rho}$ is proportional to the norm of the centroid positions $\widehat{\boldsymbol{\rho}}_{mf}$. The larger departures from a straight line obtained for the $R = 15$ centroiding algorithm (right graph of Figure 3.8) can be explained by the larger contribution of noisy pixels. Without any thresholding applied, the centroiding algorithm is barely sensitive to a sub-pixel shift of the

Shack-Hartmann spot, for any size R of software window.

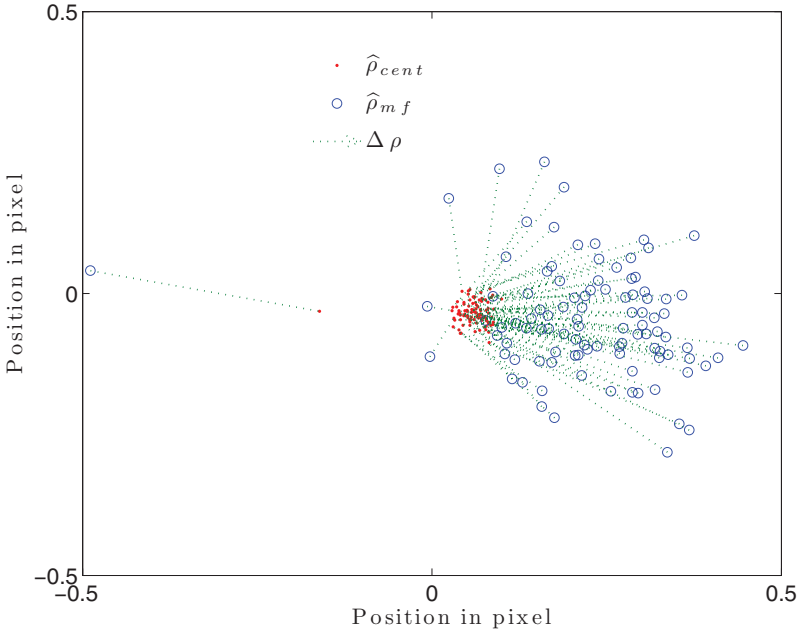

Figure 3.7: Centroid positions estimated by the matched filter ($\widehat{\rho}_{mf}$, "$\circ$") and by a centroiding algorithm. ($\widehat{\rho}_{cent}$: "$\cdot$", for $R = 9$ and $t = 0$.) Data collected on subject 2, with one single lenslet.

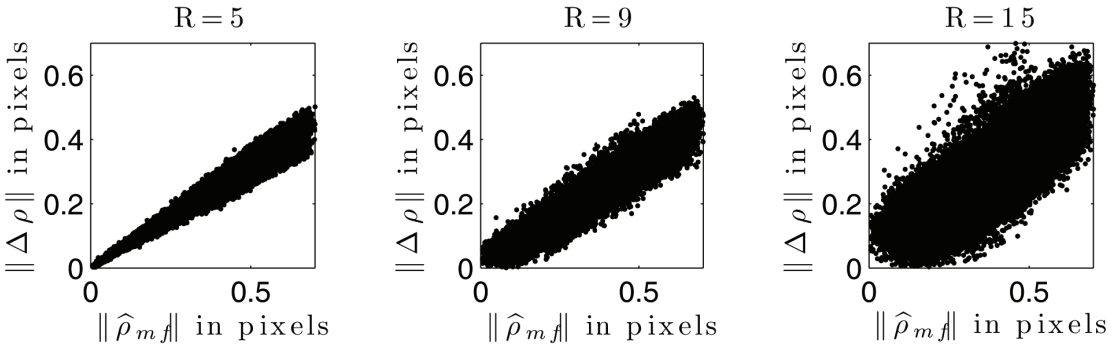

Figure 3.8: Signal dependant bias of the centroiding algorithm, for three different window sizes ($R = 5$, $R = 9$, $R = 15$) and no threshold ($t = 0$). Data collected on subject 2, using the 333 lenslets of the aberrometer.

3.3.3 Effect of thresholding

Thresholding is an effective way of reducing the effect of a Gaussian noise when computing a centroid position [174–176], although it can introduce large non-linearities for non rotationally-symmetric Shack-Hartmann spot [179]. Thresholding can also help to maintain the linearity of the centroid estimates because it suppresses the above described biasing effect of the background. To investigate the effect of thresholding on the estimates of the centroiding algorithm, we compute the rms of the norm of $\boldsymbol{\Delta\rho}$: $\sigma = \sqrt{\langle \|\boldsymbol{\Delta\rho}\|^2 \rangle}$, where $\langle\rangle$ denotes spatio-temporal averaging for a given subject. Figure 3.9 shows σ as a function of the threshold t. The centroiding algorithm with a $R = 15$ window and a low threshold provides estimates that are very different from the matched filter estimates (up to $\sigma \simeq 0.6$ pixels, for $t \simeq 0.2$). This peak in $\sigma(t)$ comes from the inhomogeneity of the scattered light, and is significant for these two subjects. Figure 3.10 shows the partially thresholded CCD data obtained with subject 2, for $t = 0.1$ (left) and $t = 0.2$ (middle). For these two subjects, the error is close to a minimum value for $t = 0.8$, independent of the size of the centroiding window R. Thresholding reduces the residual error of the centroiding algorithm, from approximatively $\sigma \simeq 0.3$ pixels ($t = 0$) down to $\sigma \simeq 0.13$ pixels ($t = 0.8$). The residual error does not fall bellow 0.13 pixels. For high threshold levels, the truncation of the spot leads to bias in the centroid estimates. (See the local data in Figure 3.10, obtained with a threshold level $t = 0.6$.) Regardless of t, the residual error is well above the 0.006 pixels precision of our aberrometer, which we experimentally measured using an artificial eye.

Figure 3.11 shows for 5 subjects the mean rms error of the tip/tilt removed residual wavefront, for $t = 0$ and $t = 0.8$. This residual rms is computed using a modal reconstruction of Zernike coefficients (up to the tenth radial order). A $t = 0.8$ threshold allows to consistently decrease the difference between the matched filter and the centroiding algorithm down to a mean error of 0.02 μm rms, for the 3 window sizes. Without thresholding, we found a mean value of 0.062 μm rms for $R = 15$, and 0.045 μm for $R = 5$ and $R = 9$. The propagation of the error in the estimated centroid positions as a residual wavefront depends on the geometry of the Shack-Hartmann sensor. The lenslet array of our aberrometer has a 7.15 mm focal length, the size of a pixel of the detector is 10.8 μm, and the sensor has 21 lenslets across the measured diameter.

The extended nature of Shack-Hartmann spots and the amount of background light obtained in human eyes justify the choice of the matched filter algorithm for aberrometry. Its close relationship to the least-squares estimator makes it also suitable for dealing efficiently with a larger number of pixels subject to Gaussian read-

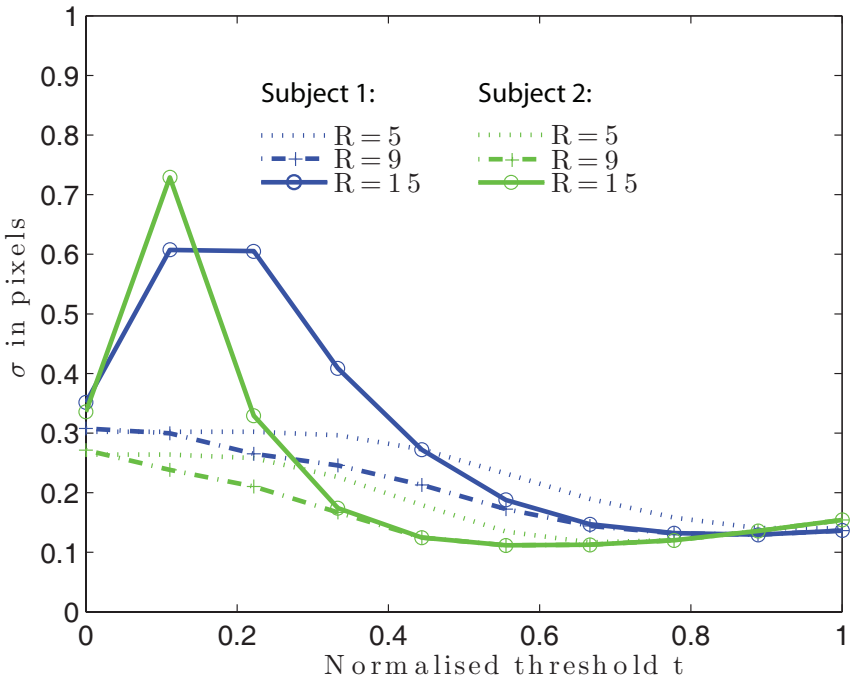

Figure 3.9: Rms difference between the centroiding algorithms ($R = 5$, $R = 9$, $R = 15$) and the matched filter, as a function of the threshold t.

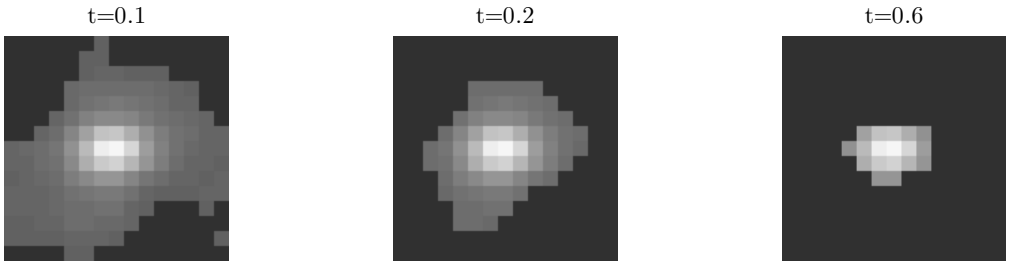

Figure 3.10: Thresholded data, obtained with subject 2 for 3 values of t. For $t = 0.1$ (left) and $t = 0.2$ (middle), the partially thresholded background leads to very large values of σ. (See Figure 3.9.)

out noise [165]. However, we have shown that the difference between the (tip/tilt removed) estimated aberrations becomes in the order of 0.02 μm rms when an appropriate thresholding of the data is applied before centroiding ($t = 0.8$), independently of the size of the rectangular window R. This residual error is not significant for most ophthalmic applications of the Shack-Hartmann wavefront sensor, as it corresponds to $\lambda/25$ for a 0.5 μm wavelength. Using MATLAB 7.4.0, we found our implementation of the matched filter algorithm 6 times slower than the centroiding algorithm, for the processing of 15×15 pixels images. For an adaptive optics system, the modest gain

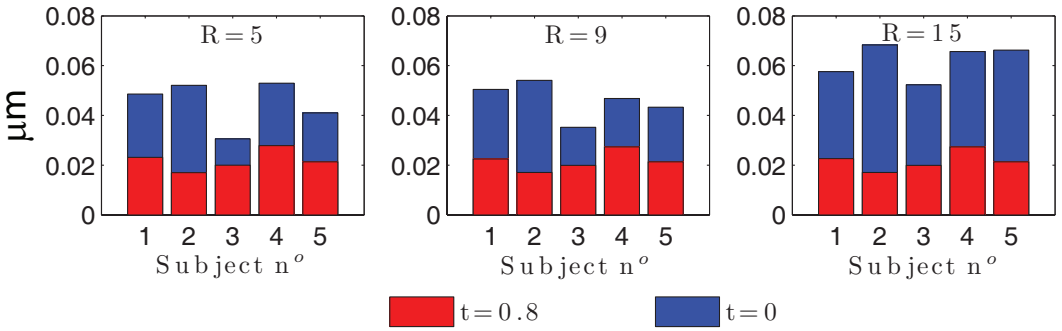

Figure 3.11: Tip-tilt removed difference between the wavefront reconstructed from a centroiding algorithm and the matched filter, for the 5 subjects, as a mean wavefront rms.

in accuracy obtained with the matched filter algorithm might therefore be obtained at the cost of a reduced bandwidth, unless appropriate parallel processing of the data is implemented (using field programmable gate arrays for instance). Without thresholding, the centroiding algorithm leads to centroid positions that are systematically estimated at the centre of the software window. With our custom-built aberrometer, we estimated the corresponding (tip-tilt removed) error between 0.045 and 0.062 μm rms.

Chapter 4 describes some key issues in the process of reconstructing a wavefront map from the measured centroid positions. In this context, the measured centroid positions are the raw data that are used to estimate some parameters that describe the wavefront.

Chapter 4

Wavefront reconstruction

Wavefront reconstruction is the inverse problem of estimating a set of parameters that describe a wavefront, from the measured centroid positions. The first section of this chapter presents the fundamentals of wavefront reconstruction, in a simple but detailed manner. We do not present any advanced technique for the reconstruction of ocular wavefronts, the reason being that too little is known about the statistics of the measurement process. We think that many subject-dependant issues and the non-stationarity of ocular wavefronts are likely to make such a model subject to unknown errors. Optimisation of a wavefront reconstruction method (for example, the number of Zernike modes) is a difficult task. It requires some knowledge of the statistics of both the noise and the signal, and the choice of a "risk", which depends on the scientific use of the measurements [165].

For the study of the dynamics of accommodation presented in Chapter 5, the curvature of the measured wavefront was computed as quantification of the instantaneous accommodative state of the eye. We thus present in this chapter a simple comparison of different methods to compute the curvature of ocular wavefronts.

We also discuss the coupling between Zernike modes that is induced by the shift of the pupil of the eye relative to the fixed pupil of an ophthalmic instrument. This effect plays an important role in the measurement of the dynamics of ocular aberrations.

To finish this chapter, we describe a method to extend the dynamic range of an aberrometer. Whereas the rest of this chapter shows the different artefacts inherent to

wavefront reconstruction methods, this algorithm stresses one of the main advantage of a modal reconstruction: even with missing centroid measurements, it is possible to estimate a wavefront map by interpolation. By performing a similar "modal interpolation" iteratively, one can process the complex spot patterns that are obtained when measuring a high amount of aberrations with a SHWFS.

4.1 Linear model of the SHWFS

The estimation of the wavefront map is an inverse problem that consists in finding an estimate of a set $\boldsymbol{\theta}$ of parameters that represent the true wavefront, from the measured centroid displacements $\mathbf{s}$. It is usually considered as a linear problem, which means that one can write a linear relationship between the measured centroids ($\mathbf{s}$), the true parameter of interest ($\boldsymbol{\theta}$), and the random error on the centroid measurements ($\boldsymbol{\nu}$) [146, 147]:

$$\mathbf{s} = \mathbf{A} \times \boldsymbol{\theta} + \boldsymbol{\nu} \tag{4.1}$$

For a number S of lenslets and N estimated components of $\boldsymbol{\theta}$, $\mathbf{A}$ is of size $2S \times N$. Each component (i, j) of $\mathbf{A}$ corresponds to the contribution of the j^{th} component of $\boldsymbol{\theta}$ to the i^{th} noise-free centroid position. Equation 4.1 might not be a good model for some applications of the Shack-Hartmann. Sources of non-linearity include inhomogeneity of intensity in the pupil plane [16], crosstalk of Shack-Hartmann spots [19], and aliasing effects in the measurements of $\boldsymbol{\theta}$ due to high spatial frequencies of the wavefront [18]. We put these issues aside, and write the general solution of the linear inverse problem:

$$\widehat{\boldsymbol{\theta}} = \mathbf{R} \times \mathbf{s}$$

For a complete (but straightforward) description of the estimation problem, we require a statistical modeling of the measurement noise $\boldsymbol{\nu}$. It is usually modeled with zero-mean Gaussian statistics, identically and independently distributed for each lenslet (so fully described by a single variance σ_ν^2, independently of the incoming wavefront). The zero-mean assumption requires to have a linear estimator of the centroid positions. Section 3.3 gives an example for which this assumption does not hold, because the centroid estimates are subject to a signal-dependant bias.

If the bias introduced by the wavefront reconstruction is negligible (see Section 4.2.1), the set of parameters $\widehat{\boldsymbol{\theta}}$ that minimizes the difference (in a least-squares sense) between the measured centroids ($\mathbf{s}$) and the modeling ($\mathbf{A} \times \boldsymbol{\theta}$) is the maximum likeli-

hood (ML) estimate of $\boldsymbol{\theta}$ [165]. It is computed by a simple least-squares fit on the data using the following reconstructor $\mathbf{R}$:

$$\mathbf{R} = (\mathbf{A}^t \times \mathbf{A})^{-1} \times \mathbf{A}^t$$

4.1.1 The zonal approach

In the zonal approach, the estimated parameter is a vector $\mathbf{W}$, which represents a wavefront map estimated at N points of the measured pupil. Three main geometries have been proposed by Fried [184], Hudgin [185], and Southwell [186]. Each geometry defines a $\mathbf{A}$ matrix (the "geometry matrix" [164]) by writing S implementations of the pair of equations displayed in Figure 4.1. For a closed-loop AO system, $\mathbf{W}$ is also the estimated control command, and Figure 4.1 describes the positioning of the actuators of the deformable mirror with respect to the lenslets of the wavefront sensor [164].

The Southwell geometry is the only geometry that samples the reconstructed wavefront in the middle of each lenslet. For the Southwell geometry, a set of averaged centroid displacements $\widetilde{\mathbf{s}}$ is computed before solving the inverse problem. The modified centroid measurements $\widetilde{\mathbf{s}}$ are thus correlated, so their covariance matrix $\mathbf{K}$ has to be taken into account in the reconstructor: $\mathbf{R} = (\mathbf{A}^t \times \mathbf{K}^{-1} \times \mathbf{A})^{-1} \times \mathbf{A}^t \times \mathbf{K}^{-1}$. We implemented this geometry for our zonal reconstructor, because the two others suffer from important artefacts.

The Fried geometry is known to suffer from its insensitivity to the so called waffle modes. These chessboard-like structures are apparent in the reconstructed wavefront, and introduced some complications in the optimization of the early astronomical AO systems [187, 188]. This aliasing problem simply comes from the local averaging of the wavefront difference in the linear model proposed by Fried. For example, the noise-free centroid displacements $(s_{x,1}, s_{y,1})$ are the same if the true wavefront (W_1, W_2, W_3, W_4) is equal to (1,0,0,1) or (0,0,0,0) (see Figure 4.1).

The Hudgin geometry assumes that the x and y components of the gradient of the wavefront are sampled at two different locations in the pupil plane. The Hudgin geometry is thus more suitable for a double-shear interferometer, but can be implemented using two SHWFSs that work in parallel [187].

Freischlad et al. [189] proposed one of the first implementations of a Fourier reconstructor, which uses suitable basis functions in the spatial frequency domain. Because

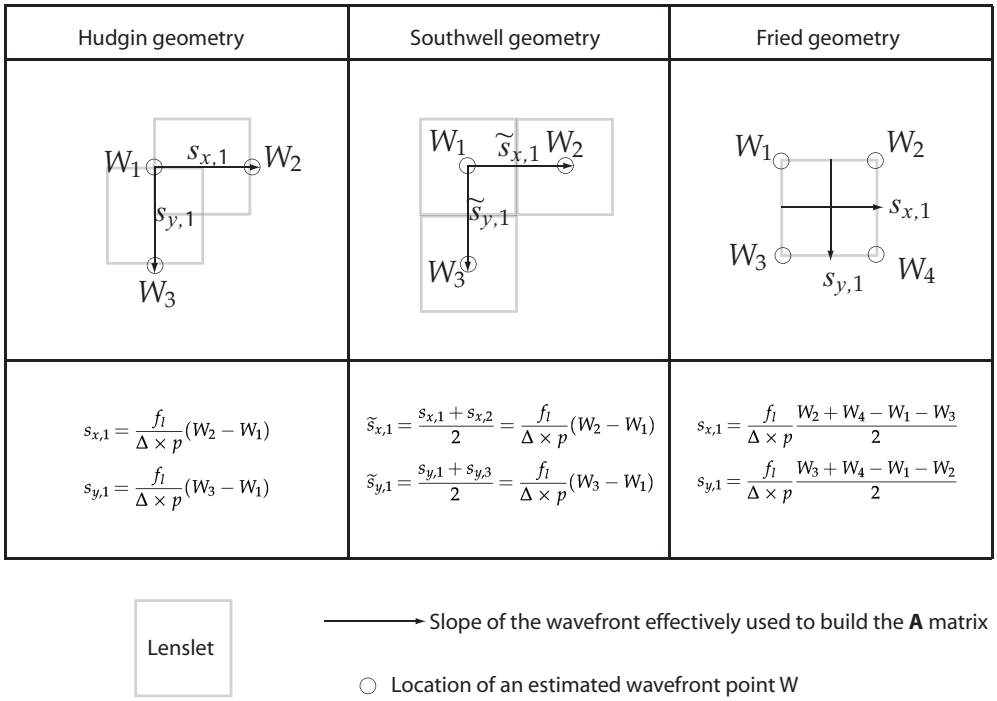

Figure 4.1: Each zonal approach models the reconstructed wavefront **W** (computed at the locations marked ∘, in μm) as a combination of the measured centroid displacements **s** (⟶, in pixels), which allows us to write the geometry matrix **A** (pixels.μm^{-1}). p is the pitch of a lenslet, Δ the size of a CMOS pixel, and f_l the calibrated sensitivity of a lenslet (see Table 2.2).

of the finite sized aperture, a Fourier reconstructor can introduce large errors in the reconstructed wavefront [190]. This so-called "boundary problem" is reduced by extrapolating the measured centroid positions outside the aperture, and setting some wrap-around centroid positions to enforce periodicity of the two-dimensional maps of the centroid positions [191]. Fourier reconstructors are useful for the real-time reconstruction of wavefronts using SHWFS with a large number of lenslets (like in an "extreme AO" system [192], with typically 128 lenslets across the diameter). The bias of a Fourier reconstructor is virtually zero when the number of lenslets is large [191].

4.1.2 The modal approach, using Zernike polynomials

Zernike polynomials are widely used in optics, mainly because they are orthonormal over a circular pupil. Zernike derived them for the theoretical analysis of his famous phase-contrast experiment [193], for which he was awarded the Nobel Prize. Each polynomial represents a balanced combination of Seidel aberrations with mini-

mum variance [61, 194, 195]. Interferometers classically used for optical testing, such as the Twyman-Green interferometer, provide a direct estimate of the wavefront map with a very fine spatial sampling (typically the 1000×1000 pixel field of a CCD). As a result, the orthonormality of the Zernike coefficients allows the engineer to estimate each coefficient independently of the other, typically using a least-squares fit. The orthonormality of the Zernike polynomials makes them useful when optimising the design of an imaging system. For a high quality imaging system, with a reasonably high Strehl ratio, optimizing each Zernike coefficient of the system is generally a good strategy. Most studies of ocular aberrations report that a fairly small number of Zernike modes can describe with a good accuracy typical wavefront maps. Of course, any discussion about the statistics of the ocular aberrations is biased by the measurement process [146, 147, 160, 196].

The construction of a (Zernike) modal estimator requires the assumption that the true wavefront $W(\mathbf{x})$ can be accurately approximated with N Zernike polynomials over the measured pupil:

$$W(\mathbf{x}) = \sum_{k=1}^{k=N} z_k Z_k(\mathbf{x}) \tag{4.2}$$

The modal geometry matrix $\mathbf{A}$ is defined by combining Equations 4.2 and 3.5:

$$A_{s,n} = \frac{f_l}{\Delta \times p^2} \times \int_{\mathbf{x} \in L(s)} \frac{\partial Z_n(\mathbf{x})}{\partial x} d^2\mathbf{x}$$

$$A_{s+S,n} = \frac{f_l}{\Delta \times p^2} \times \int_{\mathbf{x} \in L(s)} \frac{\partial Z_n(\mathbf{x})}{\partial y} d^2\mathbf{x}$$

for $1 \leq s \leq S$ and $1 \leq n \leq N$. A good method to make sure that there is no error in the numerical implementation of the $\mathbf{A}$ matrix is to compute the expected deviation of all Shack-Hartmann spots (in CMOS pixels, for the 5.4 mm configuration of our aberrometer), for a tilted plane wavefront (Zernike $z_{1,-1} = 1$ μm):

$$\rho_y = \frac{PV \times f_l}{\Phi \times \Delta} \simeq 0.504 \text{ pixels}$$

Φ is the diameter of the pupil in the plane of the Shack-Hartmann array. It is computed using the number of pixels across the software pupil, and the size of a CMOS pixel. For the 5.4 mm configuration of our aberrometer, $\Phi = 4.28$ mm (se Tables 2.1 and 2.2). PV is the peak to valley amplitude of the wavefront, and is 4 μm. We make sure that all the non-null values of the first column of the $\mathbf{A}$ matrix are equal to 0.504. Note that if the scaling and the sign of the $\mathbf{A}$ matrix are valid for the tilts ($z_{1,-1}$ and

$z_{1,1}$, which correspond to the first and second columns of $\mathbf{A}$), they are also valid for all other Zernike terms (because the "code that builds $\mathbf{A}$" is the same for all Zernike polynomials). It is however necessary to make sure beforehand that the numerical implementation of the gradients of Zernike polynomials is free of errors.

4.2 Wavefront reconstruction errors

4.2.1 Modeling and bias

For both zonal and modal reconstructors, we refer to the bias b as the noise-free error on the overall set of estimated parameters. We define b as the norm of the difference between the mean estimates $\widehat{\boldsymbol{\theta}}$ and the true parameters $\boldsymbol{\theta}$, obtained after a sufficiently large number of repeated measurements of the same wavefront,

$$b(\boldsymbol{\theta}) = \| \langle \widehat{\boldsymbol{\theta}} \rangle_{\mathbf{s}|\boldsymbol{\theta}} - \boldsymbol{\theta} \| \tag{4.3}$$

Zonal bias due to the assumption of "locally plane" wavefronts

Quite intuitively, the three zonal approaches all correspond to an approximate modeling of the SHWFS. They assume that the centroid position is proportional to the difference between the wavefront sampled at two points. We recall that the noise-free centroid position (for any unbiased estimator) is proportional to the locally averaged gradient of the wavefront. This fundamental principle of the Shack-Hartmann was fully described by Equation 1.1, which we simplified to Equation 3.5 under the assumption of uniform intensity in the pupil plane.

We compute the bias b introduced by the assumption of "locally plane" wavefronts, for the Southwell geometry and a SHWFS with 11, 21, and 31 lenslets across the diameter of the measured pupil. Different ensembles of wavefronts are simulated: Kolomogorov-like wavefronts (using a code given by R. A. Johnston [197]), and ocular wavefronts (using a multivariate Gaussian model derived from the population study of L. Thibos [57], for Zernike coefficients measured over a 6 mm pupil). The noise-free positions of the Shack-Hartmann spots are computed by a numerical implementation of Equation 3.5. The geometry of the detection of a single Shack-Hartmann spot is the same for each sensor, and corresponds to the SHWFS of our custom-built aberrometer. (See Table 2.2.) The measurement plane and the SHWFSs are thus conjugated with different magnifications. The number of CMOS pixels is: 208×208, 396×396,

Wavefronts	11 Lenslets	21 Lenslets	31 Lenslets
D/r_0=20	0.091	0.053	0.038
D/r_0=10	0.051	0.030	0.021
D/r_0=5	0.029	0.017	0.012
D/r_0=2.5	0.016	0.009	0.007
Thibos et al. (6 mm)	0.058	0.014	0.008

Table 4.1: Noise-free error due to the assumption of "locally plane" wavefronts, inherent to a zonal reconstructor. This error is computed in μm, from 100 samples of each ensemble of wavefronts. These results are obtained with a Southwell geometry. (See Figure 4.1.)

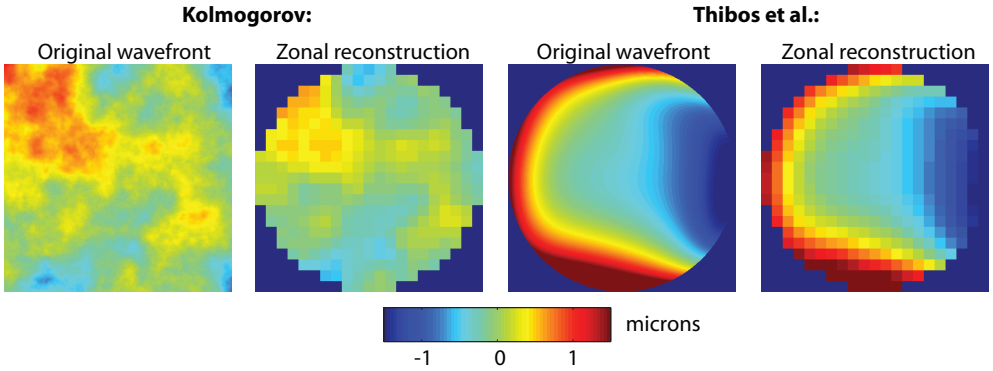

Figure 4.2: Example of wavefronts (in μm) simulated to obtain the results of Table 4.1. The turbulence-corrupted wavefront corresponds to D/r_0=10, and the ocular wavefront is typical for a 6 mm pupil (with corrected refractive errors). The zonal reconstruction is obtained for a Southwell geometry, and a Shack-Hartmann with 21 lenslets across the diameter.

and 586×586 for 11, 21, and 31 lenslets across. Examples of simulated wavefronts are shown in Figure 4.2. For each ensemble of wavefronts, we compute a (noise-free) ensemble averaged rms error: $\sqrt{\langle b(\mathbf{W})^2 \rangle_{\mathbf{W}}}$. The results are shown in Table 4.1. For the measurement of atmospheric turbulence at low light level, a SHWFS is typically designed with a number of lenslets across the aperture equal to D/r_0. The relevant errors in Table 4.1 would thus be: 0.053 μm (for $D/r_0 = 20$ and 21 lenslets) and 0.030 μm ($D/r_0 = 10$ and 11 lenslets). For a typical ocular wavefront as measured by Thibos et al., the use of a zonal reconstructor with 11 lenslets across the diameter is not recommended (the error is 0.058 μm, so $\lambda/8.5$ at $\lambda = 0.5$ μm). For a closed-loop AO system, we recall that the sensed residual wavefront tends towards zero (if the loop is working), which minimises gradually the impact of the bias given in Table 4.1.

Modal bias: aliasing effects of the non-estimated Zernike modes

The least-squares estimate of the Zernike coefficients $\widehat{\mathbf{z}}$ is inbiased if the true wavefront has no significant Zernike terms of degree higher than N. We define $\mathbf{z}$ as the set of Zernike coefficients (of size $Q \times 1$, $Q > N$) that describes accurately the true wavefront. The bias $b(\mathbf{z})$ introduced by an inadequately low number N of estimated Zernike coefficients can be directly computed using a $\mathbf{B}$ matrix (of size $N \times Q$), which depends on the geometry of the sensor [146, 147, 160]:

$$b(\mathbf{z}) = \|\mathbf{B} \times \mathbf{z}\| \qquad \text{With: } \mathbf{B} = \mathbf{R} \times \mathbf{A} - \mathbf{I}_{N,Q} \tag{4.4}$$

Where $\mathbf{I}_{N,Q}$ is the identity matrix, of size $N \times Q$. The bias expressed by the $\mathbf{B}$ matrix is a direct consequence of the non-orthogonality of the Zernike modes in the $2S$-dimensional measurement space. The scalar product between the different Zernike modes in the SHWFS measurement space can be directly read in the $\mathbf{A}^t \times \mathbf{A}$ matrix ($N \times N$ elements), which would be diagonal if Zernike polynomials were orthogonal in the SHWFS measurement space. Each column of the $\mathbf{A}$ matrix is a $2S \times 1$ vector, which corresponds to the noise-free measurement of a pure Zernike aberration (with a 1 μm rms). Figure 4.3 shows an example of the $\mathbf{B}$ matrix (left, for $N = 27$ and $Q = 65$) for our aberrometer with 21 lenslets across the diameter. The bias is only proportional to the non-estimated modes, and typically the overall bias $b(\mathbf{z})$ decreases when the number of estimated modes increases. The $\mathbf{A}^t \times \mathbf{A}$ matrix is also shown in Figure 4.3 (right) for $N = 65$ estimated Zernike modes and 21 lenslets across.

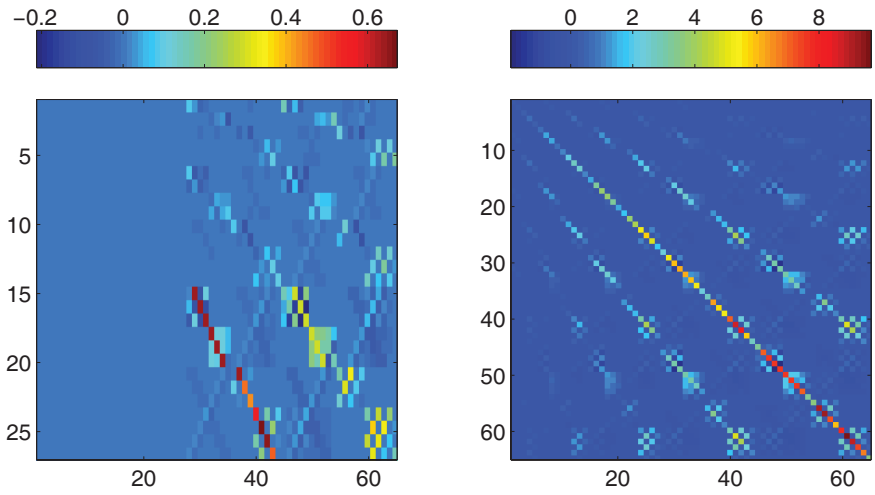

Figure 4.3: Two matrices that illustrate the non-orthonormality of the Zernike coefficient in the measurement space, for our aberrometer with 21 lenslets across. Left: matrix of bias $\mathbf{B}$ (for $N = 27$ estimated Zernike, and $Q = 65$ significant Zernike modes in the true wavefront; no unit). The first 27 columns of $\mathbf{B}$ are filled with zeroes. Right: Scalar product $\mathbf{A}^t \times \mathbf{A}$ of 65 Zernike in the measurement space, in pixel^2.μm^{-2}

4.2.2 Propagation of the measurement noise

The linear modeling of the SHWFS also allows us to quantify the propagation of the measurement noise as a wavefront random error [146, 147]. Under the assumption that the measurement noise ν follows independent and identical Gaussian statistics (zero-mean, standard deviation σ_ν in pixels), $\widehat{\boldsymbol{\theta}}$ follows a multivariate Gaussian distribution, described by a covariance matrix $\sigma_\nu^2 \times \mathbf{R} \times \mathbf{R}^t$. The mean of this distribution depends on $\boldsymbol{\theta}$, and is in general affected by the aliasing effects described in the previous paragraph [146, 147]. The covariance matrix of $\widehat{\boldsymbol{\theta}}$ is independent of the true wavefront. Its trace is the sum of the variance of the N components of $\widehat{\boldsymbol{\theta}}$ (σ_N^2 in μm^2), and quantifies the measurement noise as a wavefront error. The overall MSE $\varepsilon(\boldsymbol{\theta})$ in the estimation of the wavefront parameter $\boldsymbol{\theta}$ can be written as the combination of the bias $b(\theta)$ and the noise σ_N^2 [146, 147]:

$$\varepsilon(\boldsymbol{\theta}) = \sigma_N^2 + b(\boldsymbol{\theta})^2 \tag{4.5}$$

Equation 4.5 describes the well-known trade-off common to most estimation problems. The overall error is the sum of the measurement noise, which typically increases with the number of estimated parameters, and a bias term, which decreases with the

number of estimated parameters. For a modal reconstruction, this idea is the motivation for using a suitable basis ("Karhunen-Loève functions") that describes efficiently (with a reduced number of terms) a given statistical ensemble of wavefronts [165,198].

We simply characterise the propagation of the measurement noise as a "noise factor", which we define as σ_N^2/σ_v^2 (in μm^2.pixel^{-2}). This scalar corresponds to the overall variance of $\widehat{\boldsymbol{\theta}}$ (in μm^2) that would be measured from the repeated measurements of any static wavefront, for a measurement noise $\sigma_v = 1$ pixel. In general, the noise factor is closely related to the condition number of the matrix $\mathbf{A}^t \times \mathbf{A}$, and the number of estimated parameters. Table 4.2 gives some numerical examples of the noise factor, with the three SHWFSs considered for Table 4.1. Increasing from $N = 27$ to $N = 91$ estimated Zernike modes increases the noise factor by approximatively a factor 4.5, 2, and 1.5 for 11, 21, and 31 lenslets across. For a zonal reconstructor, the number of estimated parameters is linked to the geometry: with 11 lenslets across the diameter, the noise factor is approximatively half the noise factor with 21 and 31 lenslets across. The relevance of these numbers will depend on the level of measurement noise σ_v. For the measurements of ocular aberrations over a 5.4 mm pupil, our aberrometer has 21 lenslets across and we typically use 65 Zernike modes. We thus have a noise factor of 0.03 μm^2.pixel^{-2}. With a measurement noise $\sigma_v \simeq 0.01$ pixels (we typically measured $\sigma_v \simeq 0.006$ pixels with an artificial eye), we find that the noise is $\sigma_N \simeq 0.002$ μm (which is negligible).

	11 Lenslets across	21 Lenslets across	31 Lenslets across
Zonal (Southwell)	0.04	0.08	0.08
91 Zernike modes	0.14	0.04	0.03
65 Zernike modes	0.05	0.03	0.03
27 Zernike modes	0.03	0.02	0.02

Table 4.2: "Noise factor" σ_N^2/σ_v^2 in μm^2.pixel^{-2}, for 27, 65, 91 estimated Zernike modes, and a zonal reconstructor (Southwell geometry). For the four reconstructions, the noise factor corresponds to the (tip/tilt removed) random error in μm^2 due to a measurement noise $\sigma_v = 1$ pixels.

During the 40 second measurement trials that we performed for the project described in Chapter 5, the centroid positions of Shack-Hartmann spots with low signal were not computed. For a modal reconstruction of the wavefront, one method to deal with this problem is to suppress the rows of the matrix $\mathbf{A}$ that correspond to the missing centroids, and do the matrix inversion to compute the reconstructor $\mathbf{R}$. The major problem of this method is the increase of the noise factor. This effect depends on the the number of lenslets of the SHWFS, the number of reconstructed Zernike

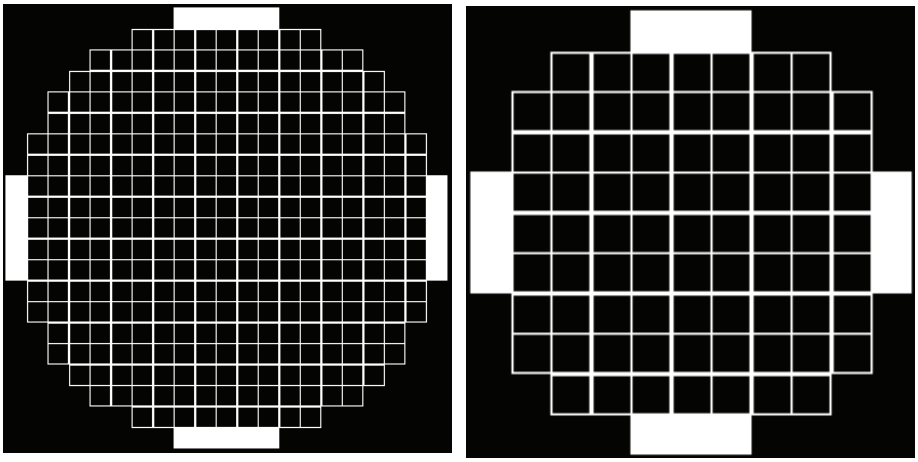

Figure 4.4: SHWFSs with 21 lenslets across (left) and 11 lenslets across (right), and some missing centroid values that are marked by white squares. For the estimation of $N = 65$ Zernike modes with 11 lenslets across, the noise factor increases because of the missing centroids, from 0.05 to 12 μm^2.pixel^{-2}. The geometry with 21 lenslets across is robust to the missing centroids: the noise increases from 0.03 to 0.04 μm^2.pixel^{-2} only.

modes, and the positions of the missing centroids. Figure 4.4 shows an example of centroids that are missing at the edge of the pupil for 11 and 21 lenslets across. For the estimation of $N = 65$ Zernike modes with 11 lenslets across, the matrix $\mathbf{A}^t \times \mathbf{A}$ is ill-conditioned and the noise factor becomes very large (12 μm^2.pixel^{-2}). Computing a reconstructor $\mathbf{R}$ for each recorded frame can thus make a SHWFS unstable and slow. (The matrix inversion is very computationally expensive.)

One alternative is to interpolate the missing centroids. With a modal reconstructor, this is fairly straight-forward. We note $\mathbf{s}_0$ the set of measured centroid positions, with zeros that correspond to the missing values. $\mathbf{R}$ and $\mathbf{A}$ are the reconstructor and the geometry matrix of the SHWFS (with no missing spots). The product $\mathbf{A} \times \mathbf{R} \times \mathbf{s}_0$ gives the interpolation of the missing centroid positions, which can be combined with the effectively measured centroids to form a vector $\mathbf{s}_1$. One can then estimate the Zernike modes: $\widehat{\boldsymbol{\theta}}_1 = \mathbf{R} \times \mathbf{s}_1$. This process can be done iteratively, but the convergence should be very fast in most cases.

4.2.3 Computation of the accommodative response

The main application of the aberrometer described in Chapter 2 is the measurement of the dynamics of ocular aberrations. Intuitively, these dynamics depend on the

method of wavefront reconstruction. Most of Conor Leahy's modeling was usually applied to a limited number of Zernike modes (15 terms, at most). In particular, we found it interesting to study the dynamics of accommodation, the statistics of which vary greatly with what we refer to as the "accommodative effort" in Chapter 5. The "accommodative response" is meant to be the instantaneous focus position of the eye (in the object space).

Defining the longitudinal position of focus of an aberrated optical system is a relatively complex issue. A single ray, in the exit pupil of an optical system, does not necessary intercept the optical axis. The projections of this ray in the sagittal and tangential plane do intercept this axis and define two different foci, which are specific to this ray. The next paragraph illustrates the impact of the definition of the accommodative response on a single measurement trial. This problem is closely related to the problem of computing the spherical refractive error using a wavefront map.

"Paraxial" and "rms" wavefront curvatures

The "paraxial curvature" of the measured ocular wavefront can be used as an objective estimation of the spherical refractive error [57, 62] and the accommodative response. The paraxial curvature a (in dioptres) is the curvature of the wavefront of an optical system, for which the pupil is set as small as possible. It is therefore computed from the Seidel defocus of the wavefront $s_{2,0}$ and the pupil diameter Φ:

$$a = \frac{8 \times s_{2,0}}{\Phi^2} \tag{4.6}$$

One can also compute the paraxial curvature using Zernike coefficients. Doing so is an approximation, because an infinite number of Zernike modes contain a quadratic term r^2.

$$a = \frac{4}{\Phi^2} \times \left(4\sqrt{3}z_{2,0} - 12\sqrt{5}z_{4,0} + 24\sqrt{7}z_{6,0} - 120z_{8,0} + 60\sqrt{11}z_{10,0} + ...\right) \tag{4.7}$$

Using more radially symmetric Zernike modes in Equation 4.7 amplifies the noise of the estimated accommodative response, and there is a tradeoff between the precision and the accuracy of the estimated response.

Figure 4.5 shows that the time series of the accommodative response are similar, for Zernike and Seidel reconstructions *of same radial order*. For the Seidel reconstruc-

tion, the difference between the accommodative response at the different radial orders comes uniquely from the least-squares fit. For reconstructions up to the sixth radial orders and higher, the noise on the accommodative response seems too high. It is interesting to note that the corresponding reconstructions (6, 8, and 10 radial orders) seem to converge well in terms of local means (or slow trends of the response). This might suggest that the paraxial curvature should be optimally computed at the sixth radial order. We adopted a more conservative approach, and computed the accommodative response with Equation 4.7 at the fourth radial order.

The computation of the curvature using Equation 4.7 at the second radial order corresponds to the curvature that minimises the rms of the wavefront ("rms curvature"). It is significantly less noisy than the other reconstructed responses, but does not follow the slow-varying drifts obtained with the other reconstructions.

Mean wavefront curvature

One alternative to the paraxial curvature is the "mean curvature", which is directly estimated without wavefront reconstruction:

$$\begin{aligned} a &= 0.5 \times \langle [a_x(i,j) + a_y(i,j)] \rangle_{i,j} \\ a_x(i,j) &\propto [s_x(i+1,j) - s_x(i,j)] \\ a_y(i,j) &\propto [s_y(i,j+1) - s_y(i,j+1)] \end{aligned} \tag{4.8}$$

i and j refer to the position in the pupil plane, s_x and s_y the local slopes of the wavefront, and a_x, a_y the local curvatures. The factor of proportionality in Equation 4.8 can be numerically estimated by simulating the noise-free slopes of a spherical wavefront. In the absence of higher order aberrations, Equation 4.8 gives $a \simeq 0$ for a purely astigmatic wavefront ($z_{2,0} = 0$, or $M = 0$ using the notation of power vector [57, 199, 200]). The accommodative response, as computed with Equation 4.8, is also shown for subject ED in Figure 4.6. For the experimental study described in Chapter 5, we computed the accommodative response with Zernike modes. In most cases, we used Equation 4.7 up to the fourth radial order.

MTF-based calculation of the accommodative response

Direct calculations of the refractive errors, such as the paraxial and the rms curvatures, tend to give results that are significantly different (up to 0.5 D) from the subjective methods. This observation can be explained by the compensation of the different

Zernike aberrations, for a normally aberrated eye [64]. It is therefore of interest to develop methods based on retinal image quality to assess refractive errors [57, 62, 201].

These methods can also be applied to compute the accommodative response [110, 138]. The starting point is to define a figure of merit that seems adequate to a visual task, and then to find the amount of Zernike defocus that maximises it. A common metric is the volume under the MTF, for spatial frequencies up to 60 cycles per degree [201]. Higher spatial frequencies are generally considered as not relevant for vision because of the limitations of receptoral and neural factors [202]. We show in Figure 4.7 the time series of the accommodative response of the measurement trial analysed in Figure 4.5 and Figure 4.6. The Zernike defocus is optimised with the MATLAB function "fminbnd", which efficiently finds local extrema within a given interval. For each acquisition time, we use the interval 0 to 0.9 D as initialisation interval. We checked that the optimum defocus is within this interval for $t = 0$ seconds, and that only one global maximum exists. The metric shows a parabolic profile. The resolution of the optimisation is set to 10^{-4} D.

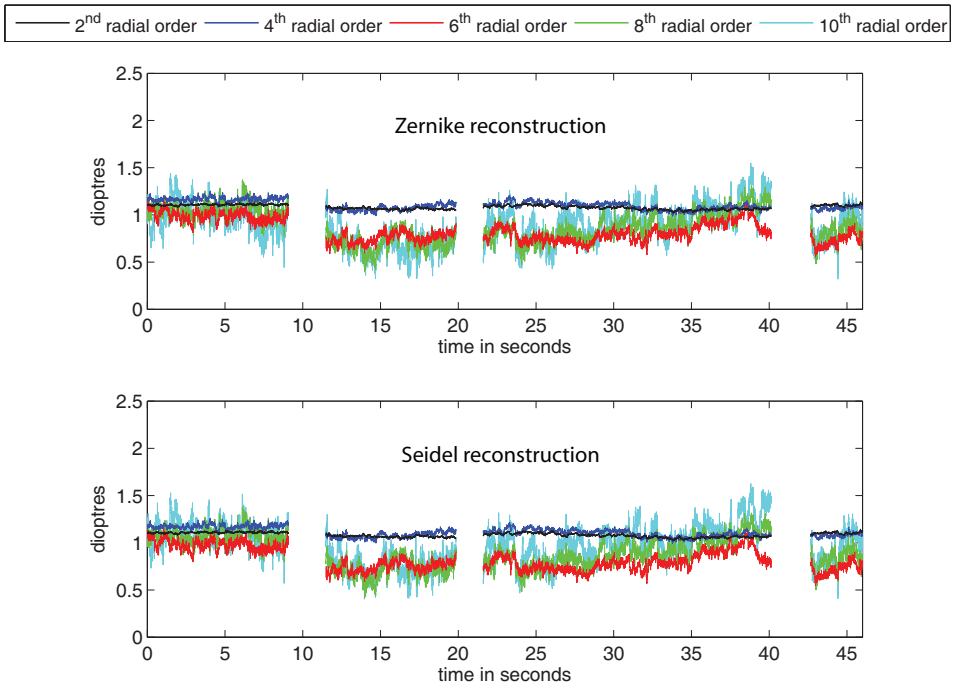

Figure 4.5: Accommodative responses computed with the Zernike (top) and Seidel (bottom) reconstruction, using different radial orders. Each radial order corresponds to the same color on the two graphs. Note the similarity of the time series for the two reconstructions, *at a given radial order*. Data obtained with subject ED (under partial cycloplegia).

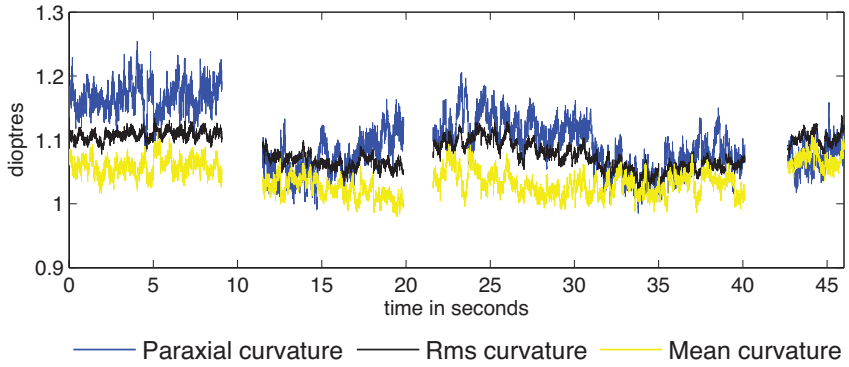

Figure 4.6: Main approaches to compute directly the accommodative response in the pupil plane. These results are computed from the same measurement trial as in Figure 4.5. Blue: "Paraxial curvature" (computed with Equation 4.7 up to the fourth radial order). Black: "Rms curvature", which minimises the rms of the measured wavefront (computed with Equation 4.7 at the second radial order). Yellow: "Mean curvature", computed without wavefront reconstruction (Equation 4.8).

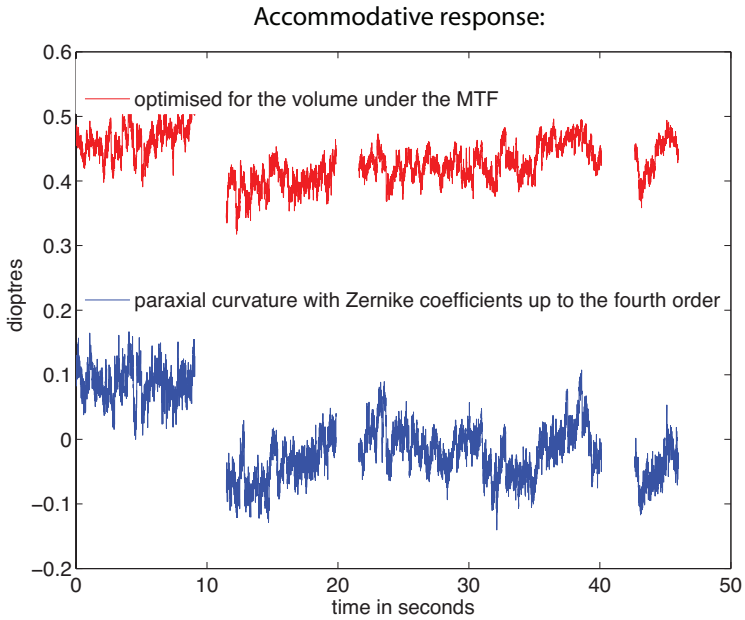

Figure 4.7: Comparison of the accommodative response, computed in the pupil plane (paraxial curvature, blue) and with the optimisation of the volume under the MTF (red). The 0.4 D bias between the two metrics is consistent with other studies of spherical refractive errors [57, 62, 201] . These results are obtained from the same measurement trial as in Figure 4.5 and Figure 4.6.

4.3 Zernike coefficients of misaligned pupils

The simplest way to define the pupil over which we reconstruct the wavefront map is to define this pupil during the calibration of the aberrometer, and to align

the subject as precisely as possible with respect to this pupil. We refer to this pupil as the instrument pupil, which we keep constant (size and position) for the study presented in this section. It is however important to have some idea of the effect of the misalignment of the subject's pupil with respect to the instrument pupil. This effect can be an issue for the reliability of a static study ocular aberrations [203], or for the modeling of the temporal variations of the ocular aberrations. It can be easily investigated using Zernike polynomials. The study we present here uses the work on the transformation of Zernike coefficients published by Lundström et al. [204], who also kindly gave a copy of her code. Using these calculations, we have an algebraic formulation of Zernike aberrations of shifted pupils.

We are grateful to Antoine Leroux, a summer student, for his involvement in the work presented in this section. He had an active role in the rigorous implementation of Linda Lundström's code, in the software of the synchronized eye tracker, and in the data analysis.

4.3.1 Algebraic formulation

We consider shifts $[X_0, Y_0]$ of the pupil of the eye, the origin being the centre of the software pupil of the aberrometer. An ocular wavefront, which is characterized by a set of Zernike coefficients $\mathbf{z}$ over the natural pupil that is centred at $[X_0, Y_0]$, will be measured by the Shack-Hartmann as a set $\widetilde{\mathbf{z}}$ of Zernike coefficients:

$$\widetilde{\mathbf{z}} = \mathbf{M} \times \mathbf{z} \tag{4.9}$$

The simple modeling of eye movement with Equation 4.9 assumes that there is no additional information that is captured by the Shack-Hartmann wavefront sensor, as the eye shift in the measurement plane. This assumption holds if the shift of the pupil is small compared to the instrument pupil, and if the gradient of the wavefront at the edge of the pupil is slowly varying on the scale of the shift of the pupil.

The matrix $\mathbf{M}$ depends on the size of the instrument pupil, and the shift of the pupil $[X_0, Y_0]$. It is always upper-triangular, which means that each coefficient z_p can only influence the measured coefficient $\widetilde{z}_q$ if $q \leq p$. We explain this by the fact that if we write the wavefront as a finite sum of terms $X^p \times Y^q$, the measured wavefront is a sum of terms $(X - X_0)^p \times (Y - Y_0)^q$. Each term can itself be written as a sum of terms of order inferior or equal to p and q. As a result, tip and tilts are the two most sensitive terms to the misalignment of the pupil. Note that we checked our calculations

of **M** with least-squares fits of Zernike coefficients from numerically translated wavefront maps. An example of matrix **M** is shown in Figure 4.8, obtained for a pupil of diameter 5.4 mm, and a vertical shift of $Y_0 = 0.2$ mm. Many off-diagonal terms of the matrix **M** have an absolute values above 0.5. It shows that the Zernike coefficients are extremely sensitive to the alignment of the pupil. For instance, with a 0.2 mm vertical shift, the element (row=7,column=12) of **M** is equal to -0.47. As a result, a pure spherical aberration of 1 μm rms ($z_{4,0} = 1$ μm) is seen by the aberrometer as a combination of spherical aberration $z_{4,0} = 1$ μm and vertical coma $z_{3,-1} = -0.47$ μm. This effect is a well known problem for the optical designer [205]. It represents a technical challenge for the researcher involved in the design of customized contact (or intraocular) lenses [85, 206].

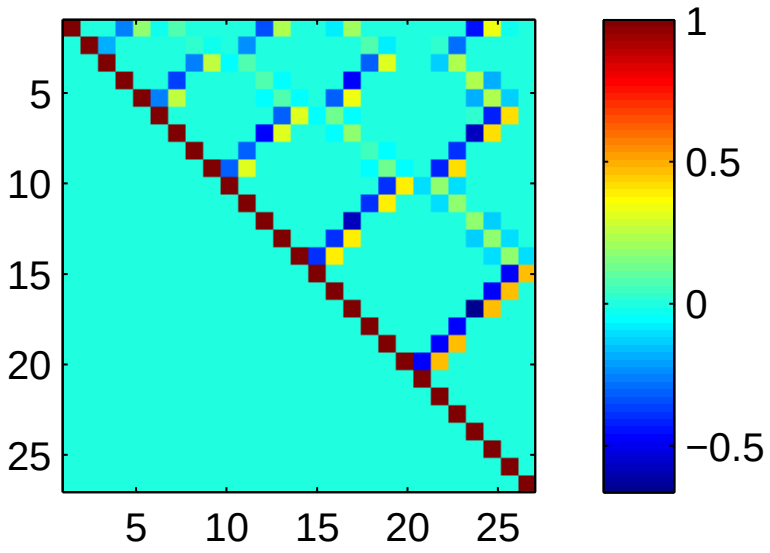

Figure 4.8: **M** matrix, for 27 Zernike coefficients and the 0.2 mm vertical shift of a 5.4 mm pupil. Courtesy of Linda Lundström [204] and Antoine Leroux.

4.3.2 Overall error due to misalignments in a static study of ocular aberrations

We present here a numerical example that illustrates the impact of the subject's misalignments for a static population study. Using the multivariate Gaussian model derived by L. Thibos [57] for a 6 mm pupil, we compute an overall error due to the misalignments of the subjects. We define this error as the norm over 33 Zernike coefficients of the difference between the measured set of Zernike coefficients $\tilde{\mathbf{z}}$ and the

true coefficients $\mathbf{z}$ (up to the seventh radial order, tilts removed):

$$\varepsilon_{\text{ align}} = \sqrt{\langle \langle \|\mathbf{z} - \widetilde{\mathbf{z}}\|^2 \rangle_{X_0,Y_0/\mathbf{z}} \rangle_{\mathbf{z}}} \tag{4.10}$$

The first average $\rangle_{X_0,Y_0/\mathbf{z}}$ denotes the averaging of 10 measurements with a random misalignment $[X_0, Y_0]$ of a given subject, whose true wavefront is described by a fixed set of Zernike coefficients $\mathbf{z}$. We model the alignment errors X_0 and Y_0 with zero mean Gaussian statistics, independently and identically distributed (with a standard deviation δ). This modeling is probably suitable for a study where the subject is realigned after each measurement. The second averaging corresponds to the averaging across the simulated population.

For 100 eyes of the model proposed by Thibos et al., and 10 realignments for each eye, we obtained the values shown in Table 4.3. The errors $\varepsilon_{\text{ align}}$ are all significant in terms of retinal image quality. For the alignment precision $\delta = 0.1$ mm, $\varepsilon_{\text{ align}}$ corresponds to $\lambda/7$ for a 0.5 μm wavelength.

Given the results of Table 4.3, it is thus important to monitor the pupil of the eye with a good resolution when measuring ocular aberrations. The values given in Table 4.3 are comparable to previously published results [203,207]. However, both the study of Bará et al. [203] and Guirao et al. [207] concluded that the benefit of correcting ocular aberrations with phase plates is robust to misalignment, because they analysed the correction of the whole ocular wavefronts (including sphero-cylindrical errors) as a function of misalignment. Unlike these authors, we stress the fact that the correction of the higher order aberrations of a typical eye is very sensitive to misalignment. For a misalignment $\delta = 0.4$ mm the error $\varepsilon_{\text{ align}} = 0.33$ μm is larger than the mean rms value of the higher order aberrations as measured by Thibos et al. (rms $= 0.3$ μm for a 6 mm pupil). For such a large misalignment, there is thus no benefit in correcting (or measuring) higher order aberrations. It is important to bear in mind that these errors are computed without modeling any measurement process, and they are not inherent to the Zernike representation of wavefronts. We obtain the same error $\varepsilon_{\text{ align}}$ if we compute the mean square difference between shifted wavefront maps (without using Zernike coefficients). The real disadvantage of Zernike coefficients is that they are mutually coupled (by the $\mathbf{M}$ matrix), when the pupil of the eye is misaligned. We illustrate this experimentally in the next section.

Standard deviation of misalignment δ in mm	Tip/tilt removed error $\varepsilon_{\text{align}}$ in microns
0.4	0.33
0.2	0.15
0.1	0.07

Table 4.3: Error $\varepsilon_{\text{align}}$ (in microns, see Equation 4.10) due to the misalignment of the pupil, for typical ocular wavefronts as measured by Thibos et al. for a 6 mm pupil.

4.3.3 Drifts of the pupil during a 40 second trial

Our aberrometer reconstructs the wavefront map and the Zernike coefficients $\widehat{\mathbf{z}}$ over a fixed software pupil. The monitoring of the pupil is primarily used for careful alignment of the subject. However, we developed optional software that computes the position of the centre of the pupil from the acquired image of the pupil. (See Figure 2.5, which shows an example of image recorded on a real eye, using some of the laser light primary used for wavefront sensing.) We first test this "eye tracking" configuration with an artificial eye. This artificial eye is a singlet of focal length 18 mm, coupled with a diaphragm (7 mm pupil), and a black screen in the focal plane. We translate horizontally the whole eye with a stage, and measure both the static wavefronts and the displacements of the diaphragm. The first measurement $\widehat{\mathbf{z}_0}$ is done with the pupil centred, and is then used to "predict" the effect of the shift of the pupil on the Zernike measured by the Shack-Hartmann, for any position of the pupil: $\widetilde{\mathbf{z}} = \mathbf{M} \times \widehat{\mathbf{z}_0}$. Figure 4.9 shows the predictions and the measurements of the horizontal coma, for shifts smaller than 0.5 mm. The spherical aberration of the singlet is small (0.03 μm over the 5.4 mm pupil), which explains the very small values of the coma introduced by the shifts of the pupil.

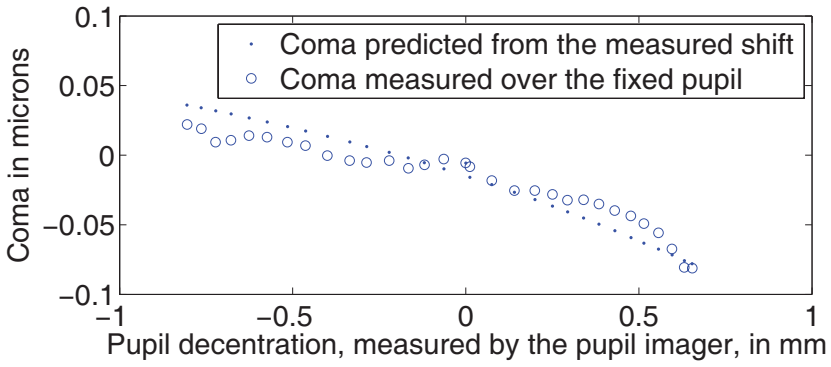

Figure 4.9: Measurements over a 5.4 mm pupil of the coma introduced by the shift of an artificial eye. Courtesy of Antoine Leroux.

Similar predictions were done dynamically, by synchronizing the monitoring of the shifts of the pupil and the acquisition of the data acquired by the SHWFS. The two acquisitions were triggered simultaneously with software, and we obtained a time series of Zernike polynomials (sampled at 100 Hz, over a fixed pupil of diameter 5.4 mm) and a time series of the positions of the pupil (sampled at 7 Hz). The effect of the shift of the pupil was computed for any acquisition time t of the pupil camera: $\widetilde{\mathbf{z}}(t) = \mathbf{M}(t) \times \widehat{\mathbf{z}}(t=0)$. $\mathbf{M}(t)$ is the $\mathbf{M}$ matrix computed using the position $[X_0(t), Y_0(t)]$ of the pupil, and $\widehat{\mathbf{z}}(t=0)$ is the measurement of the Zernike coefficients measured at the start of two synchronized acquisitions. Figure 4.10 shows the time series that we obtained for a relatively unsteady subject. With more experienced subjects, the "bite-bar" usually prevents shifts of the pupil larger than 0.2 mm. However, and even for experienced subjects, we measure the effect of the vertical shift of the eye after a blink, when the eye goes back slowly to its original position. This effect is nicely illustrated by the middle graph of Figure 4.10: at $t = 15$ s, and $t = 27$ s, the negative peak of the measured vertical coma (red) is almost entirely obtained on the predicted data (cyan). This effect should not be interpreted as tear film build-up.

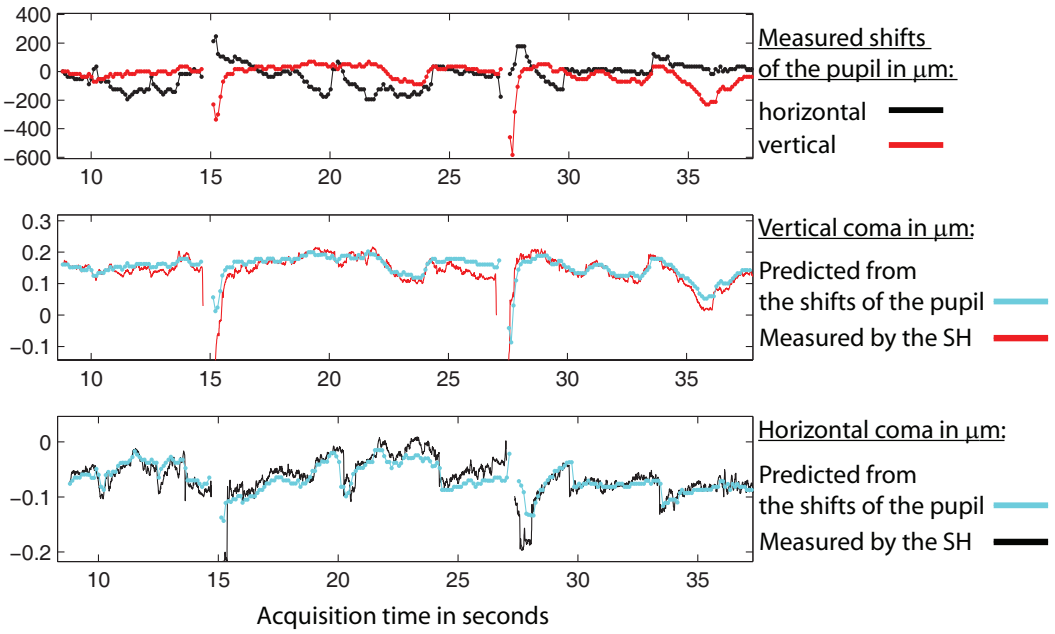

Figure 4.10: Measurements of the effect of the shifts of the pupil on the Zernike comas during a 40 second trial, for an (unexperienced) subject aligned with a "bite-bar". Data recorded and analysed with the assistance of Antoine Leroux.

We do not use the eye tracker for the study of Chapter 5, because it tends to introduce some jitter in the acquisition of the Shack-Hartmann data. (We have used a

single computer for both the SHWFS and the eye tracker, because the cameras were software-triggered.) We only control the position of the pupil with a simple infrared camera and a monitor, to make sure that the pupil of the subjects do not drift by more than 0.5 mm during each 46 second measurement trial. This control is visually done using adequate reference marks that are displayed on the monitor. The centre of the measured pupil is fixed during a single trial, so that eye movements remain an important source of error in our experiment. Our assumption is that the movement of the pupil of the eye is similar for the different accommodative states, and that our comparison of the measured accommodative responses is not affected by this nuisance.

4.4 Software-based extension of the dynamic range of an aberrometer, using Zernike polynomials

Being orthonormal, Zernike polynomials have the advantage to ease the specification of an optical system. We therefore present a method to extend the dynamic range of an aberrometer, which uses their representation in the linear model of the SHWFS. Compared to the methods presented in Chapter 1, our method has the advantage of using mathematical tools that are readily computed for the estimation of the Zernike modes. It can also be optimised for a given application of the SHWFS, if one knows what are the main Zernike aberrations of the measured wavefront.

4.4.1 Presentation of the problem

We assume that the raw frame recorded by the Shack-Hartmann wavefront sensor has been accurately processed by an algorithm that yields a $(2n \times 1)$ set $\mathbf{x}$ of estimated centroid positions that cannot be easily associated with their reference counterpart ($n \leq N$, N being the number of lenslets over the measured pupil). $\mathbf{x}$ contains the positions of the estimated centroids (in pixel units), in a global CCD coordinate system.

The problem we propose to solve is to retrieve the lenslet associated to each centroid position. The output of the algorithm is thus a set of centroid displacements $\delta\mathbf{X} = \mathbf{X} - \mathbf{X}_{ref}$, of size $2N \times 1$ (with at most $2n$ valid components). $\mathbf{X}_{ref}$ is the set of centroid positions measured with a reference wavefront, and $\mathbf{X}$ the set of sorted centroid positions. Before invoking the algorithm, each component of $\mathbf{X}_{ref}$ is associated with a position in the pupil plane.

4.4.2 Principle of the algorithm

Assuming that a certain number of spots remain in the field of view of their lenslet (typically a 3×3 grid), a vector of centroid displacements $\delta\mathbf{X}_0$ (of size 18×1) is defined to initialize our algorithm. A first reduced set of Zernike coefficients $\mathbf{z}_0$ (with typically five terms: tilts, defocus, and astigmatism) is then computed from $\delta\mathbf{X}_0$ using the least square method, which is classically described as a modal reconstruction of the wavefront [146, 147, 164]. The five components of $\mathbf{z}_0$ can only be considered as a rough approximation to their true values $\mathbf{z}$, because they were estimated using 9 centroid displacements only. In the case where these modes (tilts, defocus, and astigmatism) are actually the only significant modes of the true wavefront, $\mathbf{z}_0$ will only differ slightly from $\mathbf{z}$ because of the measurement noise on the centroid positions $\delta\mathbf{X}_0$. From the approximated set of Zernike coefficients $\mathbf{z}_0$, it is straight-forward to compute an approximation $\widetilde{\mathbf{X}}$ of all the centroid positions $\mathbf{X}$ of the sensor, using the geometry matrix $\mathbf{A}$ presented in section 4.1.2:

$$\widetilde{\mathbf{X}} = \mathbf{X}_{ref} + \mathbf{A} \times \mathbf{z}_0$$

We recall that each component of $\mathbf{A}$ is the shift of a given Shack-Hartmann spot (row index) induced by a given Zernike aberration (column index).

For each lenslet i, we then search among the components of $\mathbf{x}$ for the computed centroid position that is the nearest to $\widetilde{\mathbf{X}}[i]$. This allows us to form the set of centroid positions $\mathbf{X}$ (of size $2N \times 1$, but with invalid data that mark the missing centroid positions) that corresponds to the Shack-Hartmann spots that have been associated to their reference counterpart. A simple way to identify a Shack-Hartmann spot is to use a threshold value d (in pixels) for the maximum distance allowed between the approximated centroid position $\widetilde{\mathbf{X}}[i]$ and the nearest component of measured centroid positions $\mathbf{x}$.

4.4.3 Implementation

We briefly describe some details of the algorithm we implemented with a 6 mm configuration of our custom built aberrometer described in Chapter 2 (23 lenslets across). The dynamic range of this aberrometer in terms of curvature of the wavefront (crossover of adjacent spots) is relatively large. For a 10 dioptres myopic eye, adjacent spots are still separated by 16 pixels (instead of the 18.5 pixels pitch), but

some of the spots are shifted by more (24 pixels) than the dimension of a lenslet. Without any dedicated algorithm, the maximum power that can be measured with this aberrometer over a 6 mm pupil is approximatively 2 dioptres. The aberrometer uses a very narrow probing beam, which is not corrected for the refractive error of the subject and parallel to the axis of the instrument.

Due to reciprocity of propagation of light, the local tilt of the measured wavefront is zero at the position where the probing beam enters the eye, when the probing beam is parallel to the optical axis of the wavefront sensor. We thus initialize the algorithm with a 3×3 grid of lenslet centred on the probing beam. For each lenslet i of this 3×3 grid, our algorithm attributes to $\mathbf{X}_0[i]$ the component of $\mathbf{x}$ that is closer to $\mathbf{X}_{ref}[i]$ than a distance equal to half the pitch of a lenslet.

Once the initialization is done, we compute the approximated set of Zernike coefficients $\mathbf{z}_0$, and then a first set of approximated centroid positions $\widetilde{\mathbf{X}}$. To improve robustness, the vector $\delta\mathbf{X}$ is not reconstructed at once. In many cases, the vector $\widetilde{\mathbf{X}}$ is a good approximation of $\mathbf{X}$, and all centroid positions can be retrieved at once. It is however safer to do the extrapolation in several steps, especially if there is a significant amount of coma in the measured wavefront.

Figure 4.11 shows how we typically extrapolate over the whole pupil: each number corresponds to the number of steps used before attributing a centroid position to a given lenslet. From the first calculation of $\widetilde{\mathbf{X}}$, only 16 centroid positions (marked by a "1" in Figure 4.11) are identified and concatenated to $\mathbf{X}_0$ to form a vector $\mathbf{X}_1$ (of size 50×1). A set of 14 Zernike coefficients $\mathbf{z}_1$ is estimated from the available centroid displacement $\delta\mathbf{X}_1$, and the process is repeated 19 times until the whole pupil has been analyzed. The number of Zernike terms we use for this algorithm is 14 for any further iteration, because we assume that a priori only these modes will be significantly large. Using a normal computer with a 2 GHz processor and a MATLAB implementation of the algorithm, the full process takes approximatively 0.4 seconds and is thus only useable offline. For a real time computation of ocular aberration, it is not necessary to invoke the algorithm at each frame. Each centroid position can be tracked from the previous frame.

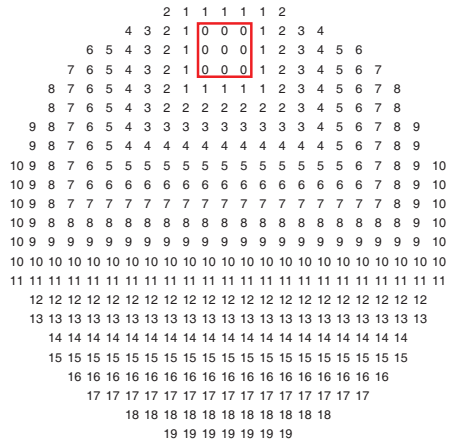

Figure 4.11: Steps for the extrapolation of the centroid positions across the measured pupil.

4.4.4 Results

Figure 4.12(a) shows the spot displacements reconstructed from the double-pass measurement of an ophthalmic cylindrical lens. The lens was placed in the measurement plane of our aberrometer, just in front of an artificial eye (a 40 mm doublet that has an opaque screen in its focal plane). The position of the probing beam in the measurement plane is marked by a black circle. The measured astigmatism is ($z_{2,-2} = -5.1$ μm, $z_{2,2} = 0.5$ μm), using the convention adopted by the OSA [156]. Figure 4.12(b) shows the spot displacements reconstructed from a simulation of the centroid positions obtained with a similar astigmatic wavefront $z_{2,-2} = -5.5$ μm. The position of the centroid positions of the spots are computed using the geometry matrix of the Shack-Hartmann, and permuted before invoking our algorithm, in order to simulate the detection of the centroid positions with software windows that are not bound to the lenslet array. The global tilt of the measured wavefront is adjusted so that the spot displacement of the lenslet centred on the probing beam is zero, in order to satisfy the principle of reciprocity of the propagation of light. For this simulation and the one shown in Figure 4.13, we consider our algorithm as successful if all centroid positions are correctly paired to their reference counterpart.

The dynamic range of our algorithm, which is suitable for double-pass measurements, is primarily limited by the successful initialisation of the 3×3 grid. If the wavefront is locally too aberrated, the assumption that the spots of this grid remain in the field of view of their lenslet might not hold. (But the spot in the middle of this grid

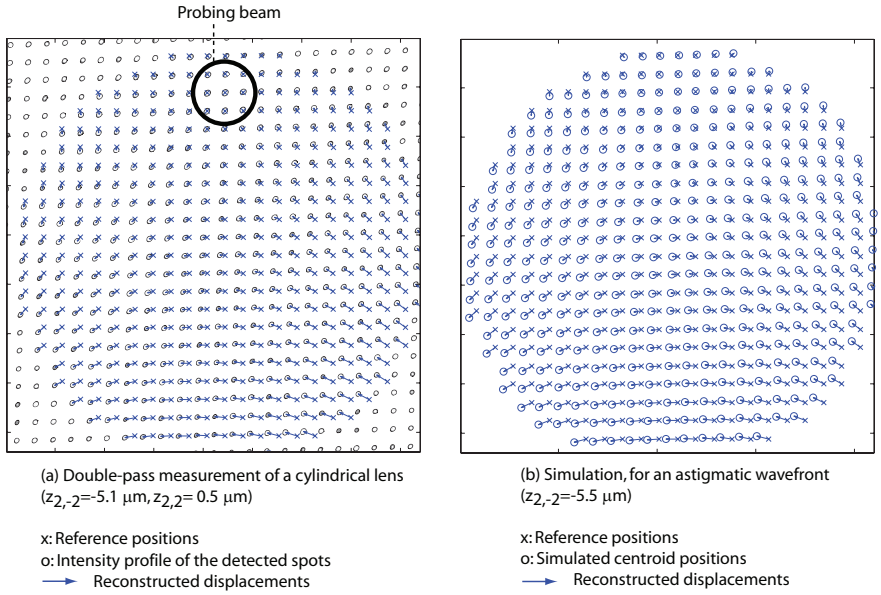

Figure 4.12: Successful pairing of the Shack-Hartmann spots (o) with their reference counterparts (x), for an astigmatic wavefront and a probing beam located 2.25 mm superior to the pupil centre. Left: double-pass measurement with an ophthalmic lens. Right: simulation.

will remain unshifted, if the probing beam is correctly centred on the grid.) We show in Figure 4.13 the extension of the dynamic range for combinations of astigmatism $z_{2,-2}$ (vertical axis of each graph) and higher order aberrations (horizontal axis): trefoil $z_{3,-3}$ (a), coma $z_{3,-1}$ (b), secondary astigmatism $z_{4,-2}$ (c), and spherical aberration $z_{4,0}$ (d). The black region corresponds to the combinations of aberrations for which each spot remains in the field of view of its lenslet. The gray region corresponds to the region for which all the spots are correctly assigned to their reference counterpart with our algorithm. It is important to mention that these simulations are obtained without performing the full detection of the CCD frame with floating software windows, and that the magnitude of aberration in Figure 4.13 is much larger than that obtained in real eyes. The centroid positions are computed, as in Figure 4.12(b), with the geometry matrix of the sensor. According to the simulations shown in Figure 4.13, the dynamic range of our aberrometer is primarily limited by the crossover of adjacent spots, which is not taken into account in our simulations. For example, with a spherical aberration $z_{4,0} = 4$ μm (and no astigmatism), some adjacent spots are separated by 6 pixels only. Assuming that their centroid positions are processed accurately, our algorithm retrieves their reference positions.

These results show that our algorithm is suitable for the measurements of patients with keratoconus, who have on average around 2.5 μm of root mean square higher order aberrations over a 6 mm pupil [153, 155]. A MATLAB code and demonstration of the algorithm is available on our website (http://optics.nuigalway.ie/people/charlie). This algorithm has been successfully implemented for the experimental study of the microfluctuations of accommodation of young subjects over a 3.9 mm pupil at a 173 Hz frame rate, which is presented in Chapter 5.

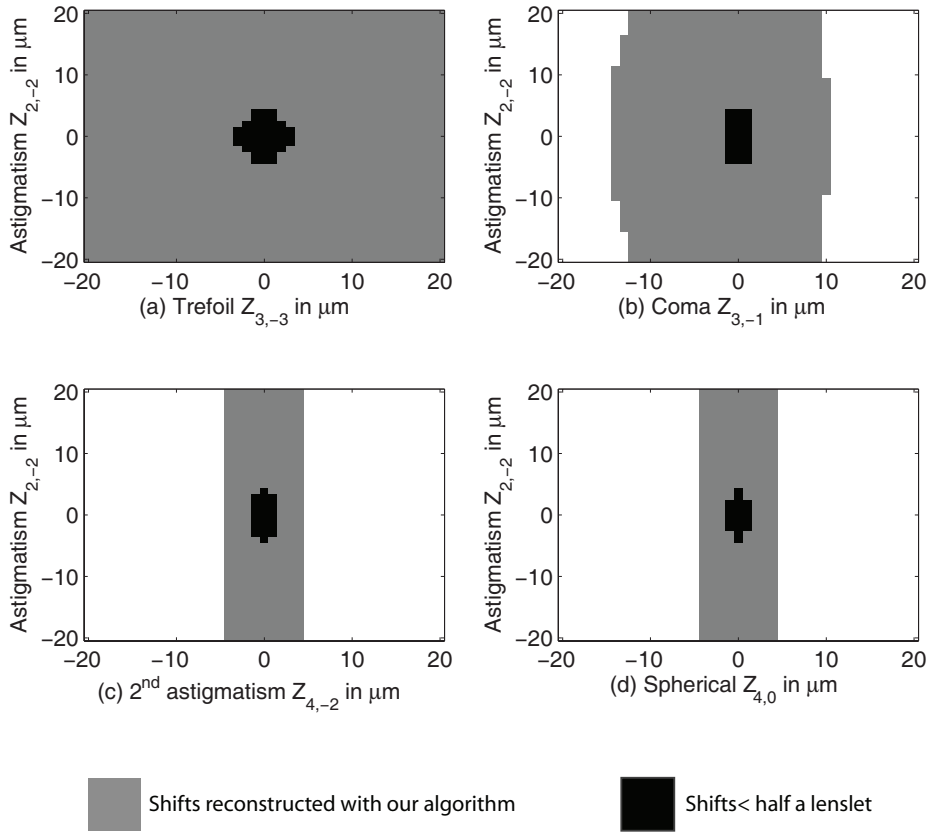

Figure 4.13: Dynamic range of our custom built aberrometer for a 6 mm pupil, with and without our algorithm, for combinations of astigmatism $z_{2,-2}$ (vertical axis) and various higher order aberrations (horizontal axis).

Chapter 5

Dynamics of accommodation and mean effort

We present in this chapter the study of the dynamics of accommodation, which was carried out with Conor Leahy and Dr. Luis Diaz-Santana of City University, London. Keeping in mind the non-stationarity of the accommodative responses, we performed a simple signal analysis that is potentially relevant for further clinical studies.

As we mentioned in Chapter 1, the relationship of the microfluctuations to the mean response of the accommodative system is of primary interest, because the physical nature of the process changes depending on the level of accommodative effort. Previous studies have reported that the amplitude of the high frequency component increases with the target vergence [35, 110, 121, 128].

The major novelty of our approach is to compute a linear fit of the periodograms represented on a log-log scale. This $1/f^{\alpha}$ ("power law") modeling of the signal is a common approach for biological signals [208]. Looking at the periodogram on a log-log plot emphasises the global shape of the PSD, rather than finer details like peaks associated with the heartbeat and breathing. Such peaks are known to vary in frequency over short periods of time and can be better observed using time-frequency analysis [142].

We also investigated the increments of the accommodative response, because it

was in many cases more stationary than the response itself. In particular, we analysed its autocorrelation, which is common practice to detect patterns in biomedical processes. Autocorrelation functions can give an indication of whether there is any neurological processing involved in the regulation of these processes [208]. Long-term correlation and fractal behaviour has been found in the human heartbeat [209, 210], which is known to be closely related to the microfluctuations of accommodation [118]. This implies that the current value of the biological signal depends not only on its most recent value but also with its long-term history.

We used our custom-built aberrometer as an alternative to the classically-used infrared optometer, which was first implemented by Campbell in 1959 [211]. Infrared optometers can typically measure the accommodative response up to 100 Hz, because the detector is a simple photodiode. Most Shack-Hartmann based aberrometers work at a frame rate of 25 Hz and are thus of limited interest for this task. For the study presented in this chapter, we have configured our aberrometer for measurements of ocular wavefronts over a 3.9 mm pupil, at a 173 Hz frame rate.

5.1 Data collection

5.1.1 Fixation arm

A fixation arm was built and attached to the aberrometer, as it is shown in Figure 5.1.1. Data was collected from the subject's dominant eye. (The non-dominant eye of the subject was covered with an eye patch.) To ensure identical fixation conditions for all subjects, the effective pupil of the dominant eye was conjugated with plane Π on the fixation arm where it was limited to 4 mm by a diaphragm.

A Snellen "O" was used as fixation target, and was seen under the same angular size (6/12) and the retinal illuminance (80 cd/m^2), independent of its vergence. The Maltese cross is widely used in experimental studies of accommodation, because it contains a large range of spatial frequencies [212]. On the other hand, the Maltese cross makes the subject change his focus as he switches from the horizontal to the vertical lines of fixation, when astigmatism is not perfectly corrected [131]. With its circular symmetry, the retinal image of a Snellen "O" is equally degraded by all directions of astigmatism. In fact, astigmatism can even help the subject to keep this target in focus, as we suggest in Chapter 6 (see Figure 6.3). The target was illuminated by an unfiltered green LED ($\lambda = 0.53$ μm). We might have improved the focus

fixation of some subjects using white light, as is suggested in references [139–141]. The probing beam of the aberrometer was set at a power approximatively equal to 15 μW ($\lambda = 0.78$ μm), and was scanned over a 1° field angle to remove speckle on the raw frames recorded by the Shack-Hartmann. It was centered slightly off axis, so that it was seen by the subject just outside of the green circular background field of diameter 1°.

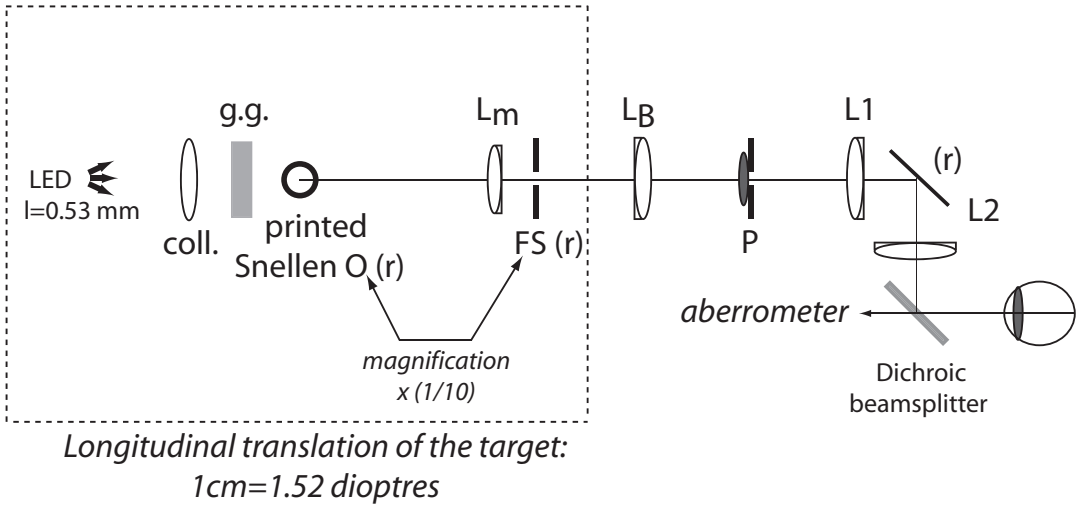

Lm	magnification lens (f=40 mm)	(r)	retina conjugates
LB	Badal lens (f=80 mm)	⬭	pupil conjugates
coll.	collimator (f=50 mm)	FS	1degree field stop
g.g.	ground glass	P	4 mm pupil stop,
L1/L2	telecentric relay (f=120 mm)		cylindrical correction,
			- 4 dioptres lens

Figure 5.1: Fixation arm used for the experiment.

5.1.2 Protocol

The wavefront aberration from 9 eyes was measured for 3 different accommodative states: near viewing, far viewing, and an intermediate position. 4 trials of 46 seconds length were performed for each state. A further 4 trials were performed under partial cycloplegia, using ophthalmic drops (1% Tropicamide). The far position was first found by the subject who translated manually the target away from the Badal lens L_B of the fixation arm (as seen in Figure 5.3).

The instruction was to find a comfortable far viewing position. A cylindrical ophthalmic lens could be introduced in the fixation arm at plane Π to correct for the subject's astigmatism. We then introduced a -4 D ophthalmic lens in the plane Π. This defined the intermediate point for the trials, which corresponded to the same accommodative demand for all subjects (4 D from the subject's far point). The near viewing position was then found by directing the subject to translate the target towards L_B. We encouraged the subject to find the limit of his/her accommodative range. The near viewing position was then found by directing the subject to translate the target approximately 1 cm towards L_B, which typically corresponds to an additional 1.5 D demand. Preliminary measurements were taken to make sure that the accommodative response at the near point of viewing was at least 1 D larger than for the intermediate point. We monitored the pupil constriction during measurements to ensure that this requirement was maintained. If the subject reported a sudden drop in the retinal image quality, the trial was discarded. The subject was aligned using a bite-bar for stabilisation.

This research was approved by The National University of Ireland Research Ethics Committee. Informed consent was obtained from all participants.

5.1.3 Measurements of the accommodative response

The aberrometer was calibrated using a point source located at a distance of 938 ± 1 mm away from the measurement plane (see section 2.1.2). The power of the measured wavefronts was reliably measured after removing the divergence of the reference, to an accuracy of 0.001 D. Because of the chromatic effect of the optics of the eye, the measured accommodative response values were biased by approximately -0.5 D compared to the 0.53 μm central wavelength of our stimulus [57, 163]. This bias was not removed in our measurements. The aberrometer uses a narrow probing beam (0.5 mm FWHM, in the measurement plane), and the signal to noise ratio of the aberrometer is thus robust to ocular aberrations. We thus measure ocular wavefronts at different accommodative levels without any optical compensation of the defocus of the measured beam, and with the same power of the probing beam. CMOS frames are shown in Figure 5.2, for subject AOB at his far and near points. It was found that the CMOS frames were usually brighter at the near point, which is not intuitive because of the expected blur of the spots. With an artificial eye (a 18 mm doublet with a dark screen located near the focal plane), we found that the peak of the spot of the SHWFS was on average reduced by a factor 0.7 when translating the screen from the 0 to 6 D

of myopia. The increase of the signal at the near point, which we observed for most human eyes, is therefore probably due to the structure of the retina. It is possible that the coupling of the light with the photoreceptors is better when the eye is accommodating (or myopic). This point might require further experimental investigations.

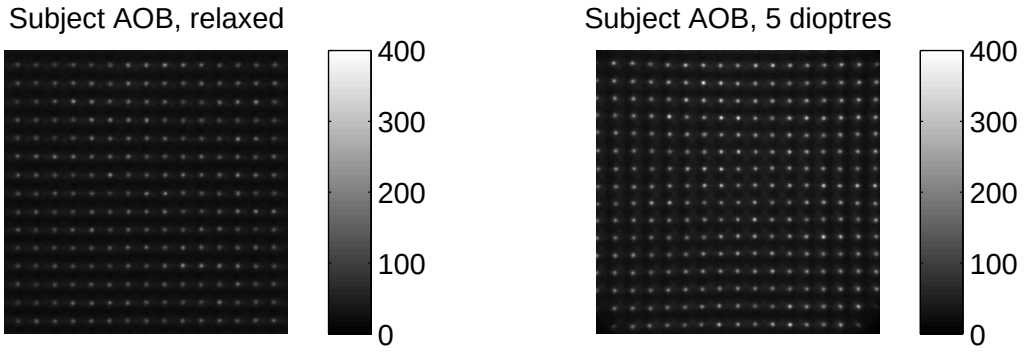

Figure 5.2: Example of recorded CMOS frames, for subject AOB over the 3.9 mm pupil. Left: relaxed accommodation. Right: near accommodation. Exposure time and light level were kept constant for this study, and we did not correct the defocus of the measured ocular wavefronts.

We used the algorithm presented in section 4.4 to extend the dynamic range of the aberrometer. As a consequence of the double-pass measurement process, the lenslet which is centred on the probing beam images a Shack-Hartmann spot that remains unshifted for any measured ocular wavefront. This effect is used by our algorithm to initialise an iterative process, which aims to couple the measured centroid positions to their reference counterpart. If the probing beam remains unchanged (angle and position in the pupil plane), the tilts and the defocus of the measured ocular wavefronts are linearly related. To first order, this linear relationship only depends on the position of the probing in the pupil plane.

Figure 5.3 shows the measured Zernike coefficients (in microns, for a 5.4 mm pupil) function of the measured power of the beam. The blue graphs correspond to Subject CL, and the black graphs were obtained by translation of an opaque screen between the lenses of the aberrometer $L1$ and $L2$. (See Figure 2.1.) From those data, one can compute the aberrations introduced by the aberrometer alone (minus the first lens $L1$) over the represented range of $[0 - 7]$ D. They are below 0.04 μm rms (including astigmatism), and can be removed by use of a lookup table. These results shows that the static measurement of the ocular aberrations of the accommodated eye is a potential application of our instrument.

We used a software pupil to estimate ocular wavefronts over a fixed $\Phi = 3.9$ mm pupil. From the modal reconstruction of the Zernike coefficients of the wavefront (up to the fourth radial order), we computed the accommodative response for the discrete acquisition time n, $a(n)$ (D) [57]:

$$a(n) = \frac{16\sqrt{3}}{\Phi^2}\left(z_{2,0}(n) - \sqrt{15} \times z_{4,0}(n)\right) \tag{5.1}$$

We define the mean effort for the conditions with unparalysed accommodation as the mean response minus the mean response obtained with partial cycloplegia. Figure 5.4 compares the mean accommodative effort of the 9 subjects at the 3 unparalysed conditions. The effort performed by all subjects at the far point was on average 0.6 D (magenta bars), and corresponds to the accommodation lead usually observed for a relaxed accommodative state. At intermediate viewing, the mean effort is 4.1 D (green). The effort at near viewing corresponds to the maximum accommodative effort that the subject is able to maintain consistently, and is on average 5.9 D (red).

5.2 Time series analysis

To prepare the data for analysis, each trial (consisting of 8,000 data points) was first examined for the presence of spurious values caused by the subject blinking. These unwanted values include instances where the eye is in the process of opening or closing, and also the transient after a blink before the process returns to steady-state [35, 142]. Data points corresponding to times when the subject was blinking can often be detected by examining the time series. Automatic methods for the removal of these unwanted values based on the time series values have been proposed in previous work [142], however it was felt that to maximise the efficiency of data removal, the individual Shack-Hartmann frames should be checked manually before removing data points. This procedure was carried out manually for each trial that was used in this study. The blanks in the time series are blinks, and typically correspond to 1 second. Our approach consisted in systematically removing any part of the response that was related to a blink: tear film break-up and build-up, eye movement, and increased noise in the reconstruction of the Zernike modes of the wavefront due to a vignetted pupil.

A simple approach to quantifying the microfluctuations of accommodation for each measurement trial is to compute the rms fluctuations of the accommodation response [120–122, 128]. This approach does not show much difference between the

intermediate and the near point, as we found mean rms values of 0.18 D (near), 0.22 D (intermediate), 0.16 D (far), and 0.11 D (partial cycloplegia). The rms is very sensitive to drifts of the response, and is consequently not adequate to quantify non-stationary signals, such as those observed at conditions other than the intermediate point. We therefore pursued other methods to quantify our observations, through spectral analysis and assessing the autocorrelation function of the time series increments.

5.2.1 Spectral analysis

The Lomb-Scargle periodogram [213,214] is a least-squares spectral analysis approach which employs a modification in the classical definition of the periodogram in order to render it capable of dealing with unevenly sampled and/or incomplete data. Its statistical properties are well defined and it allows good flexibility in frequency resolution. The Lomb-Scargle periodogram was the method used to estimate the power spectral density (PSD) throughout this study. The spectrum was implemented as follows [214]:

$$P_a(\omega) = \frac{1}{2}\left\{ \frac{\left[\sum_j a_j cos\omega\left(t_j-\tau\right)\right]^2}{\sum_j a_j cos^2\omega\left(t_j-\tau\right)} + \frac{\left[\sum_j a_j sin\omega\left(t_j-\tau\right)\right]^2}{\sum_j a_j sin^2\omega\left(t_j-\tau\right)} \right\} \tag{5.2}$$

where ω is the angular frequency, x_j is the value of the j-th data point, and τ is defined by

$$tan\left(2\omega\tau\right) = \frac{\sum_j sin2\omega t_j}{\sum_j cos2\omega t_j} \tag{5.3}$$

Periodograms were obtained for each trial. The periodograms were estimated from trials with 73 % valid data on average. The spectra are evaluated at 3,000 uniformly spaced frequencies (green trace) and 1,650 frequencies (blue trace) in the range 0.01-86.5 Hz. In least-squares spectral analysis, the number of invalid points in the time series does not impact on the resolution, because the spectrum is evaluated at arbitrary frequencies [214]. The periodograms were transformed to a logarithmic scale in both axes. Figure 5.5 shows periodograms for 3 subjects on a log-log scale, for frequencies up to 10 Hz. Using this representation it was possible to fit a piecewise straight line slope model. A straight line slope in a log-log representation implies a power law relationship, in this case between spectral power and frequency. Two separate lines are fitted in each case, comprising a lower frequency region slope m_1 and a higher frequency region slope m_2, with the breaking point between them deter-

mined empirically by visual inspection of the data. Fitting slopes to the periodograms was achieved using a robust linear regression method. Table 1 shows the fitted slope values for all nine subjects at each of the viewing conditions, along with the average value across subjects. At the intermediate point, we computed a systematically more negative slope of the periodogram in the higher frequency slope range, with an average value of $m_2 = -3.2$. At the far point (and with partial cycloplegia), the periodogram could be better fitted by a single straight line over the whole 0.2-10 Hz range. We found average slope values of $m_1 = -1.2$ and $m_2 = -2.1$ for the far point, and $m_1 = 1.1$ and $m_2 = -2.0$ for the partial cycloplegia condition.

Figure 5.6 shows the periodogram averaged across 8 subjects, with the 4 viewing conditions overlaid on a single plot. The difference in the shape of the periodogram for the intermediate viewing is still clear after averaging across subjects. Figure 5.6 also shows that the estimated PSD at the near point is to some degree a mixture of the estimated PSD obtained for the far point and the intermediate point, with an average slope of $m_2 = -2.1$ in the 2-10 Hz range.

Subject	m_1 (near)	m_2 (near)	m_1 (int)	m_2 (int)	m_1 (far)	m_2 (far)	m_1 (cyc)	m_2 (cyc)
CML	-1.0	-2.2	-0.4	-3.4	-1.2	-1.7	-1.7	-1.5
CEL	-1.4	-2.3	-0.7	-3.6	-0.8	-2.2	-1.4	-1.8
ED	-0.8	-2.5	-0.4	-3.8	-0.7	-1.5	-1.1	-1.5
DDB	-0.2	-1.8	-1.5	-1.9	-1.4	-2.5	-1.3	-1.5
EDL	-0.7	-1.5	-0.1	-2.9	-1.2	-2.1	-1.0	-1.7
MS	-1.3	-2.2	-1.1	-3.4	-1.0	-2.2	-0.8	-1.9
MN	-0.9	-2.2	-1.6	-2.9	-1.6	-2.4	-1.1	-2.6
AOB	-1.8	-2.7	-0.8	-4.0	-1.3	-2.7	-0.8	-3.1
EL	-1.3	-1.6	-1.2	-3.2	-1.2	-1.6	-0.8	-2.0
Average	-1.0	-2.1	-0.9	-3.2	-1.2	-2.1	-1.1	-2.0

Table 5.1: Fitted slopes for the 9 subjects. Data analysis by Conor Leahy.

When a subject is fixating at the near limit of his acommodative range, the fluctuations of accommodation are greatly reduced. A small relaxation of the accommodative effort creates large microfluctuations. This effect is illustrated by Figure 5.7. For $t > 25$ s, the near-limit of fixation response resembles what we typically observe at intermediate viewing. For $t < 12$, the amplitude of the microfluctuations is reduced in a manner similar to what we typically observe at the far point. Changes of behaviour like this within a single trial at the near point were quite commonly observed. It is

very likely that fatigue prevented the subject to focus at his/her near limit of fixation for more than 20 seconds. We suggest that measuring accommodation in subjects at the near limit of their accommodative range might be better served by open view conditions.

5.2.2 Autocorrelation of increments

Many types of commonly observed non-stationary processes are known to have stationary increments. The increments of a time series can provide information about the underlying process, and are useful in the removal of some nonstationary trends [215]. The increments (or first difference) $x(n)$ of the discrete accommodation response $a(n)$ are given by $x(n) = a(n) - a(n-1)$. We therefore analysed the autocorrelation function (ACF) of the increments of the accommodative response. The ACF r_{xx} of the discrete random process $x(n)$ as a function of sample lag k can be estimated as follows [216]:

$$\hat{r}_{xx}(k) = \begin{cases} \sum_{n=0}^{N-k-1} x_{n+k} x_n^* & \text{if } k \geq 0 \\ \\ \hat{r}_{xx}^*(-k) & \text{otherwise} \end{cases} \tag{5.4}$$

where N is the sample size. The ACF of a signal may be used as a quantitative measurement of the memory in the system from which the signal arose [208]. In this study, we computed estimates of the ACF over blocks of $N = 500$ samples. This enabled us to obtain multiple estimates from a single trial. Any blocks containing data previously marked as invalid were discarded. These estimates were then averaged to give a single ACF estimate for each subject at each viewing condition. The estimates rely on the assumption that the process is wide-sense stationary.

Figure 5.8 shows the normalised ACF of increments of Zernike defocus $z_{2,0}$ for 3 subjects, at each of the 4 viewing conditions. Each plot is averaged over 4 separate trials. The slower decay in the ACF suggests longer lasting correlation of the increments of the process for intermediate viewing. This suggests there is some memory in the process in the case of intermediate viewing [208], whereas for the other conditions the ACF more closely resembles physiological noise. It is possible that the memory in the system could play some role in stabilising the accommodative response when the subject is viewing targets at their intermediate point.

It is apparent from Figure 5.9 that the noise on the measured accommodative response has an important impact on the ACF. The ACF of the increments of the Zernike

defocus $z_{2,0}$ shows a smoother and a longer lasting profile than the full accommodative response, because the noise on the measured spherical aberration (Zernike $z_{4,0}$) is increased by a factor of $\sqrt{15}$ in Equation 5.1.

The results of our study show that the shape of the estimated PSD for a 4 D effort is distinct from the shape for the two extrema of the accommodation range. We observe different slopes in the periodogram depending on the mean accommodative response, in a manner that is consistent from subject to subject. Therefore the scaling of the microfluctuations is related to the accommodative state of the eye, and is significantly altered when the accommodative system is in its active range i.e. between the near and far point.

Further investigation of the dynamics of accommodation at different levels of accommodation (every 1 D for example) would clarify the relevance of the mathematical tools that we introduced in this study. In particular, it would be interesting to quantify the slopes of the PSD in the 2-10 Hz, over the whole accommodation range. This would hopefully provide a concise statistical description of the microfluctuations of accommodation.

We also report for the first time the long-lasting correlation of the increments of the accommodative response, for the 4 D effort. ACF of the increments of the accommodative response is potentially an interesting tool to analyse the microfluctuations of accommodation.

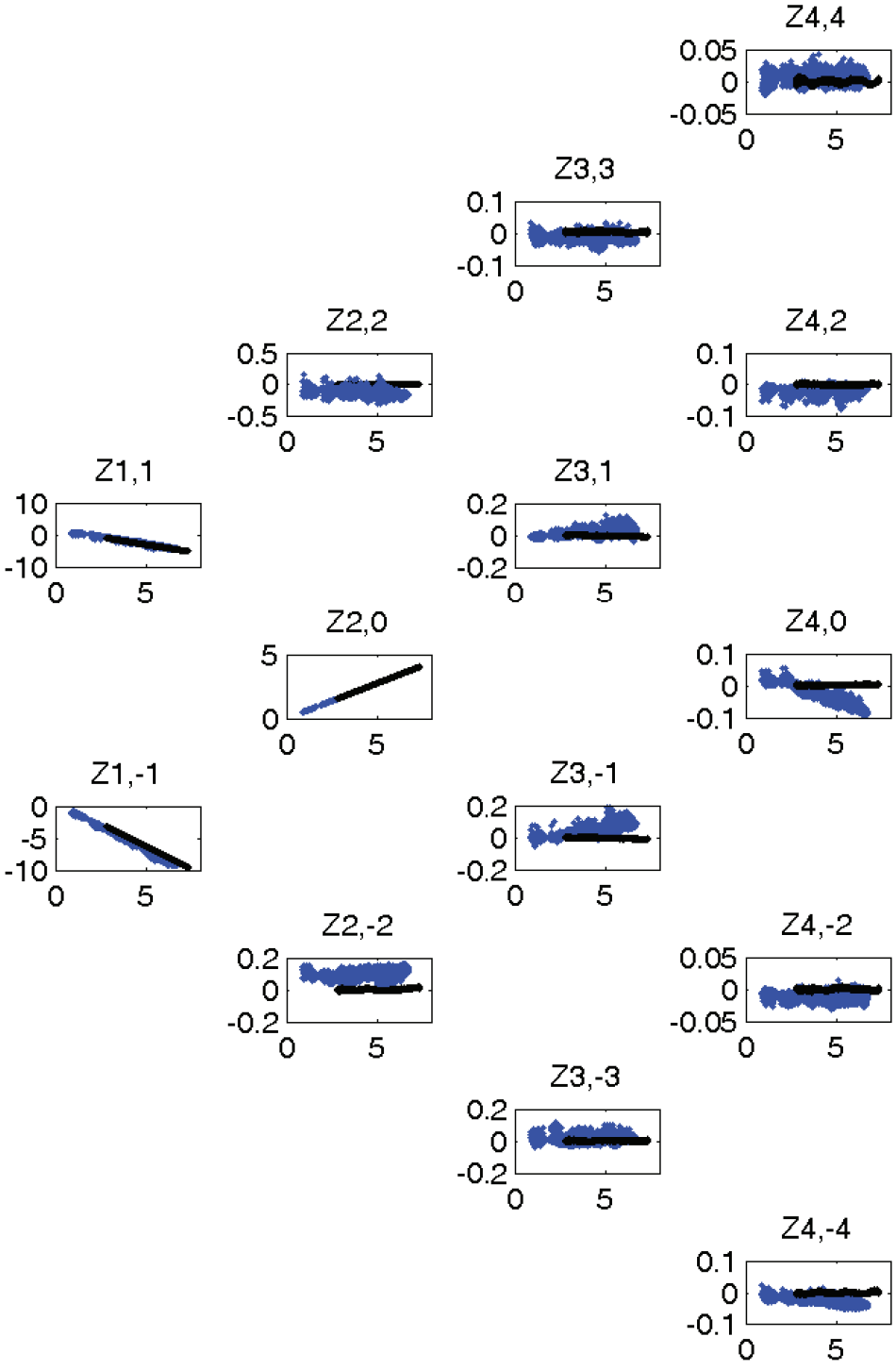

Figure 5.3: Aberrations of Subject CL (blue), as Zernike coefficient $z_{n,m}$ in microns over a 5.4 mm pupil (y axis), function of the accommodative response in dioptres (x axis). Black: aberrations of the system, measured with an articial eye.

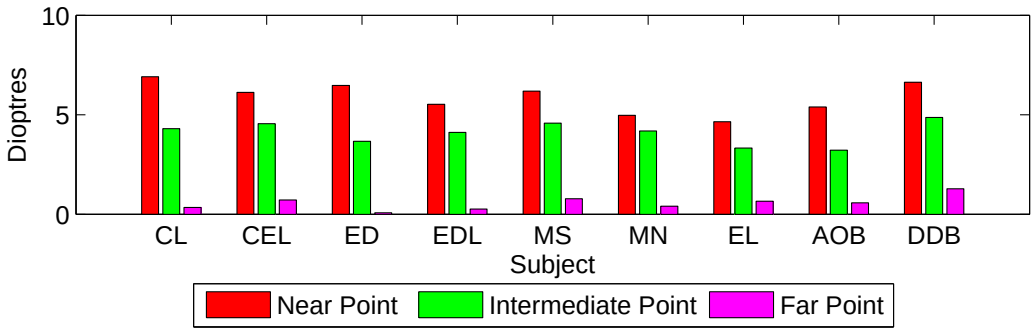

Figure 5.4: Comparison of the mean accommodative effort of the 9 subjects at the 3 natural viewing conditions.

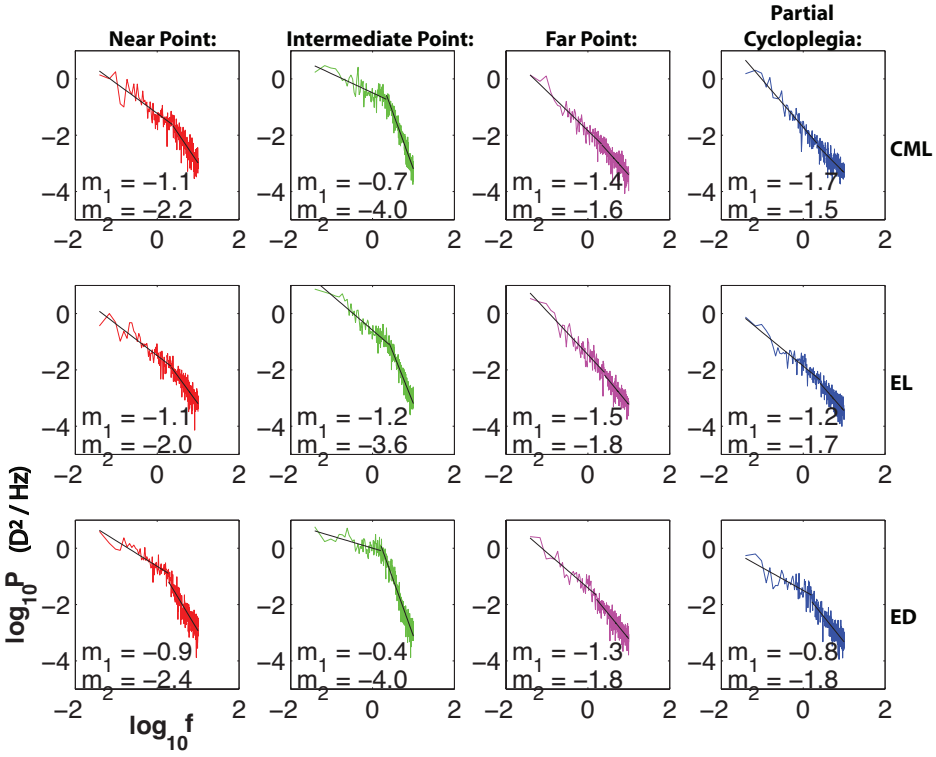

Figure 5.5: Periodograms of the accommodative response for 3 subjects at each of the viewing conditions with fitted slopes. The values m_1 and m_2 denote the fitted slopes for the lower and higher frequency regions respectively. Data analysis by Conor Leahy.

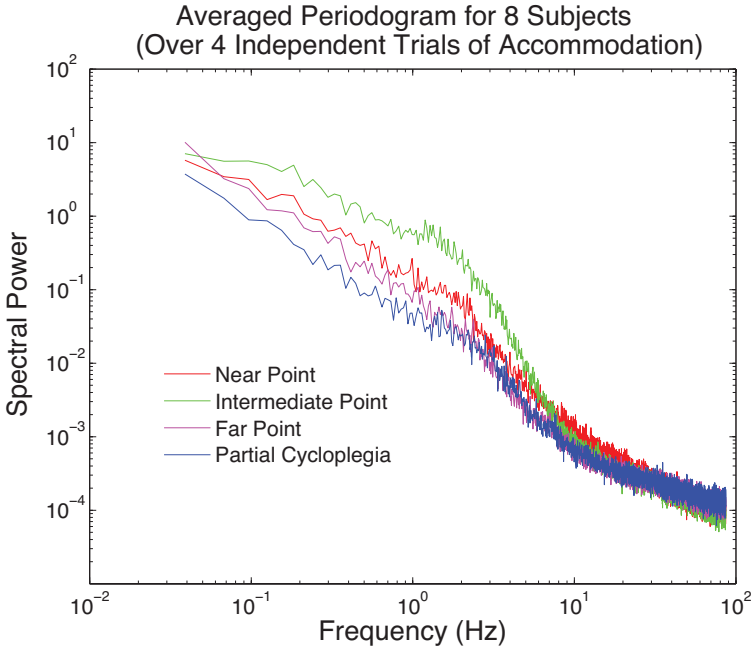

Figure 5.6: Averaged periodograms of the accommodative response for different accommodative conditions. Each trace represents the average estimated spectral power across 9 subjects. Data analysis by Conor Leahy.

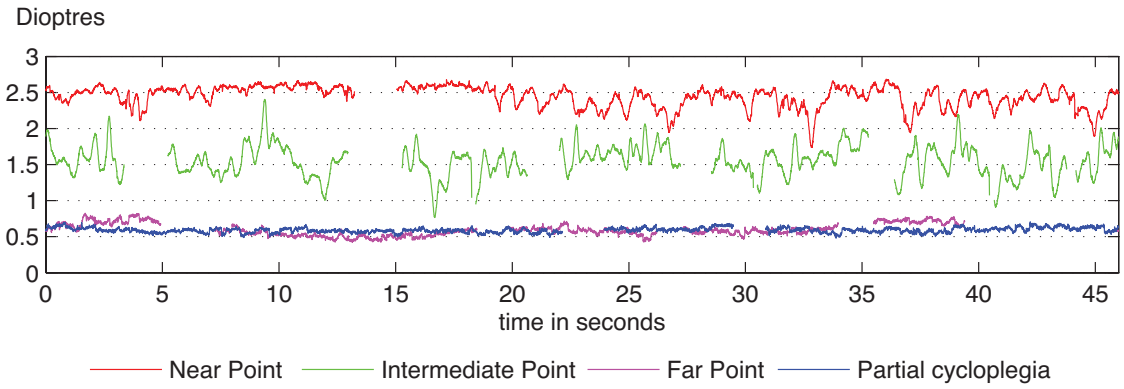

Figure 5.7: Time series measurements of accommodation for subject ED at the 4 viewing conditions. During the near point measurement, the subject was unable to fully hold fixation from $t = 25$ s onwards.

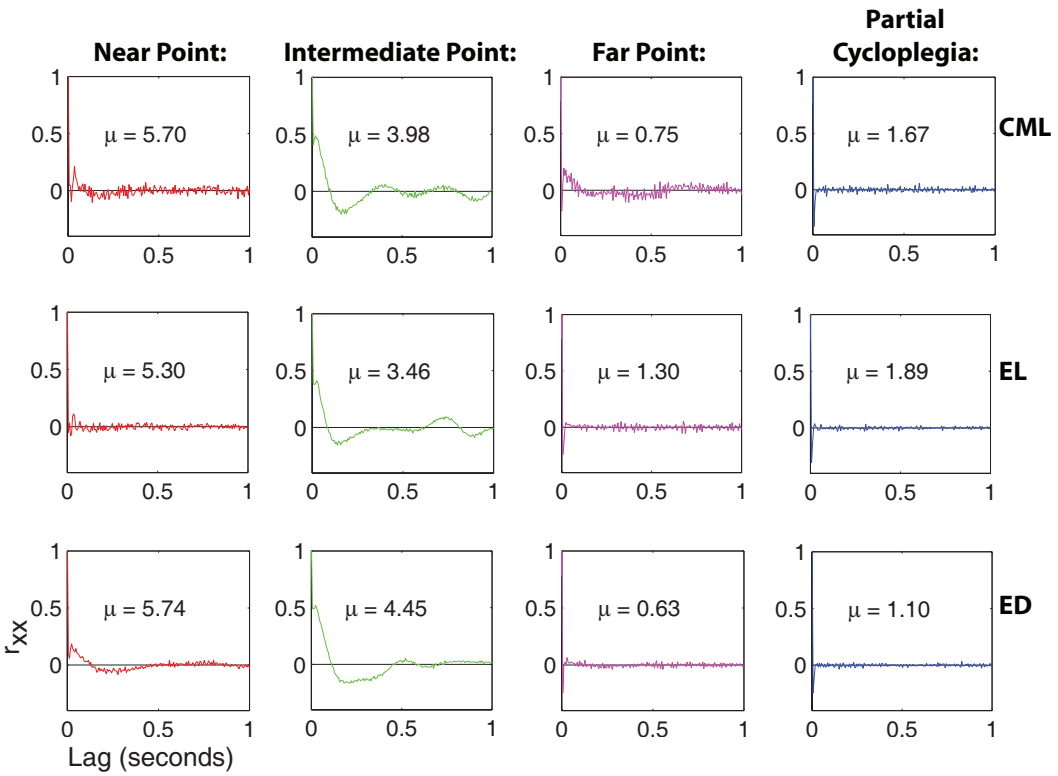

Figure 5.8: Normalised ACF of the increments of the Zernike defocus Z_2^0 for 3 subjects at each of the 4 viewing conditions. Data analysis by Conor Leahy.

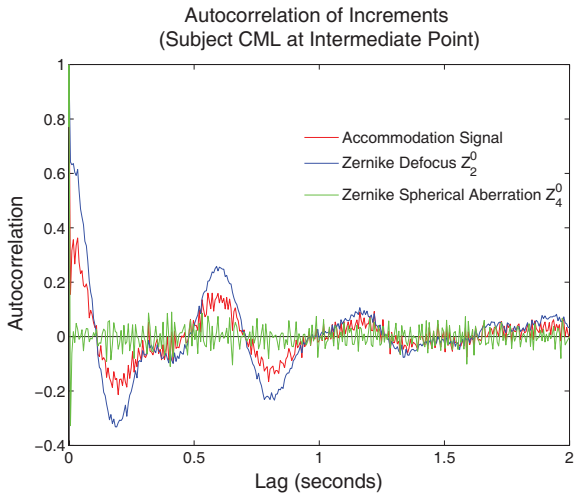

Figure 5.9: Illustration of the effects of noise on the autocorrelation of the increments. The spherical aberration term $z_{4,0}$ is more greatly affected by noise than the Zernike defocus $z_{2,0}$ term. Data analysis by Conor Leahy.

Chapter 6

Conclusions

Remarks on the instrumentation

Various tests of our custom-built aberrometer are presented in this thesis. They hopefully will be considered as a useful reference for the design of future aberrometers. The use of the Intevac CMOS camera as part of a SHWFS has been carefully investigated. We have shown that the light-insensitive regions of the detector have a negligible effect in the measurement process, for Shack-Hartmann spots larger than approximately 3 pixels FWHM.

For regions of interest of 400×400 pixels and smaller, we found that the frame rate of the CMOS is stable if it corresponds to half the maximal frame rate specified by Intevac. We implemented this frame rate reduction to obtain the two calibrated configurations of the SHWFS. (See Table 2.1.) We found that the 173 Hz configuration of our SHWFS (286×286 pixels, 3.9 mm pupil in the eye) was the fastest low-noise acquisition mode of the CMOS camera. At higher frame rates, we found that the readout noise of the CMOS increases for Shack-Hartmann spots with large signal. At a 173 Hz frame rate, we nevertheless found that spots with a peak signal larger than 700 DU should not be processed (see Figure 2.16).

The stability of the frame rate and the coupling of the SHWFS with the scanner have been carefully investigated, and calibrated for the two configurations of our SHWFS. (See Section 2.3.) We also identified in Chapter 2 the speckle effect of retinal scattering as a large source of noise: the PSD of the wavefront slope is reduced by a factor 60 with the scanner of our aberrometer. (See Figure 2.16.)

We think that the dynamics of the measured higher order aberrations are often driven by the drifts of the position of the eye, with respect to the aberrometer. Figure 4.10 shows for example, that a 0.2 μm drift of the coma was obtained for an eye shifted by 0.2 mm (for a 5.4 mm pupil). Using an additional (low-noise) CCD camera, we developed an "eye tracker" to measure the shifts of the eye's pupil during a measurement trial. The quality of the recorded frames was excellent, as we show in Figure 6.1 (c). This allowed us to have a good sensitivity in the measurement of the shift of the pupil. We later found out that the pupil of the eye can also be accurately detected from the Shack-Hartmann frames, using the background light which comes from retinal scattering and an adequate thresholding. To do so, the field of view of the SHWFS must be larger than the measured pupil. Using a 600×600 pixels region of interest of the CMOS makes this requirement possible for most eyes. Figure 6.1 shows a 600×600 pixels Shack-Hartmann frame (a), and the detected pupil using a simple thresholding/binarisation of this frame (b). The advantage of this technique of eye tracking is that the shift of the pupil is perfectly synchronous to the measurements of ocular aberrations. To suppress this measurement artefact, the measurement of the dynamics of the higher order aberrations require the use of an eye tracker.

The bandwidth of an ophthalmic AO system should be high enough to correct the dynamics of ocular aberrations, and in particular it should compensate for the effects of the shift of the pupil with respect to the instrument. Eye movements have a complex impact on the data recorded by a retinal imaging system, because fixational movements also play a major role. This issue depends on the type of imaging system (OCT, SLO, or flood illumination). For a high resolution imaging system, fixational eye movements are a major nuisance, and cannot be corrected by the AO system alone. They require the implementation of an image stabilisation system, which is usually software-based.

From a clinical perspective, the understanding in the dynamics of ocular wavefronts can give an inside in the temporal variations of the structure of the tear film. Tear film build up and break up are likely to be associated with (small) variations of higher order aberrations. We think that, to address this issue, an aberrometer should use an eye tracker and correct the effects of eye movements.

The spatial sampling of the wavefront sensor is also an issue for a study of the tear film. Self-referenced interferometric methods have provided nice sequences of temporal variation of the tear film, as long as it remains smooth. When the tear film breaks up, the reconstruction of the corneal topography from the processed fringes is almost impossible. Understanding the ability and the limitation of the SHWFS to

resolve the temporal evolution of the tear film requires further investigations.

Understanding the origin of the dynamics of ocular aberrations might be relevant for vision scientists who work on the visual benefit of customised correction of ocular aberrations. For this application, pupil misalignments also have a major impact, which can be simply quantified by numerically translating wavefront maps. We show in Table 4.3 that a 0.4 mm misalignment is enough to completely cancel the benefit of a perfect correction of higher order aberrations, for a typical ocular wavefront as measured by Thibos et al. over a 6 mm pupil. This benefit has been computed as a *wavefront rms error* $\varepsilon_{\text{align}}$, and it might be interesting to compute the impact of misalignment in terms of *retinal image quality*.

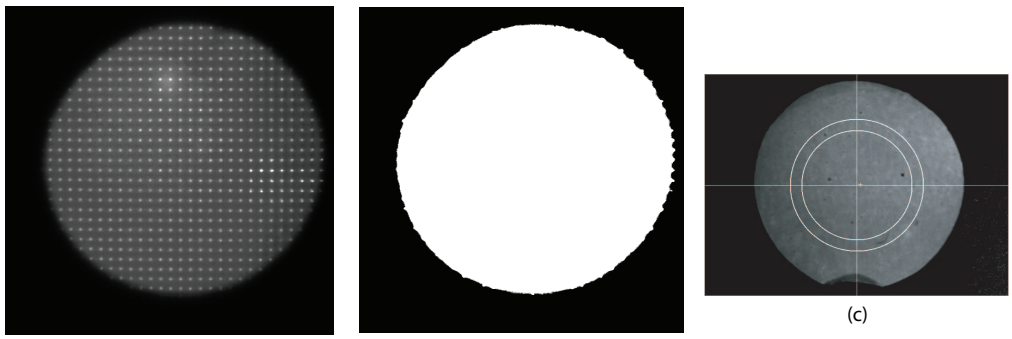

Figure 6.1: (a): 600×600 pixels Shack-Hartmann frame, which corresponds to a 8 mm field of view. (b): Direct measurement of the size and position of the pupil, after thresholding/binarisation of (a). (c): Image of the pupil as we recorded with a more sophisticated eye tracker that uses an additional CCD camera. (See Section 4.3.3.)

We also found that the fluctuations of accommodations are usually more relevant than the fluctuations of higher order aberrations. Figure 6.2 illustrates this remark. For a 3.9 mm pupil, the measured Zernike defocus $z_{2,0}$ has much higher fluctuations than the rms of the higher order aberrations. To first order, the change of power of the crystalline lens is thus homogeneous over the 3.9 mm pupil. As we briefly discuss in Section 4.2.3, the computation of the power of the eye from the Shack-Hartmann data is ambiguous. It depends on the computational method, and we interpret these artefacts by the fact that (spatial) derivation usually tends to amplify measurement errors. The description of the spatial statistics of the microfluctuations of accommodation thus requires more experimental and computational investigations.

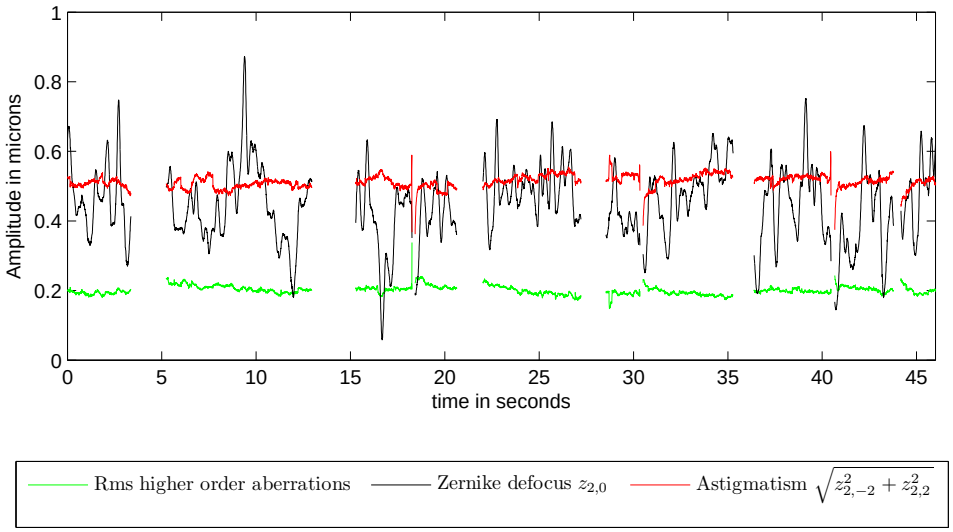

Figure 6.2: Time series of the Zernike aberrations: defocus, astigmatism, and higher order abberations (Subject ED at intermediate viewing, measured over a 3.9 mm pupil).

Our observations of the physics of the accommodative system

Our custom-built aberrometer has a fine spatio-temporal sampling, which we use to somehow "oversample" the dynamics of accommodation. Oversampling is a common (and wise) practice when measuring biological signals.

Accommodation is a complex mechanism, and the conditions under which the accommodative system is able to maintain a stable focus has been debated in a large body of literature [111]. Vision scientists usually refer to the term *blur-sensitivity* to describe the ability of a subject to find (and maintain) a stable focus *using image quality only*. This ability is usually measured under conditions for which the subject does not have any clues about the position of the target. It is probably related to the subjective depth of focus of the eye, which is parameterised by the fixation target (luminance, size, and contrast), the point spread function of the eye (pupil size and ocular aberrations), and other physiological processes such as the distribution and the alignment of the photoreceptors.

Our comprehension of the accommodative system is that the depth of focus of the eye influences the presence of drifts in the dynamics of the accommodative response, whereas the microfluctuations of higher frequencies are driven by what we refer to as the "accommodative effort" (i.e. the physics of the crystalline lens). In particular, our results tend to show that the microfluctuations have a maximal amplitude for a

mean effort of 4 D approximatively, independent of the refractive error of the subject. We think that this maximal activity is quantified by the slope of the PSD in the 2-10 Hz range, on a log log scale (m_2 in Table 5.1). The maximal activity that we measured at the intermediate point was also confirmed by the long lasting decay of the ACF of the increments of the accommodative response.

Drifts of the accommodative response were not considered of particular relevance in our experiments. They were in fact considered as aretefacts, because they would mix the different experimental conditions. This is especially true for the intermediate and the near points, as we illustrated in Figure 5.7. Our study presented an experiment for which the blur sensitivity was in principle kept as constant as possible, because the target remained unchanged with the accommodative demand (size and luminance), and was seen monocularly by the subject. At the near point, we think that eye fatigue might have play an important role in the occasional drifts and jumps of the measured responses. Other sources of unstability of the accommodative system include bad retinal quality due to uncorrected astigmatism, higher order aberrations, and the absence of proximity clues that are usually provided by an open viewing of the fixation target.

Quantifying the stabilisation of the accommodative response is of primary importance to understand the mechanisms that drive accommodation. To do so, the amplitude of the low frequency component of the estimated PSD has been analysed in many studies [120, 123, 124, 130]. We suggest that the slope m_1 of the PSD in the low frequency region might be an efficient way of estimating focus stabilisation. It is generally used to test power law random processes for stationarity [217]. For the three most experienced subjects of our study (CML, ED and CEL), the slope m_1 at the intermediate point is noticeably lower than for the other subjects and conditions, with values of 0.4, 0.7, and 0.4 (compared to the average of 0.9, see Table 5.1). This observation suggests that the microfluctuations of accommodation might be used by some subjects to stabilise their focus.

With the recent development of numerous AO systems for the eye, the role of higher order aberrations in the accommodative system has been extensively studied [132, 134–138]. Higher order aberrations can give a non-symetrical aspect in the through focus blur of the retinal image, and can therefore provide some directional clues to the accommodative system. During our experiments, some subjects with uncorrected astigmatism clearly observed the optical effect of the fluctuations of accommodation. Figure 6.3 shows the simulated through-focus image of a 6/12 Snellen O (10 arcmin of extend) for a fixed amount of astigmatism (first row, $z_{2,2} = 0.25\ \mu$m)

and coma (second row, $z_{3,-1} = 0.25$ μm). Astigmatism obviously gives more information than coma about the sign of the defocus error, and this observation should be considered for the design of other experiments on accommodation. We think that an interesting application of the mathematical tools presented in Chapter 5 is the simulation of realistic accommodative responses using deformable mirror. In particular, the visual impact of the microfluctuations could be assessed among cyclopleged subjects using psychophysical tests.

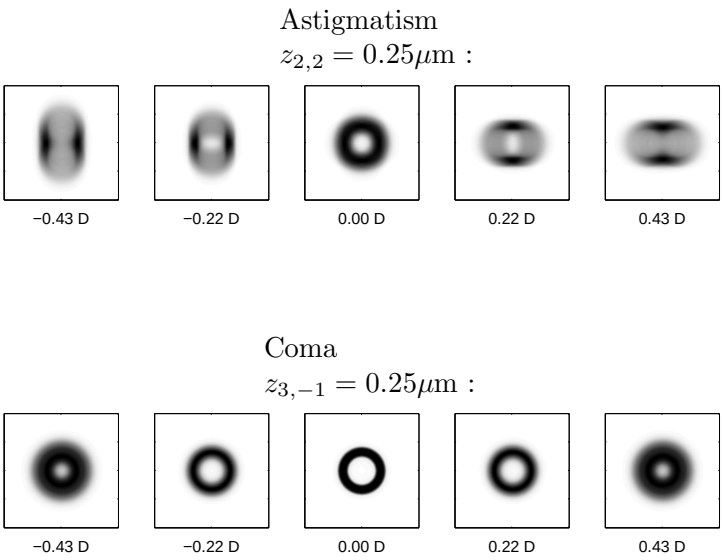

Figure 6.3: Through-focus retinal images of a"6/12 Snellen O" (extend of 10 arcmin), perceived through a 4 mm pupil by a subject with a some Zernike aberrations of rms 0.25 μm. Top: astigmatism $z_{2,2}$. Bottom: coma $z_{3,-1}$. Astigmatism provides a very efficient directional clue to the accommodative system. Courtesy of Eugenie Dalimier.

Bibliography

[1] D. Malacara. *Optical Shop Testing*. Wiley-Interscience, 2007.

[2] A. Morales and D. Malacara. Geometrical parameters in the Hartmann test of aspherical mirrors. *Appl. Opt.*, 22(24):3957–3959, 1983.

[3] M. Mrochen, M. Kaemmerer, P. Mierdel, H. Rinke, and T. Seiler. Principles of Tscherning aberrometry. *J. Ref. Surg.*, 16:570–571, 2000.

[4] M. Tscherning. Die monochromatischen Aberrationen des menschlichen Auges. *Z. Psychol. Physiol. Sinn.*, 6:456–471, 1894.

[5] B. Howland. Use of crossed cylinder lens in photographic lens evaluation. *Appl. Opt.*, 7(8):1587–1600, 1968.

[6] H.C. Howland and B. Howland. A subjective method for the measurement of monochromatic aberrations of the eye. *J. Opt. Soc. Am.*, 67(11):1508–1518, 1977.

[7] G. Walsh, W.N. Charman, and H.C. Howland. Objective technique for the determination of monochromatic aberrations of the human eye. *J. Opt. Soc. Am. A*, 1(9):987–992, 1984.

[8] G. Smith, R.A. Applegate, and D.A. Atchison. Assessment of the accuracy of the crossed-cylinder aberroscope technique. *J. Opt. Soc. Am. A*, 15(9):2477–2487, 1998.

[9] M.J. Cox and R. Calver. Reassessing the theoretical accuracy of the crossed-cylinder aberroscope technique. *J. Opt. Soc. Am. A*, 16(10):2343–2351, 1999.

[10] H.S. Smirnov. Measurement of the wave aberration in the human eye. *Biophys.*, 6:52–66, 1961.

[11] R.H. Webb, C.M. Penney, and K.P. Thompson. Measurement of ocular local wavefront distortion with a spatially resolved refractometer. *Appl. Opt.*, 31(19):3678–3686, 1992.

[12] J.C. He, S. Marcos, R.H. Webb, and S.A. Burns. Measurement of the wave-front aberration of the eye by a fast psychophysical procedure. *J. Opt. Soc. Am. A*, 15(9):2449–2456, 1998.

[13] R. Navarro and E. Moreno-Barriuso. Laser ray-tracing method for optical testing. *Opt. Lett.*, 24(14):951–953, 1999.

[14] E. Moreno-Barriuso and R. Navarro. Laser ray tracing versus Hartmann-Shack sensor for measuring optical aberrations in the human eye. *J. Opt. Soc. Am. A*, 17(6):974–985, 2000.

[15] J.H. Burge. *Advanced Techniques for measuring primary mirrors for astronomical telescopes*. PhD thesis, University of Arizona, 1993.

[16] S. Bará. Measuring eye aberrations with Hartmann Shack wave-front sensors: Should the irradiance distribution across the eye pupil be taken into account? *J. Opt. Soc. Am. A*, 20(12):2237–2245, 2003.

[17] R.C. Cannon. Global wave-front reconstruction using Shack-Hartmann sensors. *J. Opt. Soc. Am. A*, 12:2031–2039, 1995.

[18] H.H. Barrett, J.C. Dainty, and D.Lara. Maximum-likelihood methods in wavefront sensing: stochastic models and likelihood functions. *J. Opt. Soc. Am. A*, 24:391–414, 2007.

[19] J. Primot. Theoretical description of Shack-Hartmann wave-front sensor. *Optics Communications*, 222(1-6):81 – 92, 2003.

[20] Y. Carmon and E.N. Ribak. Phase retrieval by demodulation of a Hartmann-Shack sensor. *Optics Communications*, 215(4-6):285 – 288, 2003.

[21] N. Lindlein, J. Pfund, and J. Schwider. Algorithm for expanding the dynamic range of a Shack-Hartmann sensor by using a spatial light modulator array. *Optical Engineering*, 40(5):837–840, 2001.

[22] G. Yoon, S. Pantanelli, and L.J. Nagy. Large-dynamic-range Shack-Hartmann wavefront sensor for highly aberrated eyes. *Journal of Biomedical Optics*, 11(3):030502, 2006.

[23] L.E. Schmutz and B.M. Levine. Hartmann sensors detect optical fabrication errors. *Laser Focus World*, 32, 1996.

[24] X. Levecq and S. Bucourt. Method and device for analysing a highly dynamic wavefront. *U.S. Patent*, (6,750,957B1), 2004.

[25] N. Lindlein, J. Pfund, and J. Schwider. Expansion of the dynamic range of a Shack-Hartmann sensor by using astigmatic microlenses. *Optical Engineering*, 39(8):2220–2225, 2000.

[26] N. Lindlein and J. Pfund. Experimental results for expanding the dynamic range of a Shack-Hartmann sensor using astigmatic microlenses. *Optical Engineering*, 41(2):529–533, 2002.

[27] J. Pfund, N. Lindlein, and J. Schwider. Dynamic range expansion of a Shack-Hartmann sensor by use of a modified unwrapping algorithm. *Opt. Lett.*, 23(13):995–997, 1998.

[28] S. Groening, B. Sick, K. Donner, J. Pfund, N. Lindlein, and J. Schwider. Wavefront reconstruction with a Shack-Hartmann sensor with an iterative spline fitting method. *Appl. Opt.*, 39(4):561–567, 2000.

[29] D.G. Smith and J.E. Greivenkamp. Generalized method for sorting Shack-Hartmann spot patterns using local similarity. *Appl. Opt.*, 47(25):4548–4554, 2008.

[30] L. Lundström and P. Unsbo. Shack images from highly aberrated eyes using an iterative B-spline based extrapolation method. *Optom. Vis. Sci.*, 81(5):383–388.

[31] M.C. Roggemann and T.J. Schulz. Algorithm to increase the largest aberration that can be reconstructed from Hartmann sensor measurements. *Appl. Opt.*, 37(20):4321–4329, 1998.

[32] C. Leroux and C. Dainty. A simple and robust method to extend the dynamic range of an aberrometer. *Opt. Express*, 17(21):19055–19061, 2009.

[33] L. Diaz-Santana and J.C. Dainty. Effects of retinal scattering in the ocular double-pass process. *J. Opt. Soc. Am. A*, 18:1437–1444, 2001.

[34] L. Diaz Santana Haro and J.C. Dainty. Single vs symmetric and asymmetric double-pass measurements of the wavefront aberration of the human eye. *Second International Workshop on Adaptive Optics for Industry and Medicine*, 2000.

[35] H. Hofer, P. Artal, B. Singer, J.L. Aragon, and D.R. Williams. Dynamics of the eye's wave aberration. *J. Opt. Soc. Am. A*, 18:497–506, 2001.

[36] J.W. Goodman. *Speckle Phenomena in Optics*. Roberts-publishers, 2007.

[37] L. Diaz Santana Haro and J.C. Dainty. Single-pass measurements of the wavefront aberrations of the human eye by use of retinal lipofuscin autofluorescence. *Opt. Lett.*, 24:61–63, 1999.

[38] R. Ragazzoni. Pupil plane wavefront sensing with an oscillating prism. *J. Mod. Opt.*, 43:289–293, 1996.

[39] Ignacio Iglesias, Roberto Ragazzoni, Yves Julien, and Pablo Artal. Extended source pyramid wave-front sensor for the human eye. *Opt. Express*, 10(9):419–428, 2002.

[40] F. Bernu and S. Slansky. Wavefront determination resulting from Foucault test as applied to the human eye and visual instrument optical instruments and techniques. *Optical instruments and techniques*, pages 375–386, 1970.

[41] S.R. Chamot, C. Dainty, and S. Esposito. Adaptive optics for ophthalmic applications using a pyramid wavefront sensor. *Opt. Express*, 14(2):518–526, 2006.

[42] R. Ragazzoni and J. Farinato. Sensitivity of a pyramidic wave front sensor in closed loop adaptive optics. *Astron. Astrophys.*, 350:23–26, 1999.

[43] A. Burvall, E. Daly, S.R. Chamot, and C. Dainty. Linearity of the pyramid wavefront sensor. *Opt. Express*, 14(25):11925–11934, 2006.

[44] J.P. Véran and G. Herriot. Centroid gain compensation in Shack-Hartmann adaptive optics systems with natural or laser guide star. *J. Opt. Soc. Am. A*, 17(8):1430–1439, 2000.

[45] M.A. van Dam. Measuring the centroid gain of a Shack-Hartmann quad-cell wavefront sensor by using slope discrepancy. *J. Opt. Soc. Am. A*, 22(8):1509–1514, 2005.

[46] F. Roddier. Wavefront sensing and the irradiance transport equation. *Appl. Opt.*, 29(10):1402–1403, 1990.

[47] H. I. Campbell, S. Zhang, A. H. Greenaway, and S. Restaino. Generalized phase diversity for wave-front sensing. *Opt. Lett.*, 29(23):2707–2709, 2004.

[48] F. Roddier. Curvature sensing and compensation: a new concept in adaptive optics. *Appl. Opt.*, 27(7):1223–1225, 1988.

[49] D.J. Lee, Michael C. Roggemann, and B.M. Welsh. Cramér-rao analysis of phase-diverse wave-front sensing. *J. Opt. Soc. Am. A*, 16(5):1005–1015, 1999.

[50] S. Gruppetta, L. Koechlin, F. Lacombe, and P. Puget. Curvature sensor for the measurement of the static corneal topography and the dynamic tear film topography in the human eye. *Opt. Lett.*, 30(20):2757–2759, 2005.

[51] F. Díaz-Doutón, J. Pujol, M. Arjona, and S. O. Luque. Curvature sensor for ocular wavefront measurement. *Opt. Lett.*, 31(15):2245–2247, 2006.

[52] C. Torti, S. Gruppetta, and L. Diaz-santana. Wavefront curvature sensing for the human eye. *Journal of Modern Optics*, 55(4-5):691 – 702, 2008.

[53] S. Gruppetta, F. Lacombe, and P. Puget. Study of the dynamic aberrations of the human tear film. *Opt. Express*, 13:7631–7636, 2005.

[54] J. Liang. *A new method to precisely measure the wave aberrations of the human eye with a Hartmann-Shack- Wavefront-Sensor*. PhD thesis, 1991.

[55] J. Liang, B. Grimm, S. Goelz, and J.F. Bille. Objective measurement of wave aberrations of the human eye with the use of a Hartmann-Shack wave-front sensor. *J. Opt. Soc. Am. A*, 11(7):1949–1957, 1994.

[56] J. Liang, D.R. Williams, and D.T. Miller. Supernormal vision and high-resolution retinal imaging through adaptive optics. *J. Opt. Soc. Am. A*, 14(11):2884–2892, 1997.

[57] L.N. Thibos, X. Hong, A. Bradley, and X. Cheng. Statistical variation of aberration structure and image quality in a normal population of healthy eyes. *J. Opt. Soc. Am. A*, 19(12):2329–2348, 2002.

[58] J. Porter, A. Guirao, I.G. Cox, and D.R. Williams. Monochromatic aberrations of the human eye in a large population. *J. Opt. Soc. Am. A*, 18(8):1793–1803, 2001.

[59] M.P. Cagigal, V.F. Canales, J.F. Castejon-Mochon, P.M. Prieto, N. Lopez-Gil, and P. Artal. Statistical description of wave-front aberration in the human eye. *Opt. Lett.*, 27:36–39, 2002.

[60] J. Braat. Polynomial expansion of severely aberrated wave fronts. *J. Opt. Soc. Am. A*, 4(4):643–650, 1987.

[61] V.N. Mahajan. *Optical Imaging and Aberrations*. SPIE-Press, 1998.

[62] L.N. Thibos, A. Bradley, and R. A. Applegate. Accuracy and Precision of Objective Refraction from Wavefront Aberrations. *2003 ARVO Annual Meeting*.

[63] L.N. Thibos, M. Ye, Xi. Zhang, and A. Bradley. The chromatic eye: a new reduced-eye model of ocular chromatic aberration in humans. *Appl. Opt.*, 31(19):3594–3600, 1992.

[64] J.S. McLellan, P.M. Prieto, S. Marcos, and S.A. Burns. Effects of interactions among wave aberrations on optical image quality. *Vision Research*, 46(18):3009 – 3016, 2006.

[65] N. Davies, L. Diaz-Santana, and D. Lara-Saucedo. Repeatability of ocular wavefront measurement. *Optom. and Vis. Science*, 80(2):142 – 150, 2003.

[66] X. Cheng, N.L. Himebaugh, P.S. Kollbaum, L.N. Thibos, and A. Bradley. Test retest reliability of clinical Shack-Hartmann measurements. *Invest. Ophthalmol. Vis. Sci.*, 45(1):3413–3420, 2004.

[67] M.A. Miranda, C. O'Donnell, and R. Hadhkrishnan. Repeatability of corneal and ocular aberration measurements and changes in aberrations over one week. *Clin. Exp. Optom.*, 92(3):253–266, 2009.

[68] S. Srivannaboon, D. Reinstein, and T. Archer. Diurnal variation of higher order aberrations in human eyes. *J. Refract. Surg.*, 23:442–446, 2007.

[69] M. Asejczyk-Widlicka and B. Pierscionek. Fluctuations in intraocular pressure and the potential effect on aberrations of the eye. *Br. J. Opthalmology*, 91:1054–1058, 2007.

[70] J.S. McLellan, S. Marcos, and S.A. Burns. Age-related changes in monochromatic wave aberrations of the human eye. *Invest. Ophthalmol. Vis. Sci.*, 42:1390Ű1395, 2001.

[71] P. Artal, E. Berrio, A. Guirao, and P. Piers. Contribution of the cornea and internal surfaces to the change of ocular aberrations with age. *J. Opt. Soc. Am. A*, 19(1):137–143, 2002.

[72] I. Escudero-Sanz and R. Navarro. Off-axis aberrations of a wide-angle schematic eye model. *J. Opt. Soc. Am. A*, 16(8):1881–1891, 1999.

[73] A.V. Goncharov and C. Dainty. Wide-field schematic eye models with gradient-index lens. *J. Opt. Soc. Am. A*, 24(8):2157–2174, 2007.

[74] M.T. Sheehan, A. V. Goncharov, V.M. O'Dwyer, V. Toal, and C. Dainty. Population study of the variation in monochromatic aberrations of the normal human eye over the central visual field. *Opt. Express*, 15(12):7367–7380, 2007.

[75] A.V. Goncharov, M. Nowakowski, M.T. Sheehan, and C. Dainty. Reconstruction of the optical system of the human eye with reverse ray-tracing. *Opt. Express*, 16(3):1692–1703, 2008.

[76] X. Wei and L. Thibos. Modeling the eye's optical system by ocular wavefront tomography. *Opt. Express*, 16(25):20490–20502, 2008.

[77] J.C. He, S.A. Burns, and S. Marcos. Monochromatic aberrations in the accommodated human eye. *Vision Research*, 40(1):41–48, 2000.

[78] H. Cheng, J.K. Barnett, A.S. Vilupuru, J.D. Marsack, S. Kasthurirangan, R.A. Applegate, and A. Roorda. A population study on changes in wave aberrations with accommodation. *Journal of Vision*, 4(4):281–287, 2004.

[79] R. Navarro, J. Santamaría, and J. Bescós. Accommodation-dependent model of the human eye with aspherics. *J. Opt. Soc. Am. A*, 2(8):1273–1280, 1985.

[80] A.V. Goncharov and C. Dainty. Wide-field schematic eye models with gradient-index lens. *J. Opt. Soc. Am. A*, 24(8):2157–2174, 2007.

[81] M.S. Rajan, I. Keilhorn, and J.A. Bell. Partial coherence laser interferometry vs conventional ultrasound biometry in intraocular lens power calculations. *Eye*, 16(5):662–556, 2002.

[82] J. Tabernero, A. Benito, V. Nourrit, and P. Artal. Instrument for measuring the misalignments of ocular surfaces. *Opt. Express*, 14(22):10945–10956, 2006.

[83] P. Rosales and S. Marcos. Phakometry and lens tilt and decentration using a custom-developed purkinje imaging apparatus: validation and measurements. *J. Opt. Soc. Am. A*, 23(3):509–520, 2006.

[84] A. de Castro, P. Rosales, and S. Marcos. Tilt and decentration of intraocular lenses in vivo from purkinje and scheimpflug imaging: Validation study. *J. Cat. Ref. Surg.*, 33(3):418 – 429, 2007.

[85] P. Rosales and S. Marcos. Customized computer models of eyes with intraocular lenses. *Opt. Express*, 15(5):2204–2218, 2007.

[86] P. Rosales, M. Dubbelman, S. Marcos, and R. van der Heijde. Crystalline lens radii of curvature from Purkinje and Scheimpflug imaging. *J. Vis.*, 6(10):1057–1067, 9 2006.

[87] J.E. Kelly, T. Mihashi, and H.C. Howland. Compensation of corneal horizontal/vertical astigmatism, lateral coma, and spherical aberration by internal optics of the eye. *Journal of Vision*, 4(4):262–271, 2004.

[88] J. Tabernero, A. Benito, E. Alcón, and P. Artal. Mechanism of compensation of aberrations in the human eye. *J. Opt. Soc. Am. A*, 24(10):3274–3283, 2007.

[89] P. Artal, A. Benito, and J. Tabernero. The human eye is an example of robust optical design. *Journal of Vision*, 6(1):1–7, 1 2006.

[90] S. Marcos, P. Rosales, L. Llorente, S. Barbero, and I. JimŐnez Alfaro. Balance of corneal horizontal coma by internal optics in eyes with intraocular artificial lenses: Evidence of a passive mechanism. *Vision Research*, 48(1):70 – 79, 2008.

[91] R.B. Mandell. A guide to videokeratography. *International Contact Lens Clinic*, 23(6):205 – 228, 1996.

[92] T.O. Salmon and L.N. Thibos. Videokeratoscope-line-of-sight misalignment and its effect on measurements of corneal and internal ocular aberrations. *J. Opt. Soc. Am. A*, 19(4):657–669, 2002.

[93] A. Roorda and D.R. Williams. Adaptive optics and retinal imaging. In *Vision Science and its Applications*, page NW5. Optical Society of America, 2000.

[94] J. Carroll, D.C. Gray, A. Roorda, and D.R. Williams. Recent advances in retinal imaging with adaptive optics. *Opt. Photon. News*, 16(1):36–42, 2005.

[95] J.C. Christou, A. Roorda, and D.R. Williams. Deconvolution of adaptive optics retinal images. *J. Opt. Soc. Am. A*, 21(8):1393–1401, 2004.

[96] A. Roorda, F. Romero-Borja, W. Donnelly, H. Queener, T. Hebert, and M. Campbell. Adaptive optics scanning laser ophthalmoscopy. *Opt. Express*, 10(9):405–412, 2002.

[97] D.X. Hammer, R.D. Ferguson, C.E. Bigelow, N.V. Iftimia, T.E. Ustun, and S.A. Burns. Adaptive optics scanning laser ophthalmoscope for stabilized retinal imaging. *Opt. Express*, 14(8):3354–3367, 2006.

[98] C. Vogel, D. Arathorn, A. Roorda, and A. Parker. Retinal motion estimation in adaptive optics scanning laser ophthalmoscopy. *Opt. Express*, 13(26), 2005.

[99] S.A. Burns, R. Tumbar, A.E. Elsner, D. Ferguson, and D.X. Hammer. Large-field-of-view, modular, stabilized, adaptive-optics-based scanning laser ophthalmoscope. *J. Opt. Soc. Am. A*, 24(5):1313–1326, 2007.

[100] B. Hermann, E.J. Fernández, A. Unterhuber, H. Sattmann, A.F. Fercher, W. Drexler, P.M. Prieto, and P. Artal. Adaptive-optics ultrahigh-resolution optical coherence tomography. *Opt. Lett.*, 29(18):2142–2144, 2004.

[101] Y. Chen, L.N. Vuong, J. Liu, J. Ho, V.J. Srinivasan, I. Gorczynska, A.J. Witkin, J.S. Duker, J. Schuman, and J.G. Fujimoto. Three-dimensional ultrahigh resolution optical coherence tomography imaging of age-related macular degeneration. *Opt. Express*, 17(5):4046–4060, 2009.

[102] G. Yoon and D.R. Williams. Visual performance after correcting the monochromatic and chromatic aberrations of the eye. *J. Opt. Soc. Am. A*, 19(2):266–275, 2002.

[103] D.R. Williams. Visibility of interference fringes near the resolution limit. *J. Opt. Soc. Am. A*, 2(7):1087–1093, 1985.

[104] E. Dalimier. *Adaptive Optics Correction of Ocular Higher-Order Aberrations and the Effects on Functional Vision*. PhD thesis, 2007.

[105] R. Navarro, E. Moreno-Barriuso, S. Bará, and T. Mancebo. Phase plates for wave-aberration compensation in the human eye. *Opt. Lett.*, 25(4):236–238, 2000.

[106] S.A. Burns, S. Marcos, A.E. Elsner, and S. Bará. Contrast improvement of confocal retinal imaging by use of phase-correcting plates. *Opt. Lett.*, 27(6):400–402, 2002.

[107] J. Arines and S. Bará. Hybrid technique for high resolution imaging of the eye fundus. *Opt. Express*, 11(7):761–766, 2003.

[108] L. Diaz-Santana, I. Munro, P. Gasson, and C. Dainty. Benefit of higher closed loop bandwidths in ocular adaptive optics. *Opt. Express*, 11:2597–2602, 2003.

[109] T. Nirmaier, G. Pudasaini, and J. Bille. Very fast wave-front measurements at the human eye with a custom cmos-based Hartmann–Shack sensor. *Opt. Express*, 11(21):2704–2716, 2003.

[110] S. Plainis, H. Ginis, and A. Pallikaris. The effect of ocular aberrations on steady-state errors of accommodative response. *Journal of Vision*, 5(5):466–477, 5 2005.

[111] W.N. Charman and G. Heron. Fluctuations in accommodation: a review. *Opthal. Physiol. Optics*, 8:153–164, 1988.

[112] A. Dubra, C. Paterson, and C. Dainty. Study of the tear topography dynamics using a lateral shearing interferometer. *Opt. Express*, 12:6278–6288, 2004.

[113] A. Dubra, C. Paterson, and C. Dainty. Double lateral shearing interferometer for the quantitative measurement of tear film topography. *Appl. Opt.*, 44(7):1191–1199, 2005.

[114] K.Y. Li and G. Yoon. Changes in aberrations and retinal image quality due to tear film dynamics. *Opt. Express*, 14(25):12552–12559, 2006.

[115] S. Koh, N. Maeda, Y. Hirohara, T. Mihashi, S. Ninomiya, K. Bessho, H. Watanabe, T. Fujikado, and Y. Tano. Serial measurements of higher-order aberrations after blinking in normal subjects. *Invest. Ophthalmol. Vis. Sci.*, 47:3318–3324, 2006.

[116] F.W. Campbell, J.G. Robson, and G. Westheimer. Fluctuations of accommodation under steady viewing conditions. *J. Physiol.*, 3(145):579–594, 1959.

[117] B. Winn, J.R. Pugh, B. Gilmartin, and H. Owens. Arterial pulse modulates steady-state ocular accommodation. *Current Eye Research*, 9(10):970–975, 1990.

[118] M. Collins, B. Davis, and J. Wood. Microfluctuations of steady-state accommodation and the cardiopulmonary system. *Vision Research*, 35(17):2491–2502, 1995.

[119] B. Winn, W.N. Charman, J.R. Pugh, G. Heron, and A.S. Eadie. Perceptual detectability of ocular accommodation microfluctuations. *J. Opt. Soc. Am. A*, 6(3):459–462, 1989.

[120] L.R. Stark and D.A. Atchison. Pupil size, mean accommodation response and the fluctuations of accommodation. *Ophthal. and Physiol. Optics*, 17(4):316 – 323, 1997.

[121] P. Denieul. Effects of stimulus vergence on mean accommodation response, microfluctuations of accommodation and optical quality of the human eye. *Vision Research*, 22(15):561 – 569, 1983.

[122] C. Miege and P. Denieul. Mean response and oscillations of accommodation for various stimulus vergences in relation to accommodation feedback control. *Ophthal. and Physiol. Optics*, 8(2):165–171, 1988.

[123] L.S. Gray, B. Winn, and B. Gilmartin. Accommodative microfluctuations and pupil diameter. *Vision Research*, 33(15):2083 – 2090, 1993.

[124] L.S. Gray, B. Winn, and B. Gilmartin. Effect of target luminance on microfluctuations of accommodation. *Ophthal. and Physiol. Optics*, 13(3):258–265, 1993.

[125] G.L. van der Heijde, A.P.A. Beers, and M. Dubbelman. Microfluctuations of steady-state accommodation measured with ultrasonography. *Opthal. Physiol. Opt.*, 16(3):216–221, 1996.

[126] M. Zhu, M.J. Collins, and D.R. Iskander. Microfluctuations of wavefront aberrations of the eye. *Opthal. Physiol. Optics*, 24:562–571, 2004.

[127] K.M. Hampson, I. Munro, C. Paterson, and C. Dainty. Weak corelation between the aberration dynamics of the human eye and the cardiopulmonary system. *J. Opt. Soc. Am. A*, 22:1241–1250, 2005.

[128] J.C. Kotulak and C.M. Schor. Temporal variations in accommodation during steady-state conditions. *J. Opt. Soc. Am.*, 54:189–194, 1986.

[129] F.W. Campbell and G. Westheimer. Factors influencing accommodation responses of the human eye. *J. Opt. Soc. Am.*, 49(6):568–571, 1959.

[130] M. Alpern. Variability of accommodation during steady fixation at various levels of illuminance. *J. Opt. Soc. Am.*, 48(3):193–197, 1958.

[131] L.R. Stark, N.C. Strang, and D.A. Atchison. Dynamic accommodation response in the presence of astigmatism. *J. Opt. Soc. Am. A*, 20(12):2228–2236, 2003.

[132] K.M. Hampson, C. Paterson, C. Dainty, and E.A.H. Mallen. Adaptive optics system for investigation of the effect of the aberration dynamics of the human eye on steady-state accommodation control. *J. Opt. Soc. Am. A*, 23(5):1082–1088, 2006.

[133] G. Westheimer. Accommodation measurements in empty visual fields. *J. Opt. Soc. Am.*, 47(8):714–718, 1957.

[134] L. Chen, P.B. Kruger, H. Hofer, B. Singer, and D.R. Williams. Accommodation with higher-order monochromatic aberrations corrected with adaptive optics. *J. Opt. Soc. Am. A*, 23(1):1–8, 2006.

[135] E.J. Fernández and P. Artal. Study on the effects of monochromatic aberrations in the accommodation response by using adaptive optics. *J. Opt. Soc. Am. A*, 22(9):1732–1738, 2005.

[136] S.S. Chin, K.M. Hampson, and E.A.H. Mallen. Effect of correction of ocular aberration dynamics on the accommodation response to a sinusoidally moving stimulus. *Opt. Lett.*, 34(21):3274–3276, 2009.

[137] N. Lopez-Gil, F.J Rucker, L.R. Stark, M. Badar, T. Borgovan, and S. Burke. Effect of third order aberrations on dynamic accommodation. *Vision Research*, 47:755–765, 2007.

[138] E. Gambra, L. Sawides, C. Dorronsoro, and S. Marcos. Accommodative lag and fluctuations when optical aberrations are manipulated. *Journal of Vision*, 9(6):1–15, 2009.

[139] P.B. Kruger and J. Pola. Stimuli for accommodation: Blur, chromatic aberration and size. *Vision Research*, 26:957–971, 1986.

[140] P.B. Kruger, S. Mathews, K.R. Aggarwala, and N. Sanchez. Chromatic aberration and ocular focus: Fincham revisited. *Vision Research*, 33:1397–1411, 1993.

[141] P.B. Kruger, S. Nowbotsing, K.R. Aggarwala, and S. Mathews. Small amounts of chromatic aberration influence dynamic accommodation. *Optom. Vis. Sci.*, 72:656–666, 1995.

[142] D.R. Iskander, M. Collins, M. Morelande, and M. Zhu. Analyzing the dynamic wavefront aberrations in the human eye. *IEEE Transactions on Biomedical Engineering*, 51:1969–1980, 2004.

[143] C. Leroux and C. Dainty. Estimation of centroid positions with a matched-filter algorithm: relevance for aberrometry of the eye. *Opt. Express*, 18(2), 2010.

[144] C. Leahy, C. Leroux, C. Dainty, and L. Diaz-Santana. Temporal dynamics and statistical characteristics of the microfluctuations of accommodation: Dependence on the mean accommodative effort. *Opt. Express*, 18(3).

[145] J. Porter, H.M. Queener, J.E. Lin, K. Thorn, and A. Awwal, editors. *Adaptive Optics for Vision Science*. Wiley-Interscience, 2006.

[146] L. Diaz-Santana, G. Walker, and S. Bará. Sampling geometries for ocular aberrometry: A model for evaluation for performance. *J. Opt. Soc. Am. A*, 13:8801–8812, 2005.

[147] S. Bará. Characteristic functions of Hartmann-Shack wavefront sensors and laser-ray-tracing aberrometers. *J. Opt. Soc. Am. A*, 24(12):3700–3707, 2007.

[148] L. Llorente, S. Marcos, C. Dorronsoro, and S.A. Burns. Effect of sampling on real ocular aberration measurements. *J. Opt. Soc. Am. A*, 24(9):2783–2796, 2007.

[149] R.A. Applegate and V. Lakshminarayanan. Parametric representation of Stiles-Crawford functions: normal variation of peak location and directionality. *J. Opt. Soc. Am. A*, 10(7):1611–1623, 1993.

[150] S.A. Burns, S. Wu, F. Delori, and A.E. Elsner. Direct measurement of human-conephotoreceptor alignment. *J. Opt. Soc. Am. A*, 12(10):2329–2338, 1995.

[151] P.S. Binder, R.L. Lindstrom, R.D. Stulting, E. Donnenfeld, H. Wu, P. McDonnell, and Y. Rabinowitz. Keratoconus and corneal ectasia after lasik. *J. Cat. Ref. Surg.*, 31(11):2035 – 2038, 2005.

[152] M.B. Shapiro and T.D. France. The ocular features of Down's syndrom. *Am. J. Ophthalmol.*, 99(6):659–63, 1985.

[153] N. Maeda, T. Fujikado, and T. Kuroda. Wavefront aberrations measured with Hartmann-Shack sensor in patients with keratoconus. *Ophthalmology*, 109(11):1430–1439, 2002.

[154] S. Barbero, S. Marcos, S. Merayo-Lloves, J. Moreno, and E. Barriuso. Validation of the estimation of corneal aberrations from videokeratography in keratoconus. *J. Cat. Ref. Surg.*, 18(3), 2002.

[155] S. Pantanelli, S. MacRae, T. Jeong, and G. Yoon. Characterizing the wave aberration in eyes with keratoconus or penetrating keratoplasty using a high dynamic range wavefront sensor. *Ophthalmology*, 114(11):442–446, 2007.

[156] L.N. Thibos, R.A. Applegate, J.T. Schwiegerling, and R. Webb. Standards for reporting optical aberrations of eyes. *J. Ref. Surg.*, 18:652–660, 2000.

[157] J. Pfund, N. Lindlein, and J. Schwider. Misalignment effects of the Shack-Hartmann sensor. *Appl. Opt.*, 37(1):22–27, 1998.

[158] Y. Li and E. Wolf. Focal shifts in diffracted converging spherical waves. *Optics Communications*, 39:205–276, 1981.

[159] V.N. Mahajan. Axial irradiance and optimum focusing of laser beams. *Appl. Opt.*, 22(19):3042–3053, 1983.

[160] S. Bará, P. Prado, J. Arines, and J. Ares. Estimation-induced correlations of the Zernike coefficients of the eye aberration. *Opt. Lett.*, 31:2646–2648, 2006.

[161] F.C. Delori and K.P. Pflibsen. Spectral reflectance of the human ocular fundus. *Appl. Opt.*, 28:1061–1077, 1989.

[162] S. Marcos, L. Diaz-Santana, L. Llorente, and C. Dainty. Ocular aberrations with ray tracing and Shack–Hartmann wave-front sensors: Does polarization play a role? *J. Opt. Soc. Am. A*, 19(6):1063–1072, 2002.

[163] L. Llorente, L. Diaz-Santana, D. Lara-Saucedo, and S. Marcos. Aberrations of the human eye in visible and near infrared illumination. *Optom. Vis. Sci.*, 80:26–35, 2003.

[164] R.K. Tyson. *Principles of Adaptive Optics*. Academic press, 2 nd edition edition, 1998.

[165] H.H. Barrett and K.J. Myers. *Foundations of Image Science*. Wiley-Interscience, 2003.

[166] B.E.A. Saleh. Estimation of the location of an optical object with photodetectors limited by quantum noise. *Appl. Opt.*, 13(8):1824–1827, 1974.

[167] K.A. Winick. Cramér-rao lower bounds on the performance of charge-coupled-device optical position estimators. *J. Opt. Soc. Am. A*, 3(11):1809–1815, 1986.

[168] M.A. van Dam and R.G. Lane. Wave-front slope estimation. *J. Opt. Soc. Am. A*, 17:1319–1324, 2000.

[169] L. Diaz Santana Haro. *Wavefront Sensing in the Human Eye with a Shack Hartmann Sensor*. PhD thesis, 2000.

[170] P.M. Prieto, F. Vargas-Martín, S. Goelz, and P. Artal. Analysis of the performance of the Hartmann-Shack sensor in the human eye. *J. Opt. Soc. Am. A*, 17(8):1388–1398, 2000.

[171] T. Fusco, M. Nicolle, and G. Rousset. Optimisation of a Shack-Hartmann wavefront sensor for XAO system. *Proceedings of SPIE*, 5490:1155–1166, 2004.

[172] M. Nicolle, T. Fusco, G. Rousset, and V. Michau. Improvement of Shack-Hartmann wave-front sensor measurement for extreme adaptive optics. *Opt. Lett.*, 29(23):2743–2745, 2004.

[173] K.L. Baker and M.M. Moallem. Iteratively weighted centroiding for Shack-Hartmann wave-front sensors. *Opt. Express*, 15(8):5147–5159, 2007.

[174] J. Ares and J. Arines. Effective noise in thresholded intensity distribution: influence on centroid statistics. *Opt. Lett.*, 26(23):1831–1833, 2001.

[175] J. Arines and J. Ares. Minimum variance centroid thresholding. *Opt. Lett.*, 27(7):497–499, 2002.

[176] J. Ares and J. Arines. Influence of thresholding on centroid statistics: full analytical description. *Appl. Opt.*, 43(31):5796–5805, 2004.

[177] B.M. Welsh, B.L. Ellerbroek, M.C. Roggemann, and T.L. Pennington. Fundamental performance comparison of a Hartmann and a shearing interferometer wave-front sensor. *Appl. Opt.*, 34(21):4186–4195, 1995.

[178] R. Irwan and R.G. Lane. Analysis of optimal centroid estimation applied to Shack-Hartmann sensing. *Appl. Opt.*, 38:6737–6743, 1999.

[179] J. Arines and J. Ares. Significance of thresholding processing in centroid based gradient wavefront sensors: effective modulation of the wavefront derivative. *Optics Communications*, 237:257–266, April 2004.

[180] G. Rousset. *Adaptive Optics in Astronomy*. Cambridge University Press, 1999.

[181] L.A. Poyneer. Scene-based Shack Hartmann wave-front sensing: analysis and simulation. *Appl. Opt.*, 42:9527–9536, 2003.

[182] P.A. Knutsson, M. Owner-Petersen, and C. Dainty. Extended object wavefront sensing based on the correlation spectrum phase. *Opt. Express*, 13:9527–9536, 2005.

[183] J.W. Goodman. *Introduction to Fourrier Optics*. Roberts and Company, 2005.

[184] D.L. Fried. Least-square fitting a wave-front distortion estimate to an array of phase-difference measurements. *J. Opt. Soc. Am.*, 67(3):370–375, 1977.

[185] R.H. Hudgin. Wave-front reconstruction for compensated imaging. *J. Opt. Soc. Am.*, 67(3):375–378, 1977.

[186] W.H. Southwell. Wave-front estimation from wave-front slope measurements. *J. Opt. Soc. Am.*, 70(8):998–1006, 1980.

[187] J. Hardy. *Adaptive Optics for Astronomical Telescopes*. Oxford University Press, 1998.

[188] D.T. Gavel. Suppressing anomalous localized waffle behavior in least-squares wavefront reconstructors. volume 4839, pages 972–980. SPIE, 2003.

[189] K.R. Freischlad and C.L. Koliopoulos. Modal estimation of a wave front from difference measurements using the discrete Fourier transform. *J. Opt. Soc. Am. A*, 3(11):1852–1861, 1986.

[190] F. Roddier and C. Roddier. Wavefront reconstruction using iterative Fourier transforms. *Appl. Opt.*, 30(11):1325–1327, 1991.

[191] L.A. Poyneer, D.T. Gavel, and J.M. Brase. Fast wave-front reconstruction in large adaptive optics systems with use of the Fourier transform. *J. Opt. Soc. Am. A*, 19(10):2100–2111, 2002.

[192] L.A. Poyneer, M. Troy, B. Macintosh, and D.T. Gavel. Experimental validation of Fourier-transform wave-front reconstruction at the Palomar Observatory. *Opt. Lett.*, 28(10):798–800, 2003.

[193] F. Zernike. Diffraction theory of knife-edge test and its improved form, the phase contrast method. *Mon. Not. R. Astron. Soc.*, 94:377–384, 1934.

[194] B.R.A. Nijboer. The diffraction theory of aberrations. *Physica*, 23:605–620, 1947.

[195] G.-M. Dai. *Wavefront Optics for Vision Correction*. SPIE Press, 2008.

[196] J. Herrmann. Cross coupling and aliasing in modal wave-front estimation. *J. Opt. Soc. Am.*, 71(8):989–992, 1981.

[197] C.M. Harding, R.A. Johnston, and R.G. Lane. Fast simulation of a Kolmogorov phase screen. *Appl. Opt.*, 38(11):2161–2170, 1999.

[198] G.M. Dai. Modal wave-front reconstruction with Zernike polynomials and Karhunen-Loève functions. *J. Opt. Soc. Am. A*, 13(6):1218–1225, 1996.

[199] L.N. Thibos and D. Horner. Power vector analysis of the optical outcome of refractive surgery. *J. Cat. Ref. Surg.*, 28(2), in press.

[200] R. Navarro. Objective refraction from aberrometry: theory. *Journal of Biomedical Optics*, 14(2):024021, 2009.

[201] A. Guirao and D. Williams. A method to predict refractive errors from wave aberration data. *Optom. Vis. Sci.*, 80(1):36–42, 2003.

[202] D. Williams. Aliasing in human foveal vision. *Vision Research*, 25(2):195–205, 1985.

[203] S. Bará, T. Mancebo, and E. Moreno-Barriuso. Positioning tolerances for phase plates compensating aberrations of the human eye. *Appl. Opt.*, 39(19):3413–3420, 2000.

[204] L. Lundström and P. Unsbo. Transformation of Zernike coefficients: scaled, translated, and rotated wavefronts with circular and elliptical pupils. *J. Opt. Soc. Am. A*, 24(3):569–577, 2007.

[205] L.I. Epstein. The aberrations of slightly decentered optical systems. *J. Opt. Soc. Am.*, 39(10):847–847, 1949.

[206] A. Guirao, I.G. Cox, and D.R. Williams. Method for optimizing the correction of the eye's higher-order aberrations in the presence of decentrations. *J. Opt. Soc. Am. A*, 19(1):126–128, 2002.

[207] A. Guirao, D.R. Williams, and I.G. Cox. Effect of rotation and translation on the expected benefit of an ideal method to correct the eye's higher-order aberrations. *J. Opt. Soc. Am. A*, 18(5):1003–1015, 2001.

[208] E.N. Bruce. *Biomedical Signal Processing and Signal Modeling*. Wiley Series in Telecommunications and Signal Processing, 2001.

[209] C.K.Peng, J.Mietus, J.M.Hausdorff, S.Havlin, H.E.Stanley, and A.L.Goldberger. Long-range anticorrelations and non-gaussian behavior of the heartbeat. *Physical Review Letters*, 70(9):1343–1346, 1993.

[210] C.K. Peng, S. Havlin, H.E. Stanley, and A.L. Goldberger. Quantification of scaling exponents and crossover phenomena in nonstationary heartbeat time series. *Chaos*, 5(1):82–87, 1995.

[211] F.W. Campbell and J.G. Robson. High-speed infrared optometer. *J. Opt. Soc. Am.*, 49(3):268–269, 1959.

[212] P.B. Kruger and S. Mathews. Spatiotemporal transfer function of human accommodation. *Vision Research*, 34:1965Ð1980, 1994.

[213] N.R. Lomb. Least-squares frequency analysis of unequally spaced data. *Astrophysics and Space Science*, 39:447–462, 1975.

[214] J.D. Scargle. Studies in astronomical time series analysis ii. statistical aspects of spectral analysis of unevenly spaced data. *The Astrophysical Journal*, 263:835–853, 1982.

[215] G.E.P. Box and G.M. Jenkins. *Time Series Analysis, Forecasting and Control.* Holden-Day, San Francisco, California, 1970.

[216] A. Papoulis. *Probability, Random Variables, and Stochastic Processes*. WCB McGraw-Hill, 1991.

[217] N. Kasdin. Discrete simulation of colored noise and stochastic processes and 1/f power law noise. *Proc. IEEE*, 83:802–827, 1995.